UNIVERSITY OF CALIFORNIA SAN DIEGO

Mechanisms of UVR-Tolerance in Phytoplankton and Applications of Cyanobacteria for Engineered Living Materials

A Dissertation submitted in partial satisfaction of the requirements
for the degree Doctor of Philosophy

in

Oceanography

by

Elliot Lloyd Weiss

Committee in charge:

Professor Susan S. Golden, Co-Chair
Professor B. Greg Mitchell, Co-Chair
Professor Andrew E. Allen
Professor Julia M. Diaz
Professor James W. Golden
Professor Brian Palenik

2022

The Dissertation of Elliot Lloyd Weiss is approved, and it is acceptable in quality and form for publication on microfilm and electronically.

University of California San Diego

2022

DEDICATION

This dissertation is dedicated to my parents, Dennis and Kathleen, for their endless love, support and curiosity for the world.

TABLE OF CONTENTS

LIST OF FIGURES

Chapter 2

Chapter 2 Supplemental

Chapter 3

LIST OF TABLES

Chapter 2

Chapter 3

Chapter 4

Chapter 5

ACKNOWLEDGMENTS

Firstly, I would like to thank my committee members for their support and guidance over the course of my PhD. Particularly, I would like to thank the co-chairs of my committee, Greg Mitchell and Susan Golden. Greg, thank you for putting the wind in my scientific sails. Joining as a member of the Scripps Photobiology Group on research cruises to the Arctic showed me the exciting places that science can take you and inspired me to continue my scientific journey. The Mitchell lab allowed me to realize just how fun science can be, in the field or in the lab. Once SPG, always SPG! Susan, thank you for adopting me into your laboratory when my scientific interests began to align with yours. I greatly appreciate the way in which you put your students first, and I couldn't have asked for a better laboratory to call a second home. You are an inspiration, and your support and guidance dramatically enhanced my PhD experience. The knowledge, techniques, skills, and critical thinking that I gained as a part of the Golden lab have helped to shape me into the more mature scientist that I am today.

Thank you to Golden lab members Arnaud, Mingxu, Cigdem, Ryan, Marie, Vinson and Bryan for helping to guide me in the laboratory. I would also like to thank Maria Vernet and Jim Golden for the unofficial mentorship they have provided over my years at SIO and acknowledge that the research presented here would not have been possible without financial support from the Scripps Fellowship, the NSF GRFP, and the UC San Diego MRSEC Graduate Fellowship.

I would be remiss to not thank the friends who made the time during my PhD so enjoyable. Nachi, Brendan and Kräg, thank you for being constant sources of friendship since day one. Emma, Jon, Chase, Karthik and Daniel, I'll remember the times we spent in the mountains climbing forever, and hope that we have many more opportunities to do so. Daniel,

thank you for not only being a great climbing partner, but for your scientific mentorship as well. To Hopsy and Peaches, thank you for being such comforting companions during the preparation of this dissertation.

Lastly, I would like to thank my wonderful family. Notably, my parents Dennis and Kathleen. Thank you for your continual support and efforts to put my education first. Your warm demeanors and appetites for knowledge are inspirational and have helped to shape who I've become. I would not be where I am today without all of your love and support. Emily, thank you for always being there. Thank you for navigating life with me, as well as the chapters of this thesis! I am so lucky to have someone to discuss our experimental designs with over dinner. Your support and love have been essential components of this dissertation.

Chapter 2, in full, appears as submitted for publication as it may appear as Weiss EL, Fang M, Taton A, Szubin R, Palsson BØ, Mitchell BG, Golden SS, 2022. UVR-Tolerance Genes Revealed by a Genome-wide Fitness Assessment in a Model Cyanobacterium. The dissertation author was the primary investigator and author of this paper.

Chapter 3, in full, is in preparation for submission as Weiss EL, Cape MR, Pan BJ, Smyth TJ, Vernet M, Mitchell BG. The Distribution of Mycosporine-like Amino Acids in Phytoplankton Across a Southern Ocean Transect. The dissertation author was the primary investigator and author of this paper.

Chapter 4, in part, is currently being prepared for submission for publication of the material as Datta D*, Weiss EL*, Wangpraseurt D, Hild E, Chen S, Golden JW, Golden SS, Pokorski JK. Bio-composite Hydrogels with Engineered Cyanobacteria Yield Stimuli-responsive Photosynthetic Materials for Bioremediation. The dissertation author was the co-primary researcher and author (*) of this material.

Chapter 5 consists of unpublished material. The dissertation author was the primary author of this material. The following individuals are also authors on this work: Section 5.2- Susan Golden (UCSD), Ben Harrison (Ecosense); Section 5.3- Susan Golden (UCSD); Section 5.4- Tiago Ferreira-leão (UCSD), Evgenia Glukhov (UCSD), Lena Gerwick (UCSD).

VITA

2010 Bachelor of Science in General Biology, University of California San Diego

2019 Master of Science in Marine Biology, University of California San Diego

2022 Doctor of Philosophy in Oceanography, University of California San Diego

PUBLICATIONS

Weiss EL, Fang M, Taton A, Szubin R, Palsson BØ, Mitchell BG, Golden SS. UVR-Tolerance Genes Revealed by a Genome-wide Fitness Assessment in a Model Cyanobacterium. *(in review*)

Weiss EL, Cape MR, Pan BJ, Smyth TJ, Vernet M, Mitchell BG. The Distribution of Mycosporine-like Amino Acids in Phytoplankton Across a Southern Ocean Transect. (*in preparation*)

Datta D***, Weiss EL***, Wangpraseurt D, Hild E, Chen S, Golden JW, Golden SS, Pokorski JK. Bio-composite Hydrogels with Engineered Cyanobacteria Yield Stimuli-responsive Materials for Bioremediation. (*in preparation*)

Reiss CS, Cossio A, Santora JA, Dietrich KS, Murray A, Mitchell BG, Walsh J, **Weiss EL**, Gimpel C, Jones CD, Watters GM (2017). Overwinter habitat selection by Antarctic krill under varying sea-ice conditions: implications for top predators and fishery management. *Marine Ecology Progress Series*, *568*, pp.1-16.

Cohen RE, James CC, Lee A, Martinelli MM, Muraoka WT, Ortega M, Sadowski R, Starkey L, Szesciorka AR, Timko SE, **Weiss EL** (2018). Marine host-pathogen dynamics: influences of global climate change. *Oceanography*, *31*(2), pp.182-193.

Kahru M, Anderson C, Barton AD, Carter ML, Catlett D, Send U, Sosik HM, **Weiss EL**, Mitchell BG (2021). Satellite detection of dinoflagellate blooms off California by UV reflectance ratios. *Elem Sci Anth*, *9*(1), p.00157.

Shen Y, Benner R, Murray AE, Gimpel C, Mitchell BG, **Weiss EL**, Reiss C (2017). Bioavailable dissolved organic matter and biological hot spots during austral winter in Antarctic waters. *Journal of Geophysical Research: Oceans*, *122*(1), pp.508-520.

Mendoza WG, **Weiss EL**, Schieber B, Mitchell BG (2017). Controls on the distribution of fluorescent dissolved organic matter during an under-ice algal bloom in the western Arctic Ocean. *Global Biogeochemical Cycles*, *31*(7), pp.1118-1140.

ABSTRACT OF THE DISSERTATION

Mechanisms of UVR-Tolerance in Phytoplankton and Applications of Cyanobacteria for Engineered Living Materials

by

Elliot Lloyd Weiss

Doctor of Philosophy in Oceanography

University of California San Diego, 2022

Professor Susan S. Golden, Co-Chair
Professor Brian G. Mitchell, Co-Chair

Phytoplankton are central to biogeochemical cycling and climate regulation on Earth and have been utilized for various biotechnological applications, such as the production of high value nutraceuticals, chemicals and therapeutics. While phytoplankton depend on light for photosynthesis, they are not immune to the deleterious effects of ultraviolet radiation (UVR) that can be present in the water column to depths of up to 20 m. This dissertation investigates the genetic basis of UVR tolerance in a model cyanobacterium using the high-throughput genomic screening technique RB-TnSeq and identifies an important and

previously overlooked leucyl aminopeptidase (LAP) with cysteinyl-glycinase properties. The LAP is conserved across many ecologically relevant species and may be a key component of the glutathione catabolism pathway, with a pH-dependence that modulates activity of the enzyme based on the photosynthetic activity of the cell. This dissertation also presents the first report of the distribution of mycosporine-like amino acids (MAAs) across the surface of the Southern Ocean on a transect from Eastern New Zealand to the Western Antarctic Peninsula. MAAs, small strongly UVR-absorbing synthesized by phytoplankton and many other organisms, are an effective sunscreen against photo-inhibition and provide a defense against the photooxidative stress of UVR. Correlations were found between MAA composition and phytoplankton taxa, as well as between the ratio of MAAs to chlorophyll-a and the mean UVR dosage experienced the month prior, establishing a baseline for the quantity and quality of this ecologically important bioindicator of UVR-stress. Additionally, a novel biotechnological application of phytoplankton is presented in which genetically engineered cyanobacteria are 3D printed into an alginate hydrogel, producing a stimuli-responsive photosynthetic living material with functional outputs useful for bioremediation and the capacity for inducible cell death to prevent biofouling of the environment. A final data chapter includes projects extending beyond studies of the ultraviolet to the genetic basis of tolerance of unique spectral qualities of light in a model cyanobacterium. Together, this dissertation integrates the interactions between phytoplankton and light, from environmental to genomic levels, and presents a novel biotechnological application of cyanobacterial strains as bioengineered components of a living material.

CHAPTER 1: General Introduction

Algae and cyanobacteria are central to biogeochemical cycling and climate regulation on Earth. The marine planktonic fraction of algae and cyanobacteria, collectively referred to as marine phytoplankton, account for less than one percent of the photosynthetic biomass on Earth yet are responsible for an estimated 40 percent of all photosynthesis (Falkowski, 1994) and half of global net primary production (NPP), equal in magnitude to the NPP of terrestrial systems (Field et al., 1998; Zhao and Running, 2010). While phytoplankton are tightly coupled to photosynthetically available radiation (PAR, 400 – 700 nm) for photosynthesis, they are not immune to the damaging effects of ultraviolet radiation (UVR, 280 – 400 nm) that can penetrate the water column to depths of up to 20 meters (Boelen et al., 1999).

The balance between the requirement of PAR for photosynthesis and the damage induced by concurrent UVR has been in flux since the advent of photosynthesis, which is estimated to have evolved in protocyanobacteria between 3.2 to 3.5 billion years ago during the Archean Eon (Allen and Martin, 2007; Des Marais, 2000). Approximately 2.4 billion years ago, oxygen produced by photosynthesis began to accumulate in the atmosphere (Buick, 2008), ultimately forming a stratospheric ozone shield, filtering out virtually all UVC radiation (< 280 nm), and dramatically decreasing levels of UVB (280 – 320 nm) incident on Earth's surface. An implication of this timeline is that photosynthesis evolved in an "age of UVR", an environment with high fluxes of UVC and UVB relative to the modern environment, and in order to tolerate these extreme environments early photosynthetic organisms would have required UVR protection mechanisms concurrent with the evolution of photosynthesis. Aquatic microorganisms, such as phytoplankton, have the advantage over terrestrial systems of the

attenuation of UVR in water, creating a refuge from UVR with depth. However, regions of strong upwelling or wind-induced mixing of the upper ocean layers may overcome these adjustments, creating intermittent periods of high UVR exposure (Neale et al., 1998).

During the 1980s there was a surge in research pertaining to the interactions between phytoplankton and UVR, due largely to concerns over a periodic decline in stratospheric ozone concentrations over Antarctica and the Arctic caused by the anthropogenic emission of chlorofluorocarbons (De Mora et al., 2000). However, the establishment of the Montreal Protocol in 1987 resulted in the gradual remediation of ozone depletion and has put us on track for ozone recovery, assuming continued vigilance and safeguarding (Chipperfield et al., 2017). In light of this positive news, the initiative and funding for research on phytoplankton-UVR interactions has subsequently slowed. Nevertheless, an understanding of mechanisms of UVR tolerance in phytoplankton remains important in the era of an anthropogenically influenced changing climate, defined not only by changes to the ozone layer, but by rising global temperatures, ice melt, and variations in water-column mixed layer depths. The increased exposure of phytoplankton to UVR in aquatic regions experiencing shoaling mixed layer depths will result in changes in production and plankton community structure directly related to changes in UVR dosage (Constable et al., 2014).

The canonical methods of UVR damage in phytoplankton have long been understood, such as the formation of reactive oxygen species (ROS), the formation of thymine and cyclobutane pyrimidine dimer lesions in DNA, damage to proteins, and the inhibition of photosynthesis (Häder and Sinha, 2005). UVR can affect photosynthesis by damaging the D1 protein in the reaction center of photosystem II (PSII) (Häder et al., 2011), impairing repair of D1, and damaging accessory pigments, such as phycobilins (Singh et al., 2010). However, not all

wavelengths of UVR are equally deleterious to photosynthesis. Several studies have demonstrated the wavelength-dependent response of inhibition of photosynthesis by UVR by creating biological weighting factors for inhibition by UVR for phytoplankton, with shorter wavelengths resulting in enhanced inhibition levels (Cullen et al., 1992). Recent research has revealed that current estimates of NPP may overestimate production in the open ocean by *Synechococcus* and *Prochlorococcus* by up to 20%, due to the exclusion of biological weighting factors for the inhibition of photosynthesis by UVR (Neale and Thomas, 2017).

Over time phytoplankton have evolved a variety of mechanisms to cope with high light and UVR stress, such as the synthesis of enzymes for the repair of damaged DNA and proteins, the quenching of ROS, the synthesis of UVR-protective molecules such as syctonemin, mycosporine-like amino acids (MAAs) and certain UVR-absorbing carotenoids such as phytoene, and the avoidance of UVR altogether via motility, changes in buoyancy, or mat formation (Häder et al., 2015). Most studies on UVR tolerance in phytoplankton have targeted specific processes in these categories that were previously shown to confer resilience, often using transcript-dependent methodologies such as RNA-Seq to detect UVR-responsive genes as a proxy for gene relevance. While undoubtedly a useful strategy for gaining a deeper understanding of specific mechanisms and the transcriptomic landscape of the cell under UVR, there are likely other tolerance mechanisms in a diversity of organisms that have not been identifiable using traditional techniques that rely on prior knowledge.

A relatively new genomics tool, random barcode transposon site sequencing (RB-TnSeq), has proven to be particularly useful for elucidating genes that are most important under particular conditions and for sustaining a variety of processes in prokaryotic organisms, including the cyanobacterium *Synechococcus elongatus* PCC 7942 (*S. elongatus*) (Rubin et al., 2015; Wetmore

et al., 2015; Welkie et al., 2018; Taton et al., 2020; Simkovsky et al., 2022). RB-TnSeq is a methodology in which a library of mutants is created using transposons that carry an antibiotic resistance cassette along with unique 20-nucleotide barcodes. Each insertion event results in a single gene disruption with a uniquely barcoded insert amidst a population of millions of cells, each similarly containing a unique barcode in a unique location. Using RB-TnSeq, the initial population of mutants in the library can be sequenced and quantified based on these barcodes, subsequently exposed to a condition, and re-sequenced after several generations of growth to identify changes in the population density of individual mutants. Genes whose interruption results in lower counts at the end of the experimental period are interpreted as being important for fitness under the experimental condition.

In **chapter 2**, I leverage RB-TnSeq to elucidate the gene set that is most important in a model organism, the freshwater cyanobacterium *S. elongatus*, for tolerating UVR stress under a light cycle that matches natural UVR dosage and spectral quality. The resultant data highlight the importance of a leucyl aminopeptidase (LAP) with cysteinyl-glycinase properties that may be an important component of the glutathione catabolism pathway, with a pH-dependence that may modulate activity based on the photosynthetic activity of the cell. The importance of this LAP in UVR tolerance has likely been overlooked due to unchanging transcript levels under acute UVR exposure, highlighting the utility of fitness screens such as RB-TnSeq versus transcript-based screens. Subsequent experiments demonstrated that the UVR-sensitive phenotype of LAP knockout strains is conserved across a diversity of species. The results of this study also support the importance of genes involved in many previously identified mechanisms of UVR tolerance.

In **chapter 3**, I turn my focus towards one of the canonical methods of UVR tolerance in phytoplankton, the synthesis of MAAs, and describe the distribution of MAAs across the

Southern Ocean. MAAs are found in a diversity of organisms such as bacteria, fungi, and fish, either by synthesis or by bioaccumulation via the consumption of lower trophic levels. MAAs are frequently part of an overall strategy to diminish the adverse effects of UVR (Lesser, 1996; Dunlap and Shick, 1998). MAAs are among the strongest UVR-absorbing products found in nature, which are characterized by their low molecular weight, high solubility and polarity. MAAs, composed of a cyclohexenimine or cyclohexenone chromophore linked to an amino acid, amino alcohol, or amino group with absorption maxima ranging from 309 to 362 nm, act as an effective sunscreen against photo-inhibition and provide a defense against the photooxidative stress of UV radiation (Carreto and Carignan, 2011).

A recent study using a satellite-based algorithm with data from a new ocean-color sensor on the Japanese GCOM-C satellite, with capabilities for higher spectral resolution extending into the UVR region, demonstrated that MAAs in phytoplankton may be detectable from space (Kahru et al., 2021). Leveraging differences in the spectral signature of MAAs produced by the dinoflagellate *Lingulodinium polyedra* and a neighboring diatom bloom, the ratio of reflectance from the ocean surface in the blue region of the visible spectrum to the UV spectrum ($R_{rs}380/R_{rs}443$) was used to differentiate the two populations. It is conceivable that, with continued developments in ocean-color sensor technology, in tandem with a thorough ground-truthing of the global distribution of MAAs and their associated taxa, remote sensing extended to UVR channels will improve algorithms for global phytoplankton taxa differentiation.

Various studies have assessed phytoplankton MAA composition in coastal marine and freshwater systems and in laboratory cultures (Whitehead and Vernet, 2000; Llewellyn and Harbour, 2003; Carreto et al., 2018), yet little is known about the abundance and composition of MAAs throughout the world's oceans, as few studies have been conducted on large spatial

scales. In **chapter 3**, I incrementally close this gap in knowledge by reporting the first continuous assessment of the distribution of MAAs across the surface of the Southern Ocean, in a transect from Christchurch New Zealand to the Western Antarctic peninsula, and find correlations between MAA composition, phytoplankton taxa, and abiotic factors.

In **chapter 4**, I take a turn from exploring what nature has invented and our understanding of it, to exploring how humankind can utilize phytoplankton for modern biotechnological applications, specifically for engineered living materials (ELMs). Over the past several decades, phytoplankton have been exploited for a number of biotechnological applications, such as the production of biofuels, high value cosmetic and dietary products, bioplastics, and cultivation for feedstock. There are a number of advantages of utilizing phytoplankton for biotechnology, including the fact that microalgal cultivation can take place on non-arable land, that non-potable water can be used as a source of culture media, and that microalgal productivity is much higher than that of vascular plants. In most cases, the main disadvantage is the engineering challenge of developing a low cost, scalable cultivation system with low energy requirements for harvesting and the extraction of desired products (Leite et al., 2013). The latter disadvantage has thus far proven a challenge for the establishment of an economical algal biofuels market, but the production of high value products has been relatively successful.

At the intersection of materials science and synthetic biology lies the field of ELMs, which has evolved into a discipline of its own over the past decade (Leite et al., 2013). ELMs are defined by the inclusion of a living component, such as a unicellular organism, in a polymeric matrix, or material. Current methods of ELM construction include combining cells with a polymer via 3D printing, microencapsulation, or the production of the matrix via the

microorganisms themselves (Rodrigo-Navarro et al., 2021). A wide variety of organisms have been utilized in ELMs, including bacteria, yeast, and fungi for purposes such as the fabrication of skin patches for wound healing (González et al., 2020), sweat-responsive biohybrid fabrics (Wang et al., 2017), and a biodegradable aquaplastic (Duraj-Thatte et al., 2021). One advantage of ELMs over traditional materials is that the biological component of the ELM can be genetically engineered to provide complex responses to environmental stimuli and produce functional biological outputs.

One limitation of many ELMs outside of the laboratory is the availability of nutrients required for the viability of the biological component. Photosynthetic microorganisms are an attractive solution to this limitation, as they fundamentally depend on only light, CO_2 as a carbon source, and minimal nutrients. Cyanobacteria, in particular, are an attractive photosynthetic group for ELMs as there has been extensive work over the past few decades building toolkits for synthetic biology (Vijay et al., 2019), thus enabling the engineering of functional biological outputs in the ELM using existing tools.

In **chapter 4**, in a collaborative project under the UC San Diego Materials Research Science and Engineering Center (MRSEC), we present an ELM composed of the cyanobacterium *S. elongatus* embedded in an alginate hydrogel matrix. The hydrogel is photosynthetically active, with the capability of growing in cellular density under low to moderate light levels when immersed in liquid medium (BG-11). The ELM was further characterized with respect to its rheological properties, its structure by scanning electron microscopy, and its photosynthetic activity by proxy of oxygen evolution and chlorophyll fluorescence measurements. To enable the ELM to be environmentally responsive and provide a functional output, several strains of genetically modified *S. elongatus* were created and

incorporated into the hydrogel with capabilities for bioremediation, and inducible cell death to prevent biofouling in the surrounding environment.

Lastly, **chapter 5** is subdivided into three sections, each of which covers independent projects that were conducted during the course of this dissertation and are included for posterity, to guide future researchers who would like to advance the work presented here. The first subsection discusses the results of an RB-TnSeq experiment conducted on *S. elongatus* PCC 7942 to investigate genes important for fitness under varying spectral niches, such as those found in lakes, rivers, and the open ocean, which are formed due to the attenuation and scattering of light by water, dissolved organic matter, and phytoplankton biomass. These experiments were caried out using a custom light-engine fabricated by Ecosense®, to recreate the spectral signatures of these ecological niches. Genes of interest were identified for several spectral niches, and hypotheses for the mechanisms of fitness for these genes are suggested.

The second subsection of **chapter 5** discusses the results of a high-throughput genetic interaction screen (IRB-Seq) conducted in an attempt to determine genes responsible for the transition in expression from *psbAI*, which encodes the D1 isomer D1:1 in photosystem II, to *psbAII and psbAIII*, which each encode the isomer D1:2 (Schaefer and Golden, 1989). The D1 protein, a key subunit of photosystem II, is easily damaged under high irradiances, and thus its turnover is critical to maintain viability of the photosynthetic apparatus (Schaefer and Golden, 1989). The functional significance of maintaining various D1 protein isomers and the transition in expression of the isomers is thought to be a strategy for tolerating abrupt transitions to high light and/or UVR (Vinyard et al., 2013). Despite the importance of this mechanism, the genes central to its regulation have remained elusive. While the results of this study were largely

inconclusive, genes demonstrating strong interactive fitness effects are described to guide follow-up studies.

The third section of **chapter 5** explores the biosynthetic pathways for MAA production in cyanobacteria. While MAAs are seemingly ubiquitous in the world's oceans, and common in both terrestrial and freshwater alpine environments, we still have limited knowledge of the genetic basis behind the diversity of the 40+ MAAs currently identified in nature. An enhanced understanding of the genetic underpinnings of this diversity may prove highly informative in the current era of big data, as metagenomic and transcriptomic datasets could be mined for such pathways to enhance our understanding of MAA distributions and regulation in the context of a changing climate.

Our understanding of the genetic basis of MAA synthesis has gained momentum over the past decade. Fundamentally, in cyanobacteria, MAAs are synthesized via a biosynthetic gene cluster (BGC) comprising at least three components (Balskus and Walsh, 2010). In *Anabaena variabilis* ATCC 29413, the pentose phosphate pathway intermediate sedoheptulose 7-phosphate is modified by a dehydroquinate synthase homolog 2-epi-5-epi-valionate synthase and an adjacent O-methyltransferase, to form a single product, 4-deoxygadusol (4-DG). 4-DG and glycine are then converted by an ATP-grasp family member to form mycosporine-glycine, a basal mycosporine with an absorption maximum of 310 nm (Balskus and Walsh, 2010). Mycosporine-glycine is thought to be the core molecule from which other MAAs are derived. A non-ribosomal peptide synthase (NRPS)-like enzyme, containing adenylation, thiolation, and thioesterase domains, converts mycosporine glycine and serine to shinorine, an MAA synthesized by many phytoplankton, which has an absorption maximum of 334 nm.

In addition to the importance of understanding the biology and ecology of these molecules, MAAs show great biotechnological promise as next-generation sunscreen compounds. Recent studies have demonstrated that some of the chemical compounds present in commercial sunscreens, such as benzophenone-3, can have toxic effects on corals (Danovaro et al., 2008). It is estimated that between 6,000 and 14,000 tons of sunscreen lotion, many containing up to 10% benzophenone-3, are released into coral reef environments annually (Downs et al., 2006). In 2018, Hawaii was the first US state to ban the sale of sunscreens containing oxybenzone and octinoxate, and thus there has been a new focus on sunscreen alternatives. While a few companies, such as Mibelle Biochemistry in Switzerland, have adopted MAAs as UV-screening additives to their cosmetic products, the algal strain most commonly used for MAA production, *Porphyra umbilicalis*, is relatively slow growing, and the MAAs it produces cover only a limited bandwidth of the UVR spectrum. The heterologous expression of a diversity of MAAs will be a useful and economical organic sunscreen alternative for many current commercial sunscreens.

In the third subsection of **chapter 5**, I used a bioinformatics approach to mine the genomes of cyanobacterial isolates available locally in the laboratory of Professor Gerwick at the Scripps Institution of Oceanography in a search for strains capable of synthesizing MAAs. Candidate strains were grown under UVR for one month, harvested, extracted, and analyzed for the presence of MAAs. Attempts were then made to express the putative biosynthetic gene clusters responsible for MAA synthesis in *Escherichia coli*.

Together, this work embodies the interactions between phytoplankton and light, from environmental to genomic levels, and explores how humankind can benefit from this knowledge by utilizing phytoplankton for modern biotechnological applications.

CHAPTER 2: UVR-Tolerance Genes Revealed by a Genome-wide Fitness Assessment in a Model Cyanobacterium

Abstract

Ultraviolet radiation (UVR) has significant physiological effects on organisms living at or near the Earth's surface, yet the full suite of genes required for fitness of a photosynthetic organism in a UVR-rich environment remains unknown. This study reports a genome-wide fitness assessment of the genes that affect UVR tolerance under environmentally relevant UVR dosages in the model cyanobacterium *Synechococcus elongatus* PCC 7942. Our results highlight the importance of specific genes involved in DNA repair, glutathione synthesis, and the assembly and maintenance of photosystem II, as well as genes that encode hypothetical proteins, and others without an obvious connection to canonical methods of UVR tolerance. Disruption of a gene that encodes a leucyl aminopeptidase (LAP) conferred the greatest UVR-specific decrease in fitness. Enzymatic assays demonstrated a strong pH-dependent affinity of the LAP for the dipeptide cysteinyl-glycine, suggesting an involvement in glutathione catabolism as a function of night-time cytosolic pH level. A low differential expression of the LAP gene under acute UV exposure suggests that its relative importance would be overlooked in transcript-dependent screens. Subsequent experiments revealed a similar UVR-sensitivity phenotype in LAP knockouts of other organisms, indicating conservation of the functional role of LAPs in UVR tolerance.

Significance

Cyanobacteria account for ~25% of global primary production and dominate vast regions of the ocean, as well as biological soil crusts. While they rely upon light availability for

photosynthesis, they are simultaneously exposed to high levels of ultraviolet radiation (UVR). Damage induced by UVR decreases photosynthetic rates, suggesting that previous calculations of global primary production may be overestimated. Despite the strong impact of UVR on phytoplankton, there has not yet been a genome-wide fitness assessment to identify genes that are important for UVR tolerance in a photosynthetic organism under environmentally relevant UVR dosages. Previous work on the genetic basis of UVR tolerance in phytoplankton has focused on UVR-regulated genes as a proxy for UVR-tolerance roles or has used unnatural dosages of UVR in the experimental design. Here we report the genes that are most critical for UVR tolerance in a photosynthetic organism and the enzymatic function of a highly conserved leucyl aminopeptidase whose disruption results in the most striking loss of fitness under UVR.

Introduction

Ultraviolet radiation (UVR, 300-400 nm) is the most photochemically reactive waveband of the solar radiation field and can have deleterious effects on the physiology of organisms that live on Earth's surface or in the near-surface region of lakes and oceans. While photosynthetic organisms rely on photosynthetically available radiation (PAR, 400-700 nm) for photosynthesis, they are not immune to the harmful effects of UVR that are concurrent with PAR. These effects can occur at biologically relevant levels in the water column to depths of up to 20 meters (Gieskes and Kraay, 1990; Boelen et al., 1999). In the era of anthropogenically influenced changing climate, defined by changes to the ozone layer, ice melt, aerosol concentrations, cloud cover, and variations in water-column mixed layer depths, phytoplankton production and community structure will respond directly to related changes in UV dosage, although these changes remain difficult to predict (Constable et al., 2014). Natural populations of phytoplankton

will respond differently to changes in UVR stress. For example, large-celled diatoms are typically less affected by high light irradiances and UVB while picoplankton typically experience more damage (Jin et al., 2017). The metabolic pathways that mediate damage and oxidative stress are therefore also diverse and many are potentially undiscovered.

Types of damaged induced by UVR in phytoplankton have long been understood, such as the formation of reactive oxygen species (ROS), damage to DNA and proteins, and the inhibition of photosynthesis. The general mechanisms of tolerance are thus considered to be DNA repair, protein repair and recycling, and the synthesis of antioxidants and photo-protective molecules, as well as avoidance of UVR via motility and mat formation (Häder et al., 2015). Most studies on UVR tolerance in phytoplankton have targeted specific processes in these categories that were previously shown to confer resilience, using transcript-dependent methodologies such as RNA-Seq to detect UVR-regulated genes as a proxy for gene relevance. Many of these studies used spectral qualities such as UV-C or extreme dosage levels of UVR that have not been relevant in the natural environment since the development of a protective stratospheric ozone layer (Mloszewska et al., 2018). Previous research has demonstrated that the harmful effects of UVR on phytoplankton is highly wavelength dependent, with shorter wavelengths in the UV-B region inhibiting photosynthetic activity exponentially more than longer wavelengths in the UV-A region (Day and Neale, 2002). A dearth of genome-wide screens for UVR tolerance in phytoplankton, under realistic conditions, suggests that mechanisms and genes important for UVR tolerance remain to be discovered.

Random barcode transposon site sequencing (RB-TnSeq) is a methodology that has proven to be particularly useful for elucidating genes that are most important to sustain a variety of conditions and processes in the model cyanobacterium *Synechococcus elongatus* PCC 7942

(Rubin et al., 2015; Welkie et al., 2018; Taton et al., 2020; Simkovsky et al., 2022). In this study we leveraged RB-TnSeq to elucidate the gene set that is most critical in *S. elongatus* for tolerating UV stress under a light cycle that matches natural UVR dosage and spectral quality. Our data highlight the importance of a leucyl aminopeptidase with cysteinyl-glycinase activity that was previously overlooked and support the involvement of many canonical processes in UVR tolerance.

Results

Physiological response and transcriptomic landscape of wild type S. elongatus grown under a light-dark cycle with three UVR dosages

A suite of experiments was conducted to assess how *S. elongatus* is affected by three environmentally relevant UVR dosages. Wild-type (WT) cultures of *S. elongatus* grown to exponential phase and transferred to quartz photobioreactors were exposed to a 12-h light:12-h dark cycle with the addition of UVR for the central 6 h of the light period at one of three dosages levels: low UVR (LUV), medium UVR (MUV), or high UVR (HUV), or the PAR-only control (**Figure 2.1A**). Growth rates were equivalent among the LUV, MUV and PAR-only conditions throughout the experimental period. However, cells in the HUV condition grew more slowly than the PAR-only control during an initial 53-h phase, after which all growth rates were equivalent (experimental h 53-104) (**Figure 2.1B**). ROS measured in cultures over the course of the light cycle illustrated a distinct pattern of ROS formation and dissipation (**Figure 2.1C**). At the end of the 6-h UVR exposure period, ROS was higher in all UVR samples relative to the PAR-only control (P value LUV < 0.05; MUV < 0.01; HUV < 0.001). At the end of the following 6 h of white light, ROS levels in the UVR treatments dropped below the PAR-only

treatment. No ROS was detected the next morning following 12 h of darkness, implying that cells were able to fully scavenge all ROS. Surprisingly, after the 6 h white-light period at virtual dawn, there was significantly greater ROS detected in the UVR samples, despite no UVR exposure for this period. It is possible that an accumulation of damaged DNA and proteins from the UVR exposure of the prior light cycle stimulated enhanced photosynthetic activity, resulting in elevated ROS. Whole cell absorption spectra normalized to 675 nm showed pronounced variations in the ratio of the 630 nm to the 675 nm peak, indicating greater absorption by phycobiliproteins (PBPs) in PAR-only relative to UVR treatments, and suggesting either the downregulation of PBPs or destruction of PBPs under UVR (**Figure 2.1D**).

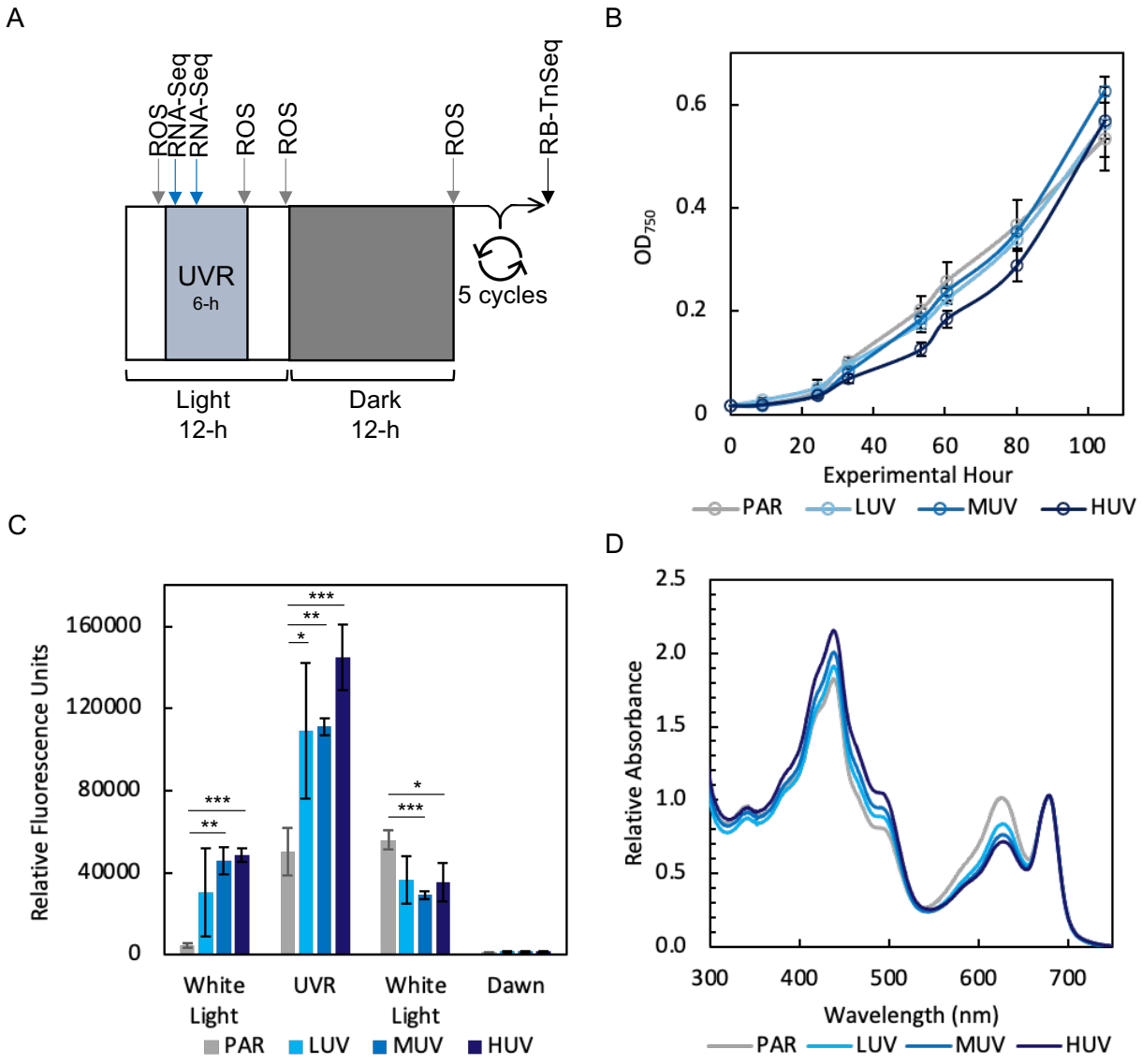

Figure 2.1. WT growth and physiological response to PAR only, LUV, MUV, and HUV conditions. A) Schematic of 12-h light:12-h dark cycle and 6-h UVR period, including ROS sampling points, 15 min and 2 h RNA-Seq sampling points, and RB-TnSeq sampling point after 5 light:dark cycles. B) OD_{750} measured over 105 hours. C) ROS measured in the whole cell fraction by H_2DCFDA fluorescence. Measurements were taken at the end of the labelled point in the light cycle. D) Whole cell absorption spectra of each UVR condition after 4 days of growth normalized to 675 nm. Data points are mean (SD); n = 3.

Differential expression of genes during the UVR period was analyzed 15 min and 2 h after the onset of the UVR period under the HUV condition using RNA-Seq. After 15 min of UVR exposure, 28 genes were upregulated ($\log_2$ fold change > 2; adjusted *P* value < 0.05), while

18 were downregulated (**Figure 2.2**). Transcripts strongly downregulated upon 15 min UVR exposure primarily encode proteins related to photosystem I subunits and phycobiliprotein-containing light-harvesting complexes. Transcripts most upregulated upon 15 min of UVR exposure encode proteins involved in light quenching, the synthesis of photosystem II D1 protein isomers PsbA2/PsbA3; protein turnover; carotenoid cycling; transcription; and replication, recombination and repair. After 2 h of UVR exposure, 41 genes were differentially upregulated, while 377 were downregulated. Strongly downregulated genes relate to photosystems I and II, energy conversion, phycobiliprotein-containing light harvesting complexes, and translation. Of the transcripts belonging to the 'translation' COG functional group, those showing strong downregulation included the *rpl*, *rpm*, and *rps* gene families.

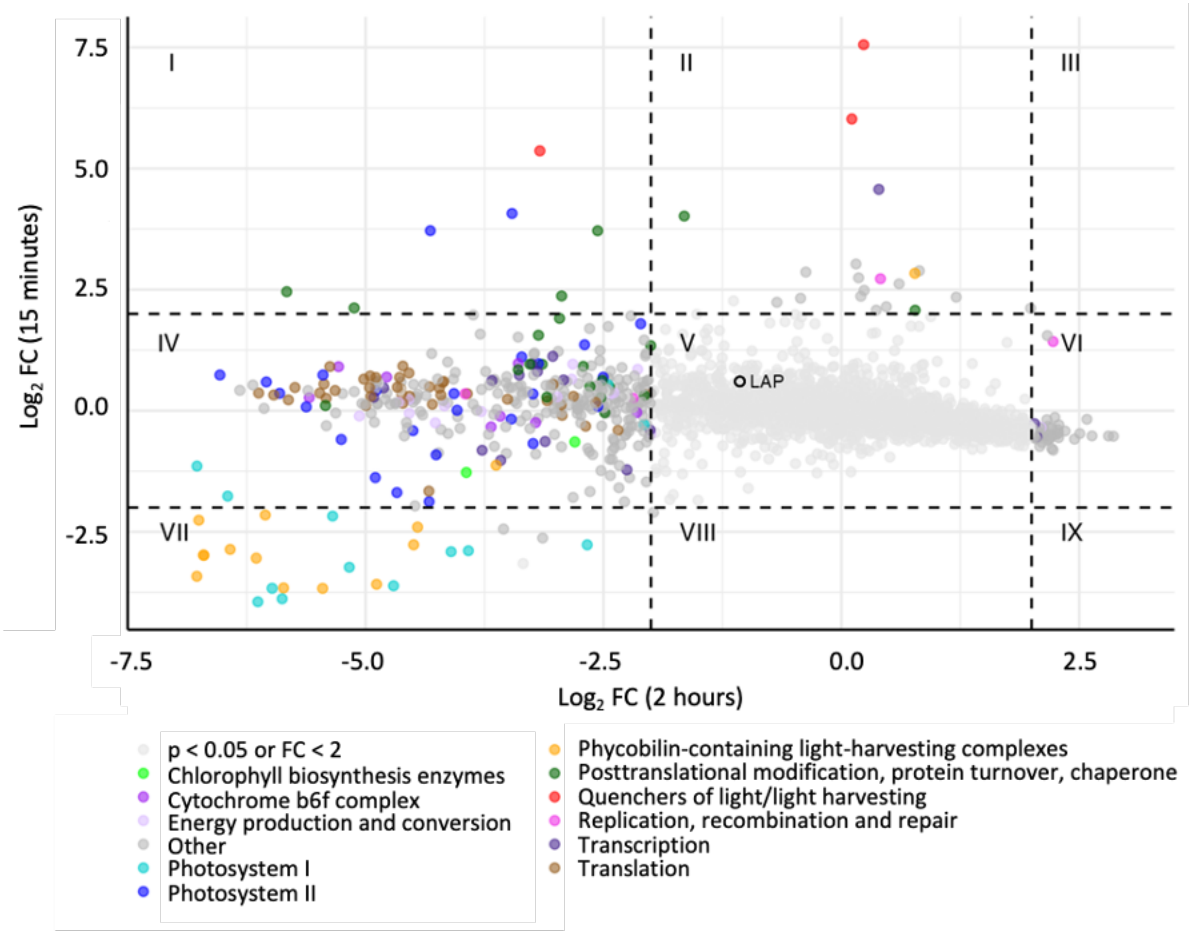

Figure 2.2. Differential expression of genes in the WT strain after 15 minutes (y-axis) or 2 hours (x-axis) of HUV exposure relative to PAR only. Genes are color coded by select functional families. Dotted lines indicate the ± 2 $\log_2$ fold change thresholds, with roman numerals indicating genes that are: I) upregulated at 15 min and downregulated at 2 h, II) upregulated at 15 min only, III) upregulated at 15 min and 2 h, IV) downregulated at 2 h only, V) without strong differential expression, VI) upregulated at 2 h only, VII) downregulated at both 15 min and 2 h, VIII) downregulated only at 15 min, IX) downregulated at 15 min and upregulated at 2 h of UVR exposure. The leucyl aminopeptidase gene *Synpcc7942_1190* is highlighted in section V.

Assessment of Genome-wide Fitness Under UVR using RB-TnSeq

A fresh culture of the RB-TnSeq mutant library of *S. elongatus* PCC 7942, recovered from a frozen archive following a standardized protocol (Rubin et al., 2015), was entrained in a 12-h light: 12-h dark cycle for 48 h, and inoculated into quartz tubes; cultures were incubated

with or without the addition of a 6-h LUV, MUV, or HUV exposure period to a 12-h light: 12-h dark regimen. The cultures were diluted to an OD_{750} of 0.05 halfway through the experimental period to minimize the attenuation of incident light. After 5-6 generations of growth the library was harvested and the barcodes were sequenced (Rubin et al., 2015). Based on the relative number of barcode sequence reads per gene under each UVR condition to the PAR-only condition, we were able to quantify the relative fitness contribution of each gene under each UVR dosage level.

S. elongatus PCC 7942 has 2,723 genes in its 2.7 Mbp genome, of which 718 were previously determined to be essential (Rubin et al., 2015); thus, those mutants are absent from the library and were not sampled in this assay. Additional mutants that are known to be unfit in a light-dark cycle would also be lost from the population (Welkie et al., 2018). The disruption of 5 of the remaining genes conferred a strong decrease in fitness specifically under the HUV condition relative to the PAR-only condition (log-2-fold < -1.0; FDR adjusted *P* value < 0.05), and mutants of 14 additional genes were had a moderate decrease in fitness (log-2-fold < -0.5; FDR adjusted *P* value < 0.05), (**Figure 2.3**). The top 5 mutant loci that strongly decreased fitness are *Synpcc7942_1190*, *Synpcc7942_0112, Synpcc7942_1945*, *Synpcc7942_1679*, and *Synpcc7942_1616*. These genes are currently annotated as encoding a leucyl-aminopeptidase (LAP), a deoxyribodipryrimidine photo-lyase, an excinuclease ABC subunit C, a photosystem II reaction center W protein, and a hypothetical protein, respectively. A strong increase in fitness was calculated for mutants in only 3 genes: *Synpcc7942_1628* (hypothetical protein), *Synpcc7942_0319* (hemolysin A), and *Synpcc7942_1933* (isopentenyl pyrophosphate isomerase). However, closer examination of the data revealed that the positive value resulted from exceptionally poor representation of these barcodes in the PAR-only sample rather than

enhanced growth in PAR + HUV. The same was true for other mutant loci that were identified as moderately improving fitness.

Figure 2.3. A volcano plot highlighting genes whose loss have moderate to strong fitness effects under HUV. Colors indicate whether loss of a gene causes an estimated fitness decrease (red) or increase (blue). A horizontal line indicates the p-value cutoff threshold, and dotted vertical lines indicate the cutoff thresholds for moderate and strong fitness effects (-1, -0.5, 0.5, and 1). Bold text highlights genes with the strongest fitness effects (< -1 or >1).

Four of the top five genes revealed by the RB-TnSeq screen to be important under HUV exhibited a fitness response that is linearly correlated with the UVR dosage incident on the mutant pools. For example, mutants defective for *Synpcc7942_1190* had a decrease in log-2-fold fitness values under HUV, MUV, and LUV of -2.1, -1.6, -0.9 [P <0.01, and false discovery rate (FDR) < 0.01; *t-test*], respectively. Only *Synpcc7942_1616* exhibited a dosage-independent response (HUV: -1.0, MUV: -1.1, LUV: -0.8).

The genes whose loss confers moderate to strong fitness decreases were classified and subsequently binned into functional groupings based on merged COG and CyoG databases. One

is classified as being involved in coenzyme transport and metabolism (*gshB*), 1 in energy production and conversion (*Synpcc7942_0567*), 1 in nucleotide transport and metabolism (*codA*), 3 in photosystem II (*psb27, psb28-1, psbJ*), 1 in post-translational modification and protein turnover (*ppiB*), 3 in replication, recombination, and repair (*phr*, *uvrC*, *ssb*), and 1 in translation (*miaA*); 8 were unclassified by the database (*lap*, *Synpcc7942_1616*, *Synpcc7942_0037, Synpcc7942_2194, Synpcc7942_B2641, Synpcc7942_1812*, *Synpcc7942_B2643, Synpcc7942_1511*). Given that the strongest decrease in fitness observed under our HUV condition was conferred by mutations in *Synpcc7942_1190*, *lap*, encoding a putative leucyl amino peptidase, we assessed the phenotype of a *lap* knockout mutant in *S. elongatus*, and performed kinetic assays of the LAP protein.

LAP knockout phenotype verification and complementation

To validate the UVR-sensitive phenotype identified by the RB-TnSeq screen, a fully segregated insertion mutant of *lap* with a kanamycin-resistance marker was generated (∇*lap*) and grown in co-culture with a WT strain containing a spectinomycin-streptomycin marker integrated at a genomic neutral site (WT::SpSm^R) for 8 days under both the PAR-only control and HUV conditions used in the library screen. Samples were collected daily and plated on both kanamycin and spectinomycin-steptomycin selective media, and colony forming units (CFUs) were used to calculate growth rates (**Figure 2.4**). There was no statistical difference in growth rate under the PAR-only condition; however, growth of the ∇*lap* mutant was significantly inhibited under HUV relative to the WT ($p < 0.05$; **Figure 2.4A and 2.4B**). To ensure that the phenotype of the ∇*lap* mutant is not the result of a second-site mutation elsewhere in the genome, the ∇*lap* mutant was complemented with a segment of DNA extending from 243 bp

upstream to 71 bp downstream of *SynPCC7942_1190* inserted into a neutral site of the genome (∇*lap*::*lap*). When spotted and grown on BG-11 agar, the WT phenotype was restored in the ∇*lap*::*lap* strain (**Figure 2.5A**). To assess whether the ∇*lap* mutant experienced enhanced sensitivity due to the dark period of the light-dark cycle in combination with prior UVR exposure, an identical experiment was conducted between the ∇*lap* mutant and the WT under constant light, with the UVR lamp active during the same 6-h exposure period as in previous studies. While the CFU circumference of the ∇*lap* mutant was reduced relative to the WT, the UV-sensitive phenotype, as assessed by reduced CFU viability in the 12-h light: 12-h dark + UVR condition, was alleviated. This result indicates that the lethality of a *lap* insertional mutant relative to the WT when exposed to UVR is enhanced under the ecologically relevant condition of a subsequent period of darkness **(Figure 2.5B**).

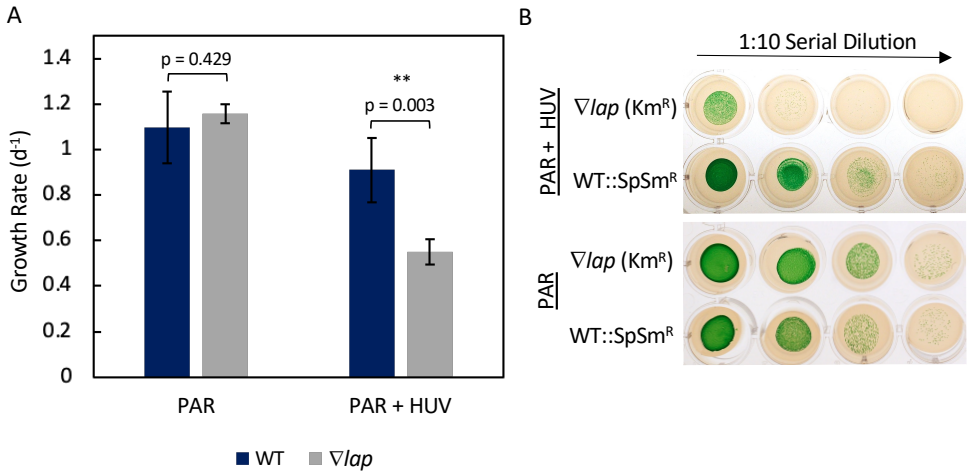

Figure 2.4. Results of a co-culture growth competition between a *lap*-deficient mutant and the WT strain. A) Growth rates under the PAR only and PAR + UVR condition. B) CFUs from spots of the co-culture under PAR and PAR + UVR conditions after 7 days of growth, plated on selective media. Data points are mean (SD); n = 3.

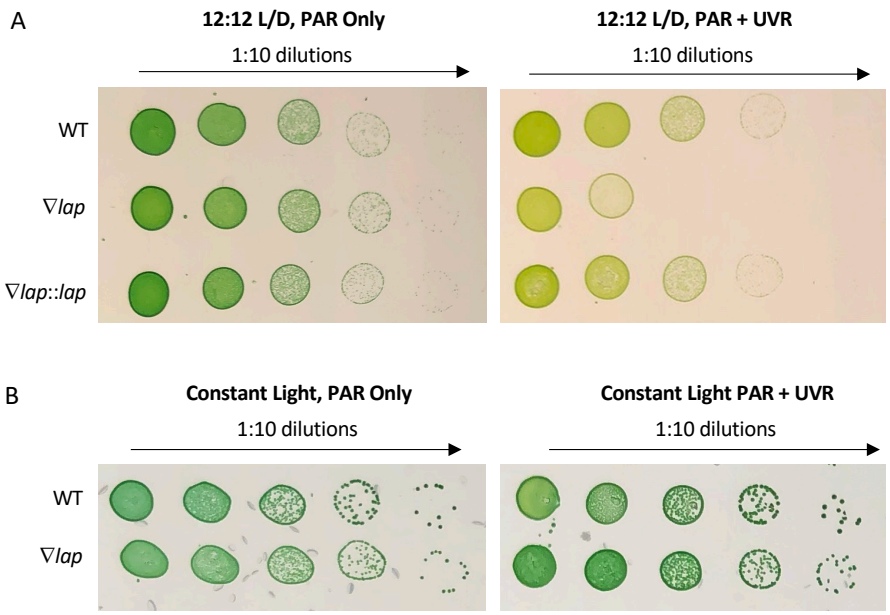

Figure 2.5. Spot tests reveal that the *lap* mutant can be complemented, and that the sensitivity to UVR is enhanced in a light:dark cycle relative to constant light. 5 µl spots of the WT and mutant strains of *S. elongatus* grown under PAR only, or PAR and HUV. A) Cells grown under 12-h light:12-h dark cycle. B) Cells grown under constant light, with UVR present for 6 h per day.

Recombinant expression and purification of SynPCC7942_1190 in E. coli*, and characterization of enzymatic properties*

SynPCC7942_1190 is predicted to be of the M17 family of proteases and function as an LAP; however, prior research has shown that some LAPs have Cys-Gly hydrolase activity. Given that Cys-Gly is a metabolite produced during the two-step catabolism of glutathione, and glutathione synthase was identified as an important enzyme for fitness under UVR, we investigated the enzymatic properties of SynPCC7942_1190. The recombinant protein was overexpressed in *Escherichia coli*, and the purified 51 kDa protein migrated as a single band of the expected size on an SDS gel (**Figure 2.6A**). The substrate specificity of SynPCC7942_1190 was then assessed against Cys-Gly and L-Leucine-p-nitroanilide (L-leu-p-NA) at pH 7.5. Using Cys-Gly as a substrate, a K_m of 1.21 mM was observed, whereas experiments with L-leu-p-NA

yielded a K_m of 7.44 mM (**Figure 2.6E**). No activity was detected against various other substrates including cystine (Cys-Cys), Glycylglycine (Gly-Gly) or glutathione (Glu-Cys-Gly), suggesting specific and preferential Cys-Gly affinity for SynPCC492_1190 at pH 7.5 despite exhibiting leucyl-aminopeptidase activity (**Figure 2.6B**).

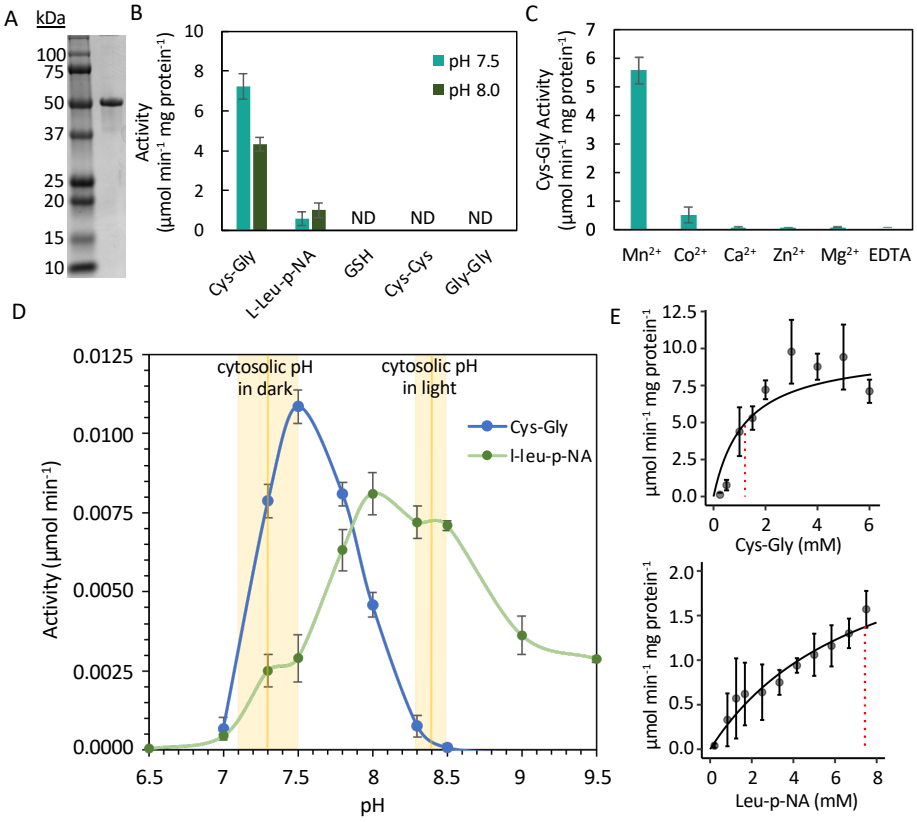

Figure 2.6. Kinetic assays of recombinant Synpcc7942_1190 Lap protein reveal preferential affinity for cysteinyl-glycine. A) SDS gel of the 51 kDa recombinant Synpcc7942_1190 Lap protein. B) Activity of the recombinant protein against various substrates, at pH 7.5 and 8.0. C) Activity of the recombinant protein against cysteinyl-glycine in the presence of metal cofactors. D) Activity of the recombinant protein against cysteinyl-glycine and L-Leucine-p-nitroanilide over a pH gradient. Average intracellular pH levels of *S. elongatus* in the dark and light are overlaid, per Mangan *et al.* (22). E) Samples containing 5µg/ml of the recombinant protein were assayed for cysteinyl-glycine or L-Leucine-p-nitroanilide at different substrate concentrations at pH 7.5. Km values are overlaid vertically as red dotted lines. Data points are mean (SD); n = 3.

Given that the M17 family of proteases are metalloproteases, the purified protein was tested to determine metal requirements for Cys-Gly activity. In the presence of EDTA, no

activity was observed (**Figure 2.6C)**. Maximal activity was observed with the addition of Mn^{2+}, and a small degree of activity was observed with the addition of Co^{2+}. No activity was observed with the addition of Ca^{2+}, Zn^{2+}, or Mg^{2+}.

To assess the effect of pH on the activity of the enzyme, both Cys-Gly and L-leu-p-NA were tested as substrates across a pH gradient from 6.5 to 9.5 (**Figure 2.6D)**. Maximal enzymatic activity against Cys-Gly was observed at pH 7.5, while maximal activity against L-leu-p-NA occurred at pH 8.0. The enzyme was not as sensitive to pH changes against L-leu-p-NA when compared to Cys-Gly, similar to results published previously for an LAP from the pathogenic bacterium *Treponema denticola* (Chu et al., 2008).

Synpcc7942_1190 *is conserved across ecologically relevant phytoplankton and knockout phenotype is conserved across prokaryotic species*

Proteins with strong sequence similarity to Synpcc7942_1190 were identified using BlastP (Altschul et al., 1997) against the genomes of select ecologically relevant phytoplankton that are present in surface waters, such as *Fragilariopsis cylindrus*, *Prochlorococcus marinus*, *Pseudo-nitzschia multistriata*, *Symbiodinium sp.* CCMP2592, *Synechococcus sp.* WH7803, and *Trichodesmium erythraeum*. In each homologous protein, conservation of amino acids at the seven resides canonically involved in M17 family metal binding and catalysis were identified (**Supplementary Figure 2.1**).

To test whether the UV-sensitive phenotype of the LAP-deficient mutant is observable among diverse species, deletion mutants of genes that encode the characteristic M17 family peptidase domains found in *S. elongatus* LAP were generated in model organisms *Anabaena* sp. PCC 7120 (Δ*RS03160*) and *E. coli* (Δ*pepA*). The *E. coli* LAP gene chosen for this study was

previously described to confer cysteinyl-glycinase activity in *E. coli* K-12 (Suzuki et al., 2001). Relative to the WT strain, the *Anabaena* sp. PCC 7120 Δ*RS03160* mutants produced fewer CFUs when grown under UVR in a 12-h light: 12-h dark cycle relative to white light only, indicating conservation of the UV-sensitive phenotype across species of cyanobacteria (**Figure 2.7A**). Similarly, the *E.coli* Δ*pepA* mutant resulted in reduced colony forming units when grown under UVR relative to white light only and the respective WT controls (**Figure 2.7B**), indicating the conservation of the UVR-sensitivity phenotype of LAP knockouts broadly across prokaryotic genera. Additionally, to test whether the *lap* gene from *Anabaena* sp. PCC 7120 (*RS03160*) could be used to complement the ∇*lap* strain of *S. elongatus*, *RS03160* was cloned under the regulation of a P*trc* promoter and introduced into a neutral site of the chromosome in the ∇*lap* strain of *S. elongatus*. When spotted and grown on BG-11 agar, the WT phenotype was restored in the ∇*lap*::*RS03160* strain, corroborating conservation of the UVR-tolerance mechanism in a leucyl aminopeptidase across cyanobacterial species (**Figure 2.7C**).

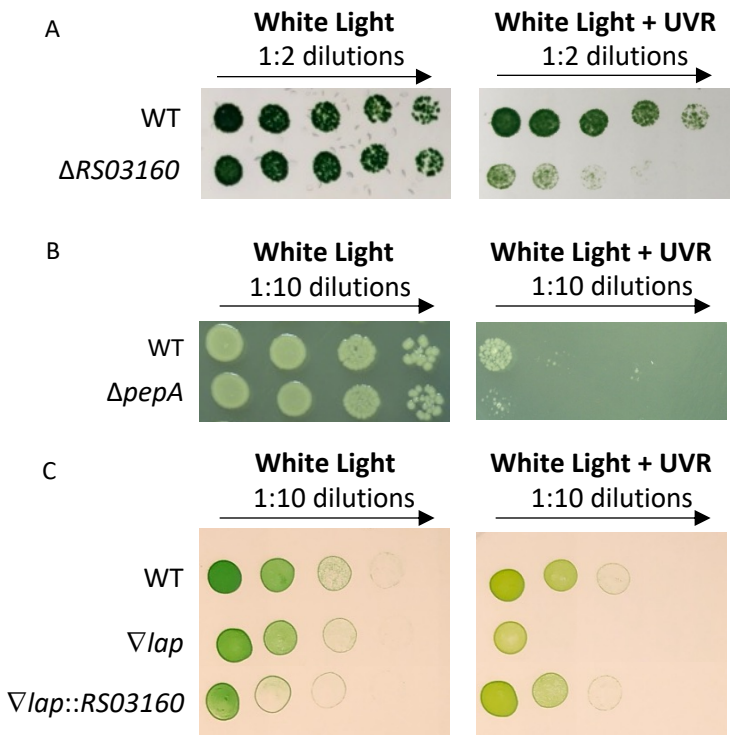

Figure 2.7. Spot tests reveal conservation of UV-sensitivity in LAP deficient mutants in a diversity of organisms. A) 5 µl spots of wild-type *Anabaena* sp. PCC 7120 and a markerless LAP mutant (Δ*RS03160*) grown under white light with or without UVR for 11 days. B) 5 µl spots of WT *E. coli* K-12 and Δ*pepA* grown under white light with or without UVR for 24 h. C) 5 µl spots of wild-type *S. elongatus,* the ∇*lap* mutant, and the ∇*lap* mutant complemented with an LAP from *Anabaena* sp. PCC 7120 (∇*lap*::*RS03150*), grown under white light with or without UV.

Discussion

As expected from previous work, many genes that contribute strongly to UVR tolerance belong to functional families related to DNA repair, maintenance of the photosynthetic apparatus, and antioxidant cycling. This work identified an unexpected protein, the M17 family aminopeptidase LAP encoded by *Synpcc7942_1190*, as the strongest determinant of fitness under all UVR dosage conditions.

LAPs preferentially catalyze the hydrolysis of leucine residues at the N-terminus of peptides and proteins and are often thought of as housekeeping enzymes. In addition to this

functionality, LAPs have distinct and complex roles in diverse organisms ranging from bacteria to higher eukaryotes. For example, LAPs are involved in oxidative lens aging in *Bos taurus* (Sharma and Ortwerth, 1986; Cappiello et al., 2004), serve as a defense protein in *Lycopersicon esculentum* (Fowler et al., 2009; Scranton et al., 2013), are a central component of H_2S production which may be important for pathogenesis in *T. denticola* (Chu et al., 2008), and aid the decay of particulate organic matter in marine systems (Caruso and Zaccone, 2000). No LAPs in general, let alone LAPs conferring cysteinyl-glycinase activity, have been previously implicated as a critical factor in UVR tolerance. This study demonstrated that the *S. elongatus* LAP is capable of the hydrolysis of cysteinyl-glycine in addition to the expected activity against dipeptides containing leucine moieties. Several aminopeptidases from *E. coli* K-12, including PepA, PepB, PepD, and PepN, have been shown to confer cysteinyl-glycinase activity (Suzuki et al., 2001), and LAP cysteinyl-glycinase activity has also been reported in LAP purified from bovine lens, *Arabidopsis thaliana*, rat liver, and the pathogenic bacterium *T. denticola* (Jösch et al., 2003; Cappiello et al., 2004; Chu et al., 2008; Kumar et al., 2015).

While the LAP demonstrated broad activity against l-Leu-p-NA across the pH gradient tested, there was no Cys-Gly hydrolase activity detected at pH levels at or above 8.5. Previous measurements of the cytosolic pH of *S. elongatus* have identified an increase in cytosolic pH from 7.3 ± 0.2 in the dark to 8.4 ± 0.1 in the light, due to H^+ pumping from the cytosol into the thylakoid lumen triggered by photosynthetic activity (Mangan et al., 2016). The results presented here suggest that, while the LAP may be functionally active as a leucyl aminopeptidase across all intracellular pH levels, it may preferentially moonlight as a cysteinyl-glycinase when the cell is exposed to darkness. A similar phenomenon of pH dependance has been demonstrated for ribulose bisphosphate carboxylase/oxygenase (RuBisCO) and has been suggested for the

regulation of chaperone function during light–dark cycles in *S. elongatus* (Mangan et al., 2016; Akter and Nakamoto, 2021).

During the catabolism of glutathione (GSH), GSH is initially cleaved into glutamate and Cys-Gly by a gamma-glutamyltransferase (GGT), and Cys-Gly is subsequently degraded into glycine and cysteine by a cysteinyl-glycinase. Previous work in *Synechocystis* sp. PCC 6803 demonstrated that the onset of darkness triggers glutathione catabolism (Cameron and Pakrasi, 2010). The affinity of the *S. elongatus* LAP towards cysteinyl-glycine under pH levels that are representative of the cytosolic pH during darkness likely facilitates the complete catabolism of glutathione during the dark period. The improved survival in UVR of the ∇*lap* mutant under constant light relative to a light-dark cycle provides further evidence this enzyme's relevance to UVR tolerance is most pronounced during the dark period and reduced cytosolic pH levels. The broader pH range of activity of the purified SynPCC7942_1190 enzyme against l-leu-p-NA supports the premise that this enzyme has a basal activity against peptides containing leucine moieties and moonlights as a cysteinyl-glycinase in darkness.

There are several arguments for importance of a complete glutathione catabolism pathway in *S. elongatus*. Cysteine appears to be the main limiting amino acid for glutathione synthesis, in addition to being an important source of sulfur for other thiols and general cell metabolism in cyanobacteria (Fahey, 2001; Copley and Dhillon, 2002; Masip et al., 2006). Additionally, it has been proposed that Cys-Gly has important redox properties and can be toxic in high quantities. This toxicity is likely due to the pro-oxidant nature of Cys-Gly, as it is a more reactive thiol than GSH, capable of starting iron redox-cycling processes that produce ROS and subsequent oxidative reactions (Paolicchi et al., 2002). In the absence of a complete or efficient catabolism cycle, there is potential for the buildup of the dipeptide Cys-Gly within the cell,

which results in a paucity of free cysteine and glycine. Abundant Cys-Gly would simultaneously create a pro-oxidant environment and a lack of Cys substrate to reallocate towards glutathione-dependent mechanisms of tolerance of oxidative stress conditions. It is possible that the severe fitness defect under UVR upon loss of this gene is due to the enzyme's dual role as a housekeeping leucyl aminopeptidase by day, and a cysteinyl-glycinase by night.

Previous screens of microorganisms have not implicated a cysteinyl-glycinase or leucyl aminopeptidase as being major factors in UVR tolerance. The lack of differential expression of *lap* upon acute UVR exposure may explain this oversight in screens that have relied upon transcriptomic data (**Figure 2.2**). Furthermore, the survival of *lap* insertional mutants under the constant light + UVR condition suggest that the strong UV-sensitive phenotype in *S. elongatus* would require subsequent exposure to a dark period to be detected; thus, this phenotype may be overlooked in screens that focused on acute UVR exposure to photosynthetic organisms, or UVR exposure under constant light.

Cyanobacteria such as *Prochlorococcus marinus* and marine *Synechococcus spp.*, which dominate vast oceanic areas, and other ecologically relevant phytoplankton such as the diazotroph *Trichodesmium erythraeum*, Bacillariophyceae such as *Fragilariopsis cylindrus* and the domoic acid producing diatom *Pseudo-nitzschia multistriata*, and the dinoflagellate photosymbiont of corals *Symbiodinium microadriaticum,* all harbor LAPs with strong sequence similarity to Synpcc7942_1190 and identical amino acids at the seven residues canonically involved in M17 family metal binding and catalysis (**Supplementary Figure 2.1**). This conservation of functional residues suggests that LAPs may support UVR stress tolerance in key primary producers residing in upper mixed layers of marine systems. The conservation of the UV-sensitive phenotype of LAP knockout strains in *E. coli* and *Anabaena* sp. PCC 7120 support

that LAPs may serve a UVR-tolerance role in a diversity of organisms. It is possible that the *E. coli* LAP tested in this study may not be subject to the same pH dependent mechanism as the phototrophic *S. elongatus* LAPs yet is nevertheless important under UVR stress.

The only gene other than *Synpcc7942_1190* that confers moderate to strong fitness and has an obvious connection to the antioxidant cycling functional family is *gshB*, encoding glutathione synthase. GSH is canonically synthesized through two sequential ATP-dependent steps, catalyzed by Glu-Cys ligase (*gshA*) and *gshB*; however, no homolog of *gshA* has been identified in *S. elongatus* PCC 7942. When GSH is oxidized (GSSG), it can be recycled back to GSH via glutathione reductase (*gor; Synpcc7942_0842*); however, mutation of *gor* had no more fitness cost under UVR stress than in white light alone. GSH is thought to be the major antioxidant present in cyanobacteria, playing a central role in ROS scavenging by providing electrons to various GSH-dependent enzymes (Rai et al., 2021). Δ*gshB* strains of *Synechocystis* sp. PCC 6803 have severe growth retardation in the presence of H_2O_2, as well as other forms of ROS, at concentrations that do not affect the WT or complemented strains, indicating that GSH is crucial for protection against diverse ROS species (Cameron and Pakrasi, 2010). Glutathione levels can be modulated by both light spectra and intensity in cyanobacteria (Singh et al., 2009; Cameron and Pakrasi, 2010). Our results confirm the critical nature of GSH synthesis in *S. elongatus* under UVR and suggest that a complete catabolic cycle of GSH is necessary under natural conditions that involve UVR and a light-dark transition in *S. elongatus* as well as *Anabaena sp.* PCC 7120 and other microorganisms.

The two genes from the DNA repair functional family that strongly affect fitness under UVR are *phr*, encoding a deoxyribodipyrimidine type I photo-lyase, and *uvrC*, encoding excinuclease ABC subunit C. Deoxyribodipyrimidine photo-lyases catalyze the light-dependent

repair of cyclobutyl pyrimidine dimers that form between adjacent DNA bases. Cyanobacteria from high-light biotopes tend to possess Phr, whereas those from low-light biotopes may not (Biller et al., 2015). Phr is important for resistance against UV-C radiation in *S. elongatus*; however, its enzymatic activity requires a light period following UVR exposure to drive catalysis, as would be experienced by an organisms in the natural environment (Kawasaki and Iwasaki, 2020). Our attempt to recreate a natural midday UVR exposure environment in the lab detected *phr* as critical for fitness. The UvrABC endonuclease enzyme complex proteins are encoded in all analyzed cyanobacterial genomes, supporting a core role in DNA repair (Cassier-Chauvat et al., 2016). In *E. coli* UvrA initiates contact with damaged DNA, transfers the DNA to UvrB, and UvrC creates incisions around the damaged site. Subsequently DNA helicase II releases the incised nucleotide (Truglio et al., 2006). Interestingly, in this study, *uvrC* was the only gene of the UvrABC complex to display a strong fitness effect (*uvrA* 0.15 ± 0.03 $p < 0.05$, *uvrB* -0.03 ± 0.08, *pcrA* -0.05 ± 0.23, under HUV). This result suggests redundancy and interchangeability of the functions of UvrA and UvrB.

The results of this screen suggest that the photosynthetic functional family genes *psb27*, *psb28-1*, and *psbJ* are fundamental for tolerating UVR stress in a cyanobacterium, likely by promoting the assembly and/or repair of PSII. Psb27 and Psb28-1 are needed for optimal growth under intermittent high-light/dark conditions, and Psb28-1 appears to be important for the synthesis of chlorophylls and apoproteins of chlorophyll-binding proteins (Roose and Pakrasi, 2008; Dobáková et al., 2009; Liu et al., 2011; Nowaczyk et al., 2012; Pagliano et al., 2013; Bečková et al., 2017). While two paralogs of Psb28 are present in *S. elongatus* (Psb28-1 and Psb28-2), *psb28-2* mutants conferred no observable fitness change under UVR stress in our screen, corroborating previous reports that Psb28-2 may serve an alternative function (Sakata et

al., 2013). PsbJ mutants have light-sensitive phenotypes due to improper assembly of PSII cores and deregulated electron flow, in addition to an accumulation of Psb27- and Psb28-containing PSII intermediates (Regel et al., 2001; Hager et al., 2002; Nowaczyk et al., 2012). Here, we identify these 3 photosystem genes as being of importance for UVR tolerance.

None of the genes identified as critical for fitness under UVR stress by the RB-TnSeq experiment, with the exception of *Synpcc7942_1511* (fitness estimate -0.5), was differentially expressed following an acute 15-min exposure to the HUV period (**Supplementary Figure 2.2**). This highlights that studies focusing on differential expression at discrete timepoints may overlook many genes that are important for UVR tolerance. Three genes important for UVR fitness were downregulated after 2 h of HUV exposure: *Psb28-1*, *Psb27* and *Synpcc7942_1616*. This decrease in expression was observed in tandem with a global downregulation of genes involved with photosystems I and II and phycobilin-containing light-harvesting complexes. This downregulation by UVR may decrease photosynthetic activity, with subsequent upregulation to be expected late in the dark period in anticipation of dawn. Notably, the hypothetical protein encoded by *Synpcc7942_1616* previously has been detected in PSI and PSII pulldown experiments, which when taken with the results of the RB-TnSeq experiment, suggests a potentially overlooked and important role of Synpcc7942_1616 in association with photosystem complexes (Zhang et al., 2021).

The results of this study define the gene set that is critical for UVR tolerance under environmentally relevant UVR conditions in a model photosynthetic organism. It is likely that essential genes, such as superoxide dismutase, which are not assayed with the RB-TnSeq library, are also important for fitness under UV stress, and that relevant genes with redundant homologs may have escaped detection. While the importance of such genes should not be overlooked, the

utilization of an RB-TnSeq library in *S. elongatus* under realistic UVR conditions has corroborated the importance of several canonical gene functional families to UVR tolerance, such as DNA repair, photosystem maintenance, and glutathione synthesis, and highlighted the key role of a previously overlooked leucyl-aminopeptidase with cysteinyl-glycinase activity, which may be conserved among many ecologically relevant phytoplankton.

Materials and Methods

Growth Conditions and Initial Growth Experiments

Synechococcus elongatus PCC 7942, stored in our laboratory as AMC06, (*S. elongatus*) was grown to an initial OD_{750} of 0.6, and 50 mL of culture was inoculated in triplicate into quartz bioreactors (100 mL, outer diameter 30 mm, inner diameter 25 mm, length 200 mm). The bioreactors were suspended above white LED panels with diffusion screens at an incident intensity of 160 μmol photons$\cdot m^{-2} \cdot s^{-1}$ at the bottom of the bioreactors. Two Q-Lab UV-A 340 lamps (QUV-UV-A340, Q Lab, Westlake, OH, USA) were positioned perpendicular to the white LED panels. The tubes were positioned at various distances from the UV lamps, in triplicate, resulting in the following UVR conditions: high UVR (HUV, 1 mW$\cdot cm^{-2}$), medium UVR (MUV, 0.6 mW$\cdot cm^{-2}$), and low UVR (LUV, 0.4 mW$\cdot cm^{-2}$). UVR levels were measured with a Solarmeter® Model 5.0 Standard UVA+B Meter. A control group, PAR alone, was created by wrapping a single layer of Edmund Polyester High-pass UV Filter Sheet (<10% transmission below 390 nm) around 3 bioreactors positioned at the same distance from the UVR source as the LUV condition. All bioreactors were bubbled with ambient air filtered through a 0.2 μm filter and subjected to a 12-h light:12-h dark regime, with activation of the UV lamp during the central 6 h of the light period to mimic highest UVR exposure during the midday solar zenith. OD_{750}

was continually monitored, and cultures were diluted at an OD_{750} of ~0.3 to maintain the optical thinness of the cultures, limiting the maximum attenuation of UVR across the 25 mm reactor to less than 30%.

Growth Rates and Absorption Spectra

S. elongatus was grown to an initial OD_{750} of 0.6, and 50 mL of culture was inoculated in triplicate into quartz bioreactors at an OD_{750} of 0.025. Growth rates were determined by measuring OD_{750} daily. Additionally, absorption spectra from 300 - 800 nm were recorded on a Tecan Infinite M200 plate reader, with BG-11 media used as a blank, and corrected to 0 at 750 nm. The spectra were normalized to the local maximum at 675 nm.

Reactive Oxygen Species (ROS)

The fluorescent marker 2',7'-dichlorodihydrofluorescein diacetate (H_2DCFDA) was used following the methods described in Rastogi *et al*. (Rastogi et al., 2010). 2.5 µL of 2 mM H_2DCFDA was added to 1 mL of sample for a final concentration of 5 µM and incubated at 30 °C for 30 min. The fluorescence was then quantified at an excitation of 480 nm and an emission of 520 nm on a Tecan Infinite M200 plate reader with the gain manually set to 120. Fluorescence data were normalized to OD750 for each sample, and untreated-sample background fluorescence was then subtracted from treated-sample fluorescence values.

RB-TnSeq Library Growth and Sampling

A 1ml aliquot of an *S. elongatus* PCC 7942 RB-TnSeq library, previously archived at -80 °C, was quickly thawed for 2 min at 37 °C, resuspended in 2 flasks of 100 ml BG-11 with

kanamycin (Km), and incubated at 30 °C for 1 day at 30 μmol photons·m^{-2}·s^{-1} without shaking (Rubin et al., 2015). The culture flasks were then transferred to 70 μmol photons·m^{-2}·s^{-1} on an orbital shaker. The cultures were subjected to a 12-h light:12-h dark regime for entrainment for 2 days, until the OD_{750} reached 0.25. The cultures were then combined and diluted to an OD_{750} of 0.025, and four replicates of 15 mL were spun down at 4,500 x g and frozen at -80 °C as time 0 samples to determine the population baseline. Aliquots of 50 mL of the RB-TnSeq outgrowth were then transferred to 12 quartz tubes and grown in identical conditions to the preliminary growth experiments for 5 generations. 15 mL of culture from each tube was subsequently collected by centrifugation at 4,500 x g, and DNA was extracted from the pellet using a phenol-chloroform extraction (Clerico et al., 2007).

Barseq

The method for Barseq analysis was conducted as previously described (Wetmore et al., 2015). In brief, amplification of barcodes from extracted DNA was conducted using 1 of 96 indexed forward primers for multiplexing, BarSeq_P2_ITXXX, and a common reverse primer, BarSeq_P1. PCR was performed in a final volumes of 50 μl using Q5 DNA polymerase, Q5 GC Enhancer (New England Biolabs), and the following thermocycler conditions: (i) 98 °C for 4 min, (ii) 25 cycles of 30 s at 98 °C, 30 s at 55 °C, and 30 s at 72 °C, (iv) and a final extension at 72 °C for 5 min. 10 μl of each PCR product was then combined, purified with a DNA Clean & Concentrator Kit (Zymo Research), and quantified using a Nanodrop 2000 Spectrophotometer (Thermo Scientific). The pooled and purified product was then sequenced using Illumina HiSeq4000 SR75 by the IGM Genomics Center at the University of California San Diego.

Fitness Calculations

Fitness values were calculated using a previously described R script (Welkie et al., 2018). In brief, the number of reads for each sample was used as a normalizing factor between samples. Any barcode falling outside or within the peripheral 20% of a gene coding sequence was ignored. Of the remaining barcodes, any genes represented by fewer than 3 barcodes were removed. For each barcode in each sample, a pseudocount of one was added to the number of reads, divided by the total number of reads for the sample, and the sample-normalized number of reads was log-2 transformed. Any gene without at least 15 T0 reads was also removed. For each gene, maximum-likelihood was used to fit a pair of nested linear mixed effects models to the sample- and read-normalized log-2-transformed counts. Genes with significant fitness differences between the UVR condition and PAR only control were identified by comparing the difference in the $-2\cdot\log$ likelihoods of the models to a $\chi 2$ distribution with one degree of freedom, estimating a P value, accounting for multiple testing by the FDR method of Benjamini and Hochberg (Benjamini and Hochberg, 1995), and selecting those gene with adjusted P values less than 0.02. We took the contract of $C_{UVx} - C_{PAR}$ to be the estimated UV-specific fitness effect of knocking out a given gene. Mutants that had fitness effects below a confidence threshold (FDR adjusted p value < 0.05) were not included. Mutants with gene disruptions conferring a fitness effect of ≥ 1 or ≤-1 were classified as having a strong fitness effect, whereas mutants with gene disruptions conferring a fitness effect of ≥ 0.5 or ≤ -0.5 were classified as having a moderate fitness effect. Fitness scores of < 0.5 or > -0.05 were classified as having negligible fitness effects.

RNA-Seq Sampling and Library Preparation

S. elongatus was grown under the HUV and PAR conditions described for the initial growth and RB-TnSeq experiments for 3 days prior to sampling 15 min and 2 h after the onset of the UVR period. 10 ml of each sample were collected, and 2 ml of an ethanol-phenol stop solution was added on ice. Samples were centrifuged at 4,500 x g for 10 min at 4 °C, decanted, and the cell pellets were stored at -80 °C. Total RNA was isolated and purified using the Zymo Research Quick-RNA Fungal/Bacterial Microprep Kit from frozen cell pellets previously harvested according to the manufacturers' protocols. Ribosomal RNA was removed from 1 μg Total RNA with the use of a QIAseq FastSelect - 5S/16S/23S kit (Qiagen). The resulting rRNA-subtracted RNA preparations were made into libraries with the KAPA RNA HyperPrep kit incorporating short Y-adapters and barcoded PCR primers. The libraries were quantified with a fluorescent assay (dsDNA AccuGreen quantitation kit, Biotium) and checked for proper size distribution and average size with a TapeStation (D1000 Tape, Agilent). Library pools were then assembled and a 1X SPRI bead cleanup was performed to remove traces of carryover PCR primers. The final library pool was quantified and run on an Illumina NovaSeq6000 with a PE50 run configuration. The sequencing depth ranged from 8.8 to 12.8 million reads per sample.

RNA-Seq Differential Expression Analysis

Differential expression analysis was conducted using the following R packages: Rsamtool (R package version 1.30.0), GenomeInfoDb (R package version 1.14.0.), GenomicFeatures (Lawrence et al., 2013), GenomicAlignments, GenomicRanges (Lawrence et al., 2013) and DESeq2 (Love et al., 2015). The workflow was followed as described by Love et al. and the differential expression was performed using DESeq2. Differentially expressed genes

between the HUV and PAR condition were selected for an adjusted *P* value < 0.05 (Benjamini-Hochberg correction for multiple testing) and an absolute $\log_2$ of fold change equal to or greater than 2.

Construction of mutants and complemented strains

The plasmid for the insertional mutation of Synpcc7942_1190 (∇*lap*) was taken from the unigene set (UGS-24-F-1). The plasmid for complementation of the ∇*lap* mutant strain with the native *lap* gene and promoter (∇*lap*::*lap*) was created as follows: pAM5217, the destination vector for the gene for complementation, was generated via seamless assembly with a GeneArt® Seamless Cloning and Assembly Kit (Thermo Fisher Scientific) of individual parts pCVD020 (NS1-Tc, pAM4836), pCVD002 (SpSm, pAM4818), and pCVD015 (ccdb-SwaI), available from the Cyanovector system (Taton et al., 2014). pAM5217 was then digested with SwaI (NEB), and a Gibson assembly (NEB) between the linearized product and the PCR product of the region 243 bp upstream to 71 bp downstream of SynPCC7942_1190 was performed, forming plasmid pAM5816 (Table 2.1). The SynPCC7942_1190 PCR product was generated using the primer pair 5217-1190-F and 5217-1190-R using standard protocols (Supplementary Table 2). The *lap* mutant strain was then transformed with the with the pAM5816 plasmid.

Table 2.1. List of plasmids used in this study.

Plasmid Name	Description	Source
UGS-24-F-1	Unigene set plasmid for insertional mutation of Synpcc7942_1190	(Chen et al., 2012)
pCVD002	SpR, SmR gene carried on a CYANO-VECTOR device (Sp, Sm, Ap)	(Taton et al., 2014)
pCVD015	Counter selectable ccdB-based cloning cassette carried on a CYANOVECTOR donor plasmid (Ap)	(Taton et al., 2014)
pCVD020	*S. elongatus* NS1 carried on a CYANO-VECTOR donor plasmid (Ap, Tc)	(Taton et al., 2014)
pAM2991	One-step cloning vector for overexpression with Ptrc promoter (Sp, Sm)	(Ivleva et al., 2005)
pAM5217	Cloning vector generated by seamless assembly of pCVD002, pCVD015, and pCVD020 (Sp, Sm, Tc)	This study
pAM5572	RSF1010-based broad host range plasmid for genome editing using Cpf1/CRISPR technology (Sp, Sm)	(Taton et al., 2020)
pAM5799	pAM5572 with gRNA spacer sequence targeting *alr0236*, and homology regions flanking PCC7120DELTA_RS03160 (Sp, Sm)	This study
pAM5816	Plasmid for chromosomal integration of Synpcc7942_1190 and native promoter (Sp, Sm)	This study
pAM5835	pAM2991 with PCR product of PCC7120DELTA_RS03160 (Sp, Sm)	This study
pAM5836	Synpcc7942_1190 cloned into a pET-28b(+) vector backbone with Strep-tag appended on 3' end (Km)	This study

The plasmid for complementation of the *lap* mutant with the LAP derived from *Anabaena* sp. PCC 7120 (pAM5835) was created by linearizing pAM2991 (Addgene plasmid # 40248) (Ivleva et al., 2005) with EcoRI and BamHI, and performing a Gibson Assembly (NEB) between the linearized backbone and the PCR product of PCC7120DELTA_RS03160 (WP_010994414.1) using the primer pair 2991-A7120-LAP-F and 2991-A7120-LAP-R (Supplementary Table 2).

To generate the plasmid for the markerless deletion of a native LAP (PCC7120DELTA_RS03160) in *Anabaena* sp. PCC 7120, the oligos A7120_gRNA-LAP-F and A7120_gRNA-LAP-R were annealed to produce a guide RNA template and were cloned into the AarI site of the CRISPR/cfp1 containing plasmid pAM5572 (Taton et al., 2020) by Golden Gate cloning (Engler et al., 2008). The guide RNA-containing plasmid was digested with KpnI-HF (NEB) and dephosphorylated with Antarctic phosphatase, and the linearized backbone was gel purified. Homologous repair templates upstream and downstream of the target *PCC7120DELTA_RS03160* gene were generated by PCR with the primer pairs A7120-LAP-U-F/A7120-LAP-U-R and A7120-LAP-D-F/A7120-LAP-D-R and cloned into the linearized

backbone using a 3-part Gibson Assembly (NEB) (Supplementary Table 2). The final plasmid product (pAM5799) was verified by sequencing.

Transformation of *S. elongatus* was achieved using standard protocols (Clerico et al., 2007). Genotyping of *S. elongatus* was performed using colony PCR with Taq DNA Polymerase (NEB). Transformation of *Anabaena* sp. PCC 7210 was achieved by biparental conjugation (Elhai et al., 1997). Genotyping of *Anabaena* sp. PCC 7120 was performed using PCR with Q5 DNA Polymerase on DNA of isolate cultures extracted using phenol-chloroform (Clerico et al., 2007).

Recombinant expression and purification of SynPCC7942_1190 *from* E. coli

Two primers (pet28-linear-streptag-F and pet28-linear-streptag-R; Supplementary Table 2) were used to linearize a commercially available pET-28b(+) vector (Millipore Sigma) with sequence to encode a Strep-tag on the N-terminus of the protein product. An additional primer pair (pet28-1190-streptag-F and pet28-1190-streptag-R, Supplementary Table 2) was used to amplify *Synpcc7942_1190* with appropriate overhangs for subsequent Gibson Assembly (NEB). The resulting plasmid (pAM5836) was used to transform *E. coli* DH5α cells for plasmid generation and sequence confirmation. The plasmid was subsequently moved into *E. coli* BL21 (DE3).

Plasmid-bearing *E. coli* BL21 (DE3) strains were grown to OD_{600} of 0.5 with 50 mg/ml kanamycin before overnight induction of protein expression at room temperature by the addition of 200 μM isopropyl β-D-1-thiogalactopyranoside. Cells were then collected by centrifugation and the pellet was resuspended in 50 ml of StrepTactin wash buffer (50mM Tris-HCl, pH 8.0, 150mM NaCl, 5% glycerol). The resuspended cells were disrupted on ice by French Press, and

the lysate was clarified by centrifugation at 27,000 × g (Sorvall SS-34 rotor) at 4 °C for 30 min. Recombinant protein was purified using a StrepTactin XT Superflow resin column (IBA Lifesciences). The column was washed with 20x the column volume of StrepTactin wash buffer, followed by protein elution with same buffer containing 50 mM biotin, and collected in 6 elution aliquots. The elution aliquots were run on SDS-PAGE to assess purity, and the central 3 elution aliquots were pooled.

Enzymatic Assays

The standard reaction buffer for all cysteinyl-glycinase assays was 50 mM Tris-HCl (pH 7.5 or 8.0), 2mM Cys-Gly, and 0.2 mM $MnCl_2$, unless another pH, substrate concentration, or cation is indicated. The purified LAP protein was incubated at 5 μg/ml for 20 min at 37 °C and terminated with 5% TCA. The reaction product L-cysteine was measured as described by Gaitonde et al. (Gaitonde, 1967). L-cysteine concentrations were determined by absorbance at 560 nm, after subtracting a blank.

Leucine aminopeptidase activity was determined using L-Leu-p-NA (Millipore Sigma) as a substrate (Morty and Morehead, 2002). The standard reaction buffer for these reactions was 50 mM Tris-HCl (pH 7.5 or 8.0), 2mM L-Leu-p-NA, and 0.2 mM $MnCl_2$, unless another pH, substrate concentration, or cation is indicated. The purified LAP protein was incubated at 5 μg/ml for 20 min at 37 °C and terminated with 5% TCA. The concentration of the reaction product was determined by absorbance at 405 nm, after subtracting a blank. All assays were performed in triplicate.

LAP Sequence Alignment

Proteins with sequence similarity to Synpcc7942_1190 were identified using Blastp against the genomes of *Anabaena* sp. PCC 7120 (accession WP_010994414.1), *Fragilariopsis cylindrus* (accession OEU09452.1), *Prochlorococcus marinus* (accession WP_158467072.1), *Pseudo-nitzschia multistriata* (accession VEU35739.1), *Symbiodinium sp.* CCMP2592 (accession CAE7247217.1), *Synechococcus sp.* WH7803 (accession A5GN62.1), and *Trichodesmium erythraeum* (accession Q11A96.1). A multiple alignment of the amino acid sequences was conducted with Geneious Alignment in Geneious Prime version 2022.0.2.

Chapter 2 Supplemental Figures

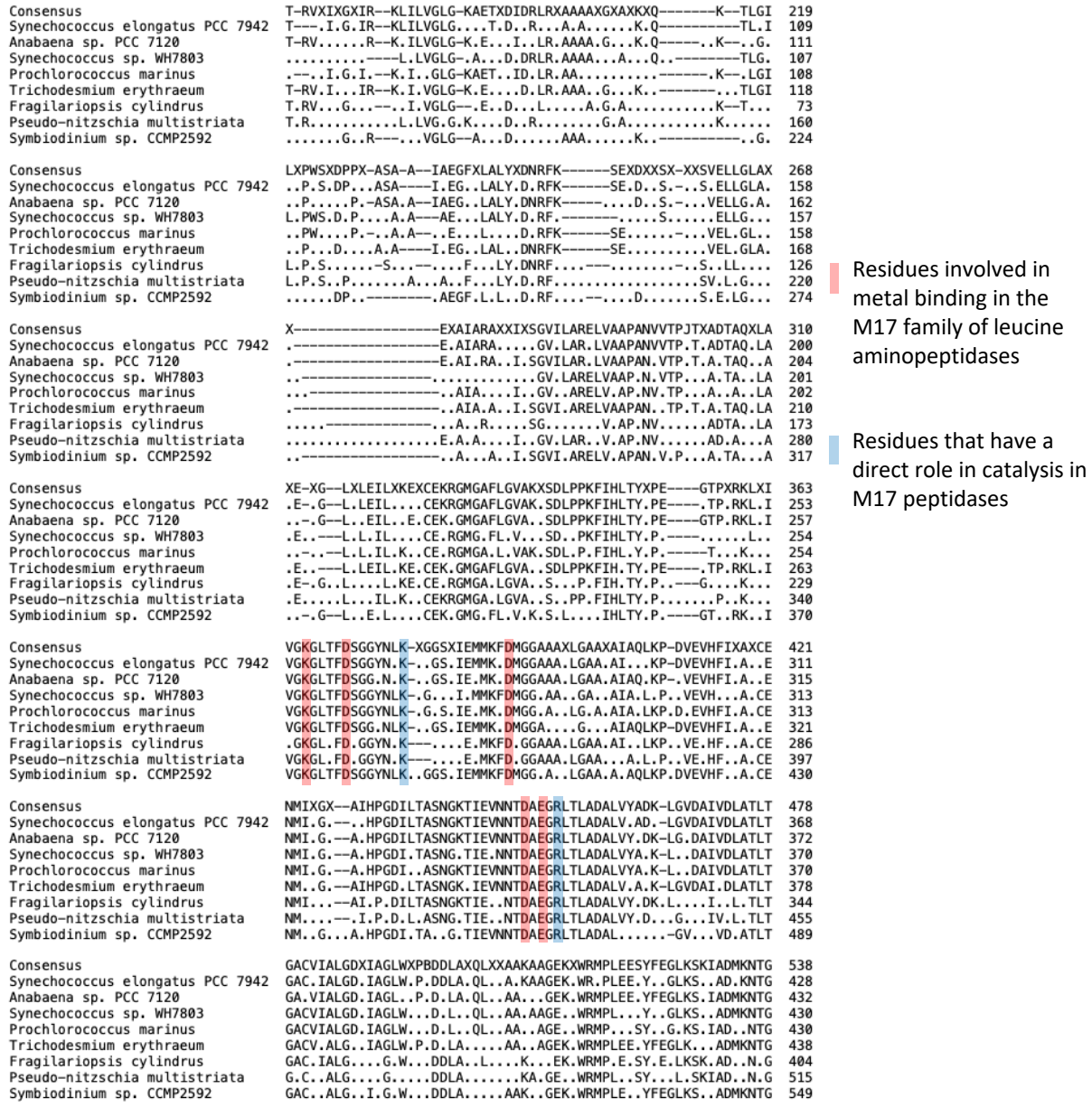

Supplementary Figure 2.1. A partial alignment of the *S. elongatus* LAP with BlastP matches from environmentally relevant phytoplankton, illustrating the conservation of amino acids at the seven residues canonically involved in M17 family metal binding and catalysis. Red column highlights indicate residues involved in metal binding in the M17 family of leucine aminopeptidases, and blue column highlights indicate residues that have a direct role in catalysis in M17 peptidases.

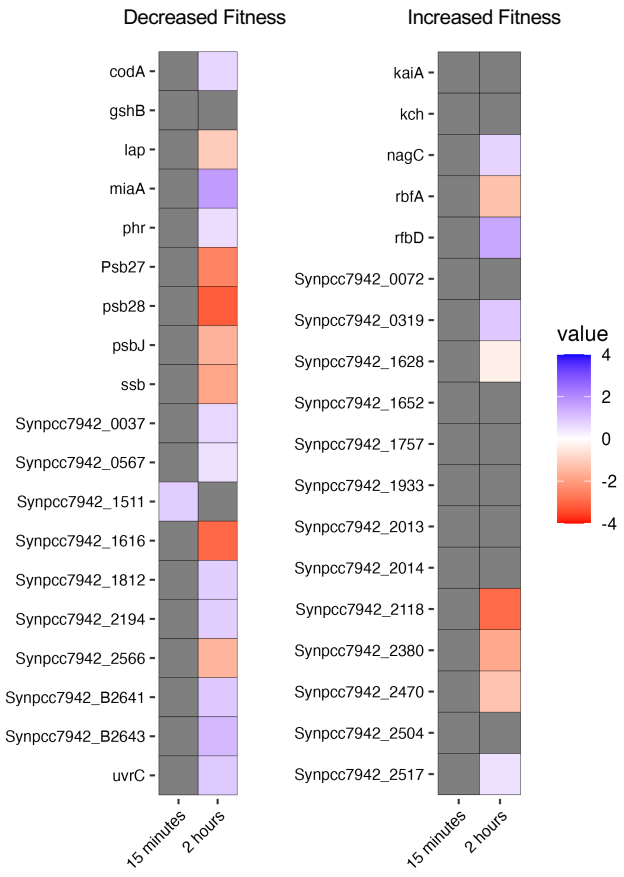

Supplementary Figure 2.2. Differential expression after 15 min or 2 h of HUV exposure of genes identified as conferring a strong increase or decrease when disrupted.

Acknowledgments

We thank David Welkie and Benjamin Rubin for consultation on experimental design, Emily Pierce for thoughtful comments on the manuscript, and Ryan Simkovsky for providing the assembled plasmid pAM5217. This work was funded by the National Science Foundation through the UC San Diego Materials Research Science and Engineering Center (DMR-2011924) and GRFP DGE-1650112 to ELW. SSG, MF, and AT were supported by the National Institute of General Medical Sciences of the National Institutes of Health under Award Number R35GM118290.

Chapter 2, in full, appears as submitted for publication as it may appear as Weiss EL, Fang M, Taton A, Szubin R, Palsson BØ, Mitchell BG, Golden SS. UV Tolerance Genes Revealed by a Genome-wide Fitness Assessment in a Model Cyanobacterium. The dissertation author was the primary investigator and author of this paper.

CHAPTER 3: The Distribution of Mycosporine-like Amino Acids in Phytoplankton Across a Southern Ocean Transect

Abstract

Interactions between phytoplankton and ultraviolet radiation (UVR: 280 – 400 nm) are undergoing changes dictated by variability in ocean temperature, the depth of mixed layers, nutrient availability, and the thickness of the ozone layer. There are a variety of mechanisms for phytoplankton to cope with UVR stress, one of the most prevalent being the presence of mycosporine-like amino acids (MAAs) that serve as a UVR-absorbing sunscreen. Despite the importance of these molecules to phytoplankton fitness under UVR stress, knowledge of the diversity and distribution of these molecules in the world's oceans is relatively limited. Here, the composition and distribution of MAAs in phytoplankton were examined in a transect across the Southern Ocean, crossing multiple fronts, from eastern New Zealand to the West Antarctic Peninsula in March and April of 2018. The highest concentration of MAAs (> 0.2 μg/L) were found between 50 and 60 °S, as well as along a longitudinal gradient between 137.47 and 144.78 °W. A strong correlation was found between a model of the preceding month's UVR dosage experienced in the mixed layer and the ratio of MAAs to chlorophyll-a across the transect, indicating a relationship between the integrated history of light exposure and phytoplankton physiology. Haptophytes accounted for the majority of biomass north of the polar front (PF) and were strongly correlated with a diversity of MAAs. South of the PF a transition to a community dominated by diatoms was observed, with community composition changes strongly correlated to porphyra-334 concentrations. The data presented here provide a baseline for MAA abundance and association with specific phytoplankton taxa across the Southern Ocean amid a changing climate.

Introduction

Ultraviolet radiation (UVR: 280 – 400 nm) is the most photochemically reactive waveband of the incident solar radiation field and has profound effects on the physiology of organisms living at or near the Earth's surface. In aquatic environments, interactions between climate change, the ozone layer, and UVR are continually modulating the length of exposure of aquatic organisms to UVR as well as the spectral quality and balance of incident radiation (Erickson et al., 2015; Barnes et al., 2019). Changes in UVR exposure alter the physiology and productivity of phytoplankton, which likely have cascading effects throughout ecosystems (De Mora et al., 2000). Climate change and other environmental variables will play a large role in the exposure of aquatic organisms to UVR. The shoaling of upper mixed layers (UML) in some ocean regions due to increased water temperature, and deepening in others, will alter the dosage of UVR received by pelagic organisms. Additionally, increases in melting of glaciers and permafrost are increasing coastal dissolved organic matter (DOM) levels thereby enhancing UVR absorption, while prolonged exposure of DOM to UVR in shoaled mixed layers may enhance DOM bleaching (Barnes et al., 2019; Hood et al., 2020). While these processes undergo natural cycles, projections from climate change modelling experiments predict that stratification will increase and the depth of the UML will be reduced in the Southern Ocean (Constable et al., 2014), resulting in changes in UVR dosages experienced by phytoplankton. Updated climate models, such as RCP-6.0, indicate that the Antarctic ozone hole is expected to close, with springtime ozone levels returning to 1980 values by 2060 (World Meteorological Organization (WMO), 2018). However recovery rates depend on continued compliance with the Montreal protocol and recent findings of increased emission of

chlorofluorocarbon-11 from eastern Asia and relatively short-lived chloroform emissions from China, among others, may delay ozone recovery (Fahey et al., 2018; Fang et al., 2019; Harris et al., 2019).

UVR has both direct, and indirect mechanisms of damage to photosynthetic biota. Mechanisms are manifested in damage to DNA, proteins, pigments, inhibition of photosynthesis, nitrogen fixation, retardation of nutrient uptake and cell motility, and the formation of reactive oxygen species (De Mora et al., 2000). Over evolutionary time photosynthetic organisms have developed an array of coping strategies to minimize the direct and indirect damage from UVR such as avoidance of UVR via cilia, flagella, or buoyancy regulation, DNA repair, the production of antioxidants, the recycling and repair of damaged proteins, and/or the synthesis of photoprotective pigments and intracellular or extracellular sunscreen molecules (Häder et al., 2015).

Mycosporine-like amino acids (MAAs) are one such type of sunscreen molecule, widely distributed in terrestrial, freshwater, and marine environments, and found in many types of organisms such as bacteria, fungi, the ocular lenses of fish, and are frequently part of an overall strategy of phytoplankton to diminish the inimical effects of UVR (Lesser, 1996; Moisan and Mitchell, 2001; Shick and Dunlap, 2002). MAAs are one of the strongest UVR absorbing natural products (molar extinction coefficients ranging from 28,100–50,000 M^{-1} cm^{-1}), which are characterized by their low molecular weight, high solubility and polarity and are composed of a cyclohexenone or cyclohexenimine chromophore conjugated to an amino acid or its amino alcohol, with absorption maxima ranging from 310 to 362 nm (Schmid et al., 2004; Sinha et al., 2007; Wada et al., 2015; Orfanoudaki et al., 2019). MAAs act as an effective sunscreen against photo-inhibition and provide a defense against the photooxidative stress of UVR (Carreto and Carignan, 2011). In addition to their role as a sunscreen, certain MAAs have been assigned

antioxidant activity and roles in osmoregulation (Portwich and Garcia-Pichel, 1999; Rastogi and Incharoensakdi, 2014). The synthesis of MAAs can be induced by exposure to UVR, far-red light, high levels of visible light, and modulated by osmotic conditions as well as nutrient limitation (Portwich and Garcia-Pichel, 1999; Moisan and Mitchell, 2001; Llewellyn et al., 2020).

Patterns of MAA production in the environment may serve as bioindicators of UVR-induced stress in phytoplankton, as has been suggested for patterns of DNA-damage and pigmentation in zooplankton (Hessen, 1993). Additionally, absorption of UVR by MAAs may enhance future satellite taxonomic characterization via remote sensing of UVR spectral bands (Kahru and Mitchell, 1998; Kahru et al., 2021). Recently, Kahru et al. (2021) demonstrated that remote detection using UVR spectral bands was able to differentiate neighboring algal blooms of differing taxonomic composition, likely due to the presence of MAAs. Various studies have been conducted to assess phytoplankton MAA composition in coastal marine and freshwater systems and in laboratory cultures (Whitehead and Vernet, 2000; Llewellyn and Harbour, 2003; Carreto et al., 2018), yet little is known about the abundance and composition of MAAs throughout the world's oceans, as few studies have been conducted on large spatial scales. Such larger scale studies in existence include the Sub-Antarctic Zone south of Tasmania in 2007 (Oubelkheir et al., 2013), and a latitudinal gradient across the Atlantic Ocean in 2008 (Llewellyn et al., 2012). An enhanced understanding of the global distribution of MAAs, the chemotaxonomic association of MAAs with phytoplankton, and the dynamics between MAA biosynthesis and abiotic factors such as UVR dosage will help to inform remote sensing observations as more satellites are equipped with ocean color sensors in the UVR region. Additionally, an understanding of the utility of MAAs to serve as a bio-indicator of UVR radiation-induced stress may help to improve

ecosystem and biogeochemical models that incorporate spectral light and explicit radiative transfer to examine the role of the irradiance spectrum and pigments in establishing biogeography (Dutkiewicz et al., 2015). In this study, we provide the first continuous assessment of surface MAA composition and abundance across the Southern Ocean, in a transect from New Zealand to the West Antarctic Peninsula (WAP), and highlight correlations between MAA composition, phytoplankton taxonomy, and modeled UVR dosage in the upper mixed layer.

Materials and Methods

Transect description and sample collection

Surface samples were collected along a transect from 54.0233 °S, 176.0422 °W to 62.1282 °S, 56.1329 °W between 3/29/18 and 4/16/18 from the icebreaker RVIB Araon, during the 2018 ANA08D expedition of the Korean Polar Research Institute (KOPRI) from Christchurch, New Zealand to the WAP. The cruise track and sampling locations are illustrated in **Figure 3.1**. Discrete seawater samples were collected from the ship's uncontaminated seawater system, with intake located at 7 m depth. Sampling occurred both at regular intervals (every 12 hours), as well as at higher resolution along major hydrographic transitions. Transitions were identified using underway sea surface salinity and temperature observations collected using a Seabird Scientific SBE45 Thermosalinograph connected to the flow-through system, as well as satellite imagery of surface chlorophyll-a and sea surface temperature using Moderate Resolution Imaging Spectroradiometer (MODIS) satellite data. Additional samples were collected when crossing climatological (average) locations of sea surface fronts (Orsi et al, 1995).

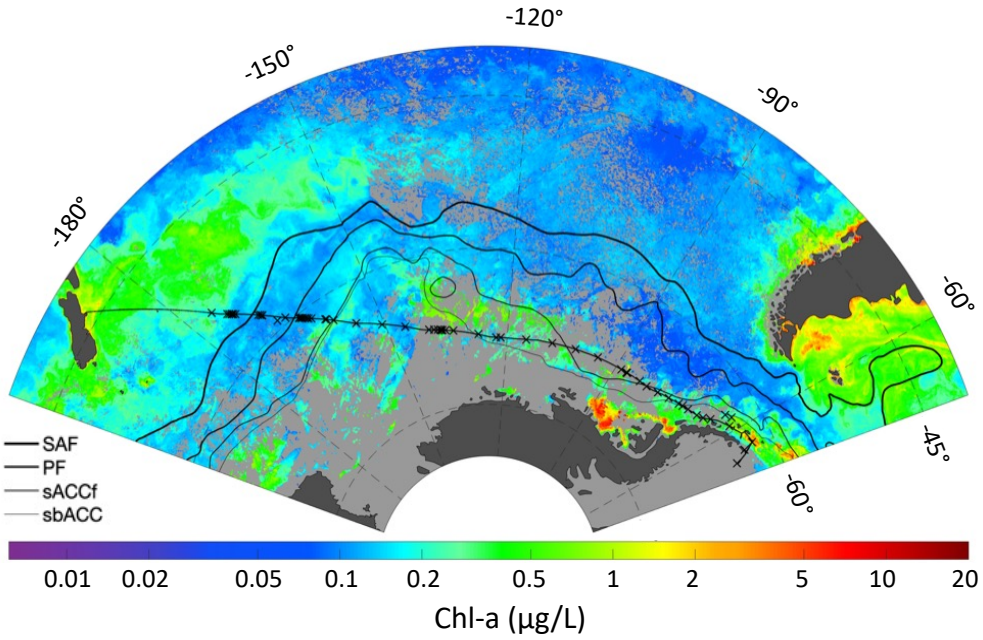

Figure 3.1. ANA08D 2018 expedition cruise track (thin black line linking New Zealand to the Antarctic Peninsula), sampling locations (x), and climatological front locations defined by Orsi et al, 1995 (SAF, Subantarctic front; PF, Polar front; sACCf, Southern Antarctic Circumpolar Current font; sbACC, Southern Boundary of the ACC) overlaid on a MODIS chlorophyll-a composite for March 2018.

HPLC analysis of pigments

Phytoplankton from 0.5 to 2 L of seawater were filtered onto Whatman GF/F glass-fiber filters (25 mm diameter) using a vacuum pressure of less than 0.5 atm. All samples were frozen on liquid nitrogen prior to shipment and extraction. Chlorophylls and carotenoids were extracted in 2 ml of 90% acetone, sonicated on ice (35 s), left to extract for 24 hours at 4 °C, and filtered through Whatman Puradisc Polypropylene Syringe Filters (0.45 µm) prior to analysis. Extracted samples were run on an Agilent 1260 Infinity II LC system, with a chilled autosampler and a diode array detector operated at 450 nm, with a reverse-phase C18 column following the protocol of Zapata et al. (2000). Detected peaks were compared to known standards based on

retention time and UV-visible spectra. Pigment standards were obtained from DHI, Denmark, with the exception of chlorophyll-a (chl-a) and chlorophyll-b, which were obtained from Sigma-Aldrich.

HPLC analysis of Mycosporine-like Amino Acids

Phytoplankton from 0.5 to 2 L of seawater were filtered onto Whatman GF/F glass-fiber filters (25 mm diameter) using a vacuum pressure of less than 0.5 atm. All samples were frozen on liquid nitrogen prior to shipment and extraction. MAAs were extracted and analyzed according to the HPLC method of Carreto et al. (2005). In brief, each sample was extracted sequentially (x3) in 2ml of 80% methanol and sonicated on ice (30 s total, 10 s on, 5 s off). Extracts were centrifuged and pooled to remove filter debris, and the supernatant was evaporated using a Labconco Centrivap Concentrator at 30 °C. Samples were resuspended in 0.5 ml of HPLC grade H_2O and filtered through a Pall Nanosep 100k Omega centrifugal filters prior to analysis. Samples were analyzed using the reverse C18 columns and the gradient elution described in Carreto et al., 2005. MAA identities were confirmed for dominant MAAs using retention times, UV-visible spectra, and LC-MS analysis. MAAs were quantified using response factors (ng/HPLC peak area) from MAAs isolated and verified by LC-MS from cultures using published extinction coefficients. For MAAs unavailable from phytoplankton cultures, HPLC eluate from similar field samples were captured and pooled and analyzed by LC-MS. The HPLC eluate was electrospray ionized (35eV) and analyzed for positive ions using a Thermo-Finnigan LCQ Advantage ion trap mass spectrometer, fitted with an Ion-Max ESI source and run with a scanning range of 50–500 *m/z*. LC-MS column and solvent conditions were identical to HPLC analysis with the exception that the LC-MS column was not temperature controlled.

CHEMical TAXonomy (CHEMTAX) analysis

Phytoplankton community composition was determined by using the CHEMical TAXonomy (CHEMTAX) software (Mackey et al., 1996), a program that uses factor analysis and steepest descent algorithm to determine the best fit to the data with a given input matrix of pigment ratios. Using an iterative process for a given input matrix, the software optimizes the pigment ratios for each group and applies the final ratio to the total chl-a in each sample to determine the proportion of total chl-a attributed to each phytoplankton group in the community. For this study, the Microsoft Excel based CHEMTAX 1.95 with ChemtaxHelper V7.1 was used.

The initial pigment ratios used for the CHEMTAX program (Table 3.1A) were adopted from Wright et al., 1996. These ratios were chosen as they have been optimized to represent the taxonomic groups found across fronts in the Southern Ocean from -45 to -65 °S, a latitudinal gradient encompassing this study. Following the recommendation of established methods (Latasa, 2007), six sets of ten CHEMTAX runs each were made from the dataset, with the first runs using the initial ratios found in Table 3.1A and up to a 75% random error added to the initial ratio values. Each subsequent run applied the output ratio of the previous run as its initial ratio, and the outputs calculated from the tenth runs were considered final. All samples were run together as opposed to separate bins, justified by collection from identical depths and limited samples size. Phytoplankton community data in this study are presented as relative abundance, which is calculated as each discrete sample's taxon-specific chl-a normalized by that sample's total chl-a concentration.

Table 3.1A. Initial CHEMTAX pigment ratios

	PER	BUT	FUCO	HEX	NEO	PRAS	VIOL	ALLO	LUT	ZEA	CHLB	CHLA
Dinoflagellates	0	0	0	0	0.15130	0.16076	0.09929	0	0.00946	0	0.94563	1
Cryptophytes	1.06186	0	0	0	0	0	0	0	0	0	0	1
Cryptophytes	0	0	0	0	0	0	0	.22850	0	0	0	1
Haptophytes-N	0	0.02548	0.09979	1	0	0	0	0	0	0	0	1
Haptophytes-S	0	0.04492	0.40430	0.50586	0	0	0	0	0	0	0	1
Chlorophytes	0	0	0	0	0.06369	0	0.05414	0	0.20223	0.00955	0.26274	1
Cyanobacteria	0	0	0	0	0	0	0	0	0	0.34771	0	1
Diatoms	0	0	0.6	0	0	0	0	0	0	0	0	1

Table 3.1B. Final CHEMTAX pigment ratios.

	PER	BUT	FUCO	HEX	NEO	PRAS	VIOL	ALLO	LUT	ZEA	CHLB	CHLA
Dinoflagellates	0	0	0	0	0.13435	0.13460	0.09189	0	0.00958	0	1.07624	1
Cryptophytes	1.11474	0	0	0	0	0	0	0	0	0	0	1
Cryptophytes	0	0	0	0	0	0	0	0.28313	0	0	0	1
Haptophytes-N	0	0.03260	0.10170	1.24446	0	0	0	0	0	0	0	1
Haptophytes-S	0	0.31029	0.23862	0.56928	0	0	0	0	0	0	0	1
Chlorophytes	0	0	0	0	0.06572	0	0.05983	0	0.17598	0.01075	0.25072	1
Cyanobacteria	0	0	0	0	0	0	0	0	0	0.31681	0	1
Diatoms	0	0	0.75032	0	0	0	0	0	0	0	0	1

UVR Dosage Modelling

The UVR dosages at 305, 325, 340, and 380 nm were modeled for our discrete sampling sites using the methods of Smyth (2011), with updates to the sources of cloud data and the absorption at 443 nm as follows. Data were determined using the LibRadTran model (v1.4) using ozone, cloud-cover (extracted from the ECMWF ERA5 dataset) and Aerosol Optical Thickness as ancillary datasets, from which daily fields at ~1 ° resolution were calculated for 2018. Monthly composites were created, and total absorption at 443 nm (determined using Lee et al. 2005 QAA model) was used to determine the diffuse attenuation coefficient at 305, 325, 340 and 380 nm from empirical data (see Smyth (2011)). Using the mixed layer depth climatology of de Boyer Montégut et al. (2004), mixed layer depth integrated dosages were calculated. See Smyth 2011 for full details.

Nutrients

At selected stations, samples for analysis of dissolved nutrients (silicate, nitrate, nitrite, phosphate, and ammonia) were collected from the ship's clean flow-through system. Samples

were filtered (0.45 um) into 20 ml HDPE scintillation vials previously cleaned in the laboratory with 10% HCl. Samples were immediately frozen at -20 C and shipped to the University of Washington, where they were analyzed within 30 days of the end of the cruise at the Marine Chemistry Laboratory in the University of Washington's School of Oceanography. Samples were analyzed using segmented flow analysis following standard protocols using a Seal Analytical AA3 (Hood et al, 2010).

Results

Hydrographic features

The location of the Subantarctic (SAF) and Polar (PF) fronts were characterized based on continuous temperature and salinity observations alongside discrete nutrient measurements. The SAF was identified from 171 to 169.5 °W, by a drop in temperature from ~9.6 °C to 6.5 °C. The PF was identified from 165.5 to 161 °W by a decrease in a temperature and an increase in silicic acid concentration from 4.02 to 19.39 uM. The Southern Antarctic Circumpolar Current font (sACCf) and Southern Boundary of the Antarctic Circumpolar Current (sbACC) climatological fronts (Orsi et al., 1995) have been overlaid on the transect map in **Figure 3.2**, however they were not directly identified in the hydrographic data as their definitions rely on subsurface data.

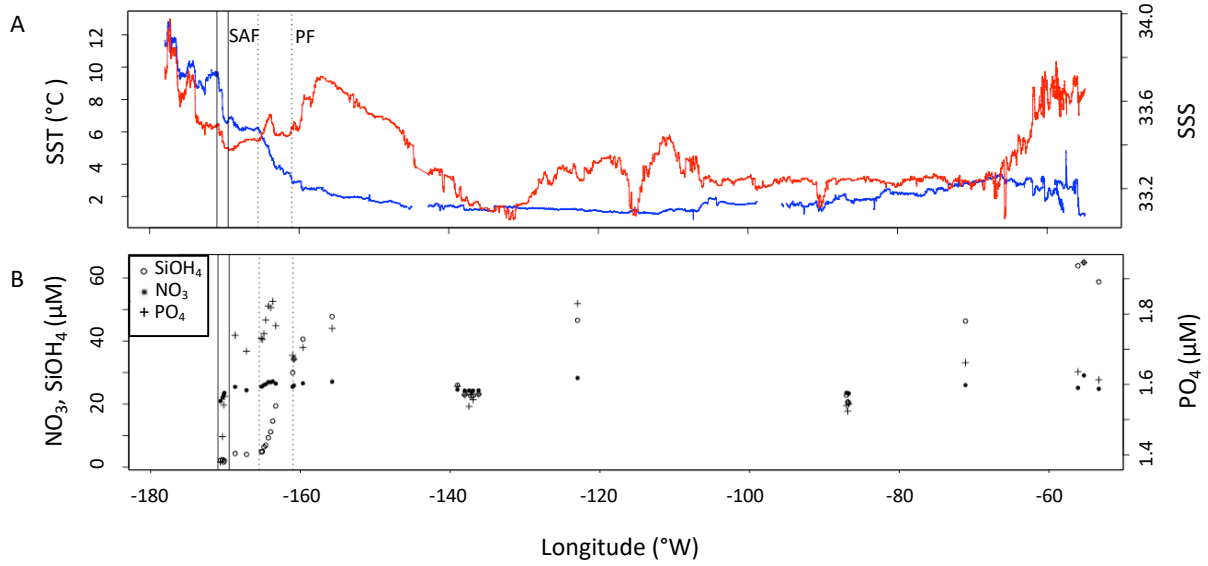

Figure 3.2. A) Sea surface temperature (SST, blue) and salinity (SSS, red) measured underway across the transect. Ranges of the Subantarctic front (SAF) and Polar front (PF) indicated by solid and dotted vertical bars, respectively. B) Surface nutrient concentrations (NO_3, $SiOH_4$, and PO_4) measured along the transect.

Pigments

Concentrations of chl-a measured west of 100 °W were relatively low, ranging from 0.05 to 0.43 µg/L (**Figure 3.3**). The highest levels of chl-a (up to 1.57 ug/L) were found at the eastern end of the transect, near the coast of the WAP. Concurrently, the maximum values for the majority of the other pigments analyzed occurred in the WAP coastal region as well, with the exception of 19'-hexanoyloxyfucoxanthin and zeaxanthin which had maximum values near the north-western end of the transect. Fucoxanthin, the major carotenoid in diatoms had the highest concentration near the eastern end of the transect, correlating strongly with chl-a ($R^2 = 0.91$). However, fucoxanthin is not an unambiguous marker for diatoms, as the pigment is shared with haptophytes. Conversely, 19'-hexanoyloxyfucoxanthin, a pigment found in some haptophytes and chrysophytes, had highest concentrations at the western end of the transect.

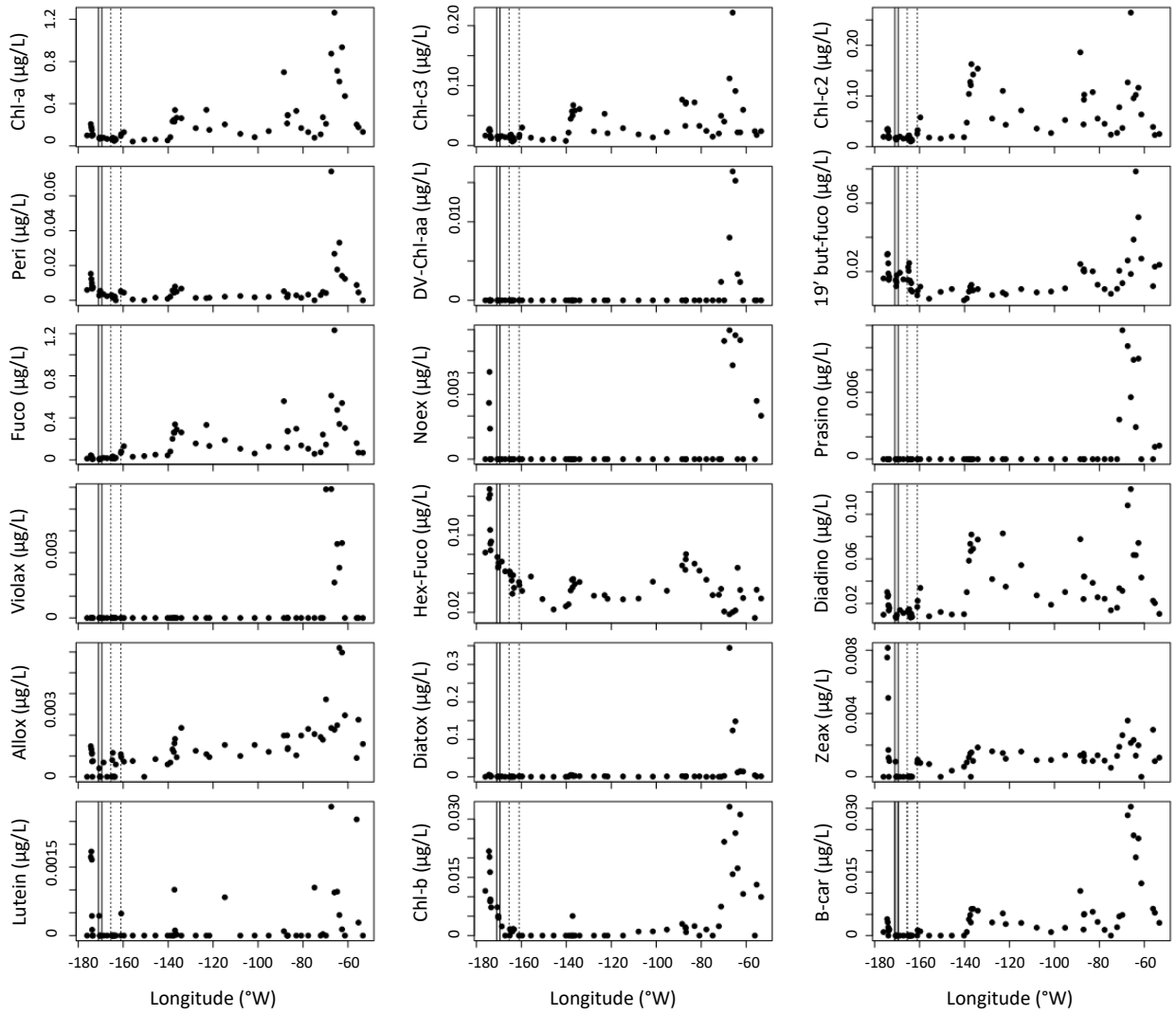

Figure 3.3. Concentration of all pigments (µg/L) analyzed by HPLC along the transect plotted with respect to longitude. The boundaries of the SAF and PF are indicated by solid and dotted vertical lines, respectively.

CHEMTAX analysis

The contribution of various phytoplankton taxa to total chl-a is illustrated in **Figure 3.4**. Diatoms, relatively absent northwest of 140 °W, increased towards the east with maximal values near the Antarctic Peninsula. Dinoflagellates, cryptophytes, and haptopytes-S had maximal contributions to chl-a in this region as well. The highest contribution of Haptophytes-N to total

chl-a were at the northwest end of the transect, decreasing towards the east. Cyanobacteria had peak levels in the north-westerly region as well. Prasinophytes, which were largely absent throughout the middle of the transect, make a small contribution of chl-a near the northwest end of the transect, and around the Antarctic Peninsula.

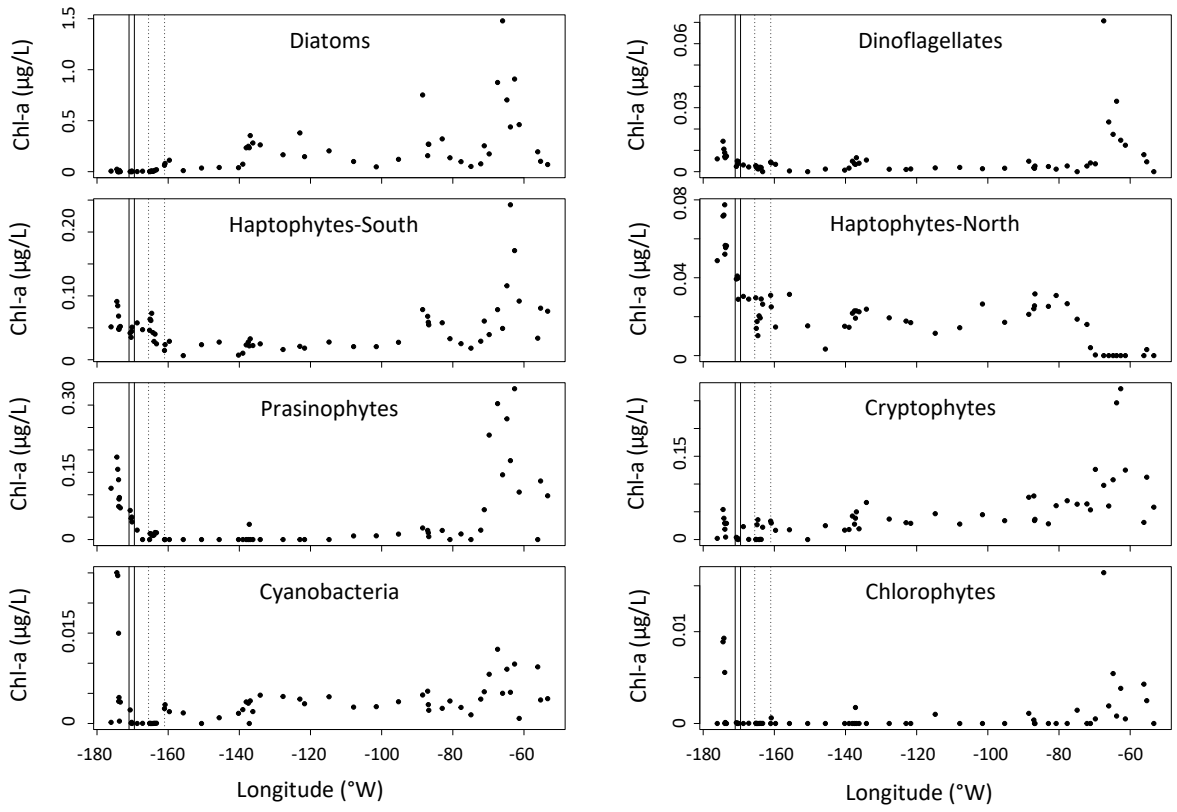

Figure 3.4. CHEMTAX estimates of phytoplankton pigment groups to total chl-a concentrations (µg/L) during the ANA08D 2018 research expedition. The boundaries of the SAF and PF are indicated by solid and dotted vertical lines, respectively.

The percent contribution of each taxonomic group to total biomass, by proxy of chl-a, is illustrated in **Figure 3.5**. The dominant taxa west of 160 °W were the haptophytes, while diatoms constituted the largest percent of biomass around and east of 160 °W. All other taxonomic groups constituted less than 12% of chl-a across the entire transect.

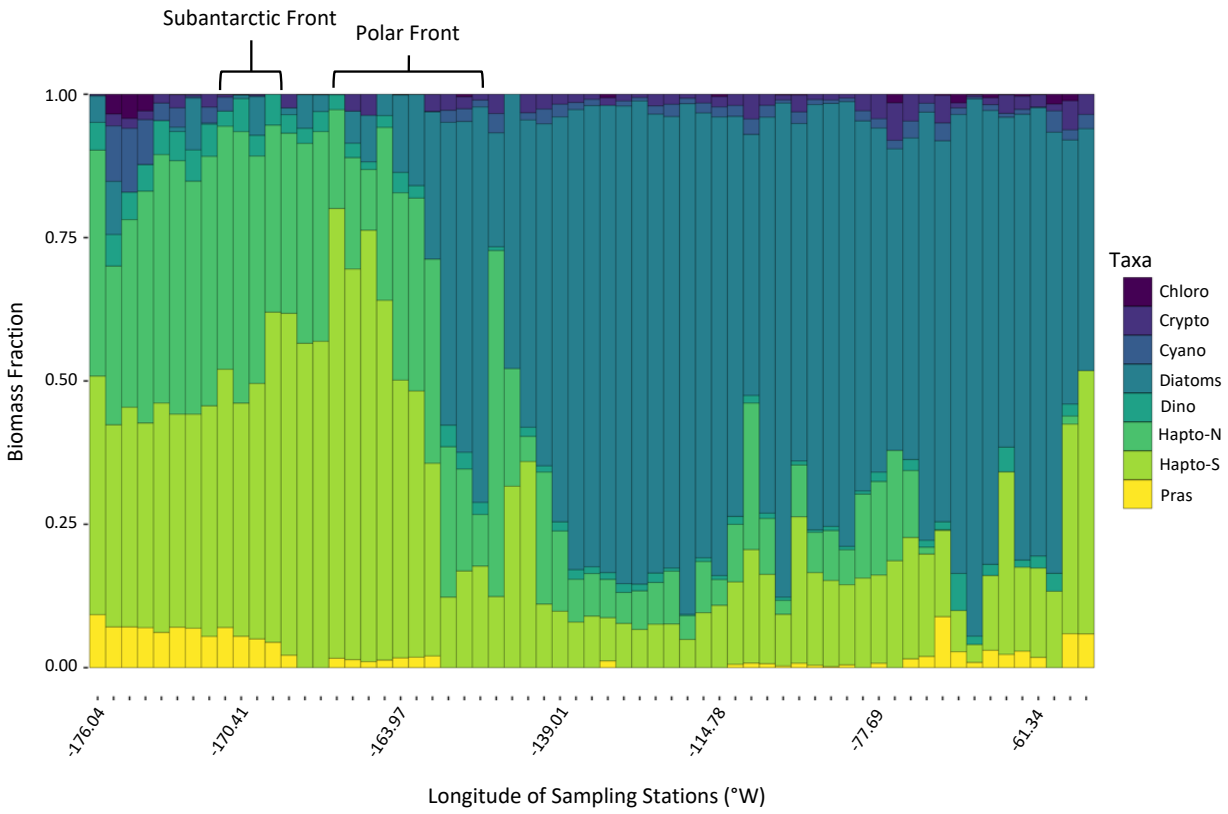

Figure 3.5. Estimated percentage of biomass of each taxonomic group to total biomass during the ANA08D 2018 research expedition.

Mycosporine-like Amino Acids

HPLC analysis revealed 6 dominant MAAs in this region: porphyra-334, shinorine, palythine, mycosporine-glycine, palythenic-acid, and one MAA that could not be identified using secondary standards (**Figure 3.6**). The unidentified MAA is referred to in this study as "Unknown". The MAA described as palythenic-acid was identified by an expected mass of 329 m/z but was not confirmed with a secondary standard. Small quantities of other MAAs including palythene were detected, however they are not included in this study as the 6 dominant MAAs accounted for more than 95% of the total peak area in all samples analyzed, with the exception of one (81% peak area; 55.55 °S, 173.90 °W).

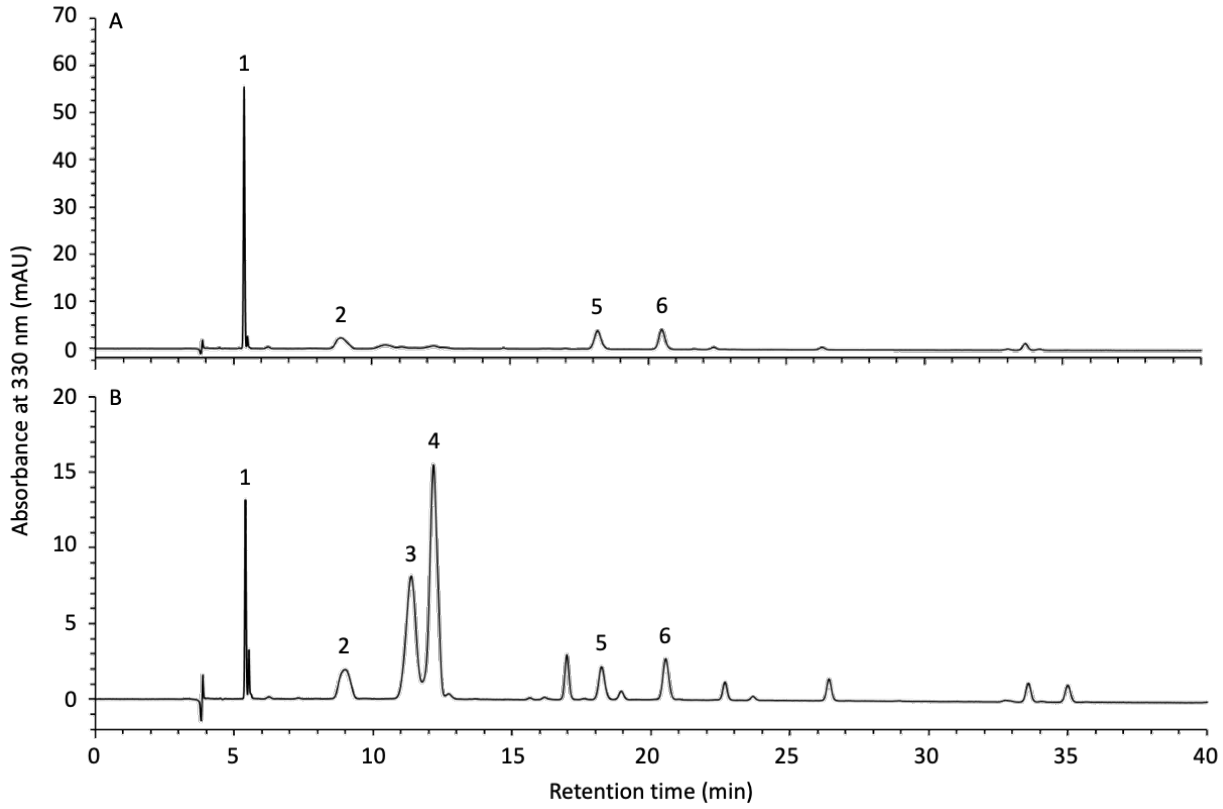

Figure 3.6. Representative HPLC chromatograms of MAA samples from extracts. A) North of the PF, latitude -55.38 °S, longitude -174.16°W, and B) South of the PF, latitude -67.72 °S, longitude -134.12 °W. MAAs identified in the chromatogram were 1) shinorine, λ_{max} 332, retention time 5.4 min; 2) palythine λ_{max} 319 nm, retention time 8.8 min; 3) porphyra-334 λ_{max} 332 nm, retention time 10.5 min; 4) mycosporine-glycine, λ_{max} 309 nm, retention time 12.2 min; 5) Unknown MAA, λ_{max} 334 nm, retention time 18.1 min; 6) palythenic-acid, λ_{max} 336 nm, retention time 20.5 min.

MAAs were ubiquitous in all samples analyzed throughout the transect (**Figure 3.7A**). The sum of the concentrations of the six dominant MAAs varied by a factor of 200. The highest concentration of MAAs detected was 0.58 μg/L at 55.52 °S, 173.94 °W, north of the SAF, followed by a cluster of increasing concentrations from 67.35 °S, 138.06 °W to 67.72 °S, 134.12 °W (**Figure 3.7A**). MAA concentrations normalized to chl-a (MAA:chl-a) decreased from the northwestern end of the transect region to 140 °W, and a local maximum of MAA:chl-a was observed from 139.01 °W to 134.12 °W (**Figure 3.7B**). This cluster coincided with an abrupt

drop in temperature of ~0.5C relative to surrounding samples. The lowest values of MAA:chl-a, ~0.01 µg/L, were observed at the end of the transect in coastal waters near the Antarctic peninsula.

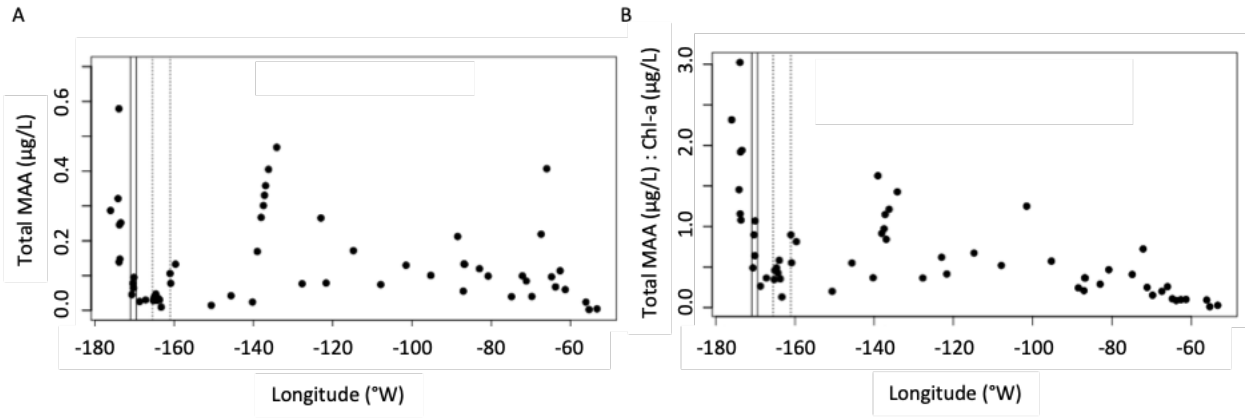

Figure 3.7. Quantitative distribution of the sum of MAAs. A) Sum of all MAAs (µg/L) across the transect of the ANA08D 2018 research expedition. B) Ratio of sum of all MAAs (µg/L) to chl-a (µg/L) across the transect of the ANA08D 2018 research expedition. The boundaries of the SAF and PF are indicated by solid and dotted vertical lines, respectively.

Porphyra-334 was the most abundant MAA across the transect, with maximum concentrations of > 0.30 ug/L from 139.0104 °W to 134.1218 °W coinciding with a local MAA:chl-a maximum, and near the coastal region of the WAP at 65.2106 °S, 66.01364 °W. All other MAAs had relatively similar patterns to one another with maximum values in the northern stations, west of 170 °W, however mycosporine-glycine had relatively high concentrations at sporadic sites throughout the transect.

The MAAs northwest of the PF were composed of a relatively even and diverse mixture of MAAs, with shinorine contributing 30.0% ± 4.7 of the total MAA pool, followed by palythine contributing 17.2% ± 12.1. Southeast of the PF, porphyra-334 accounted for over 50% of the MAA pool in the majority of samples, with values up to 84.3% (**Figure 3.8**).

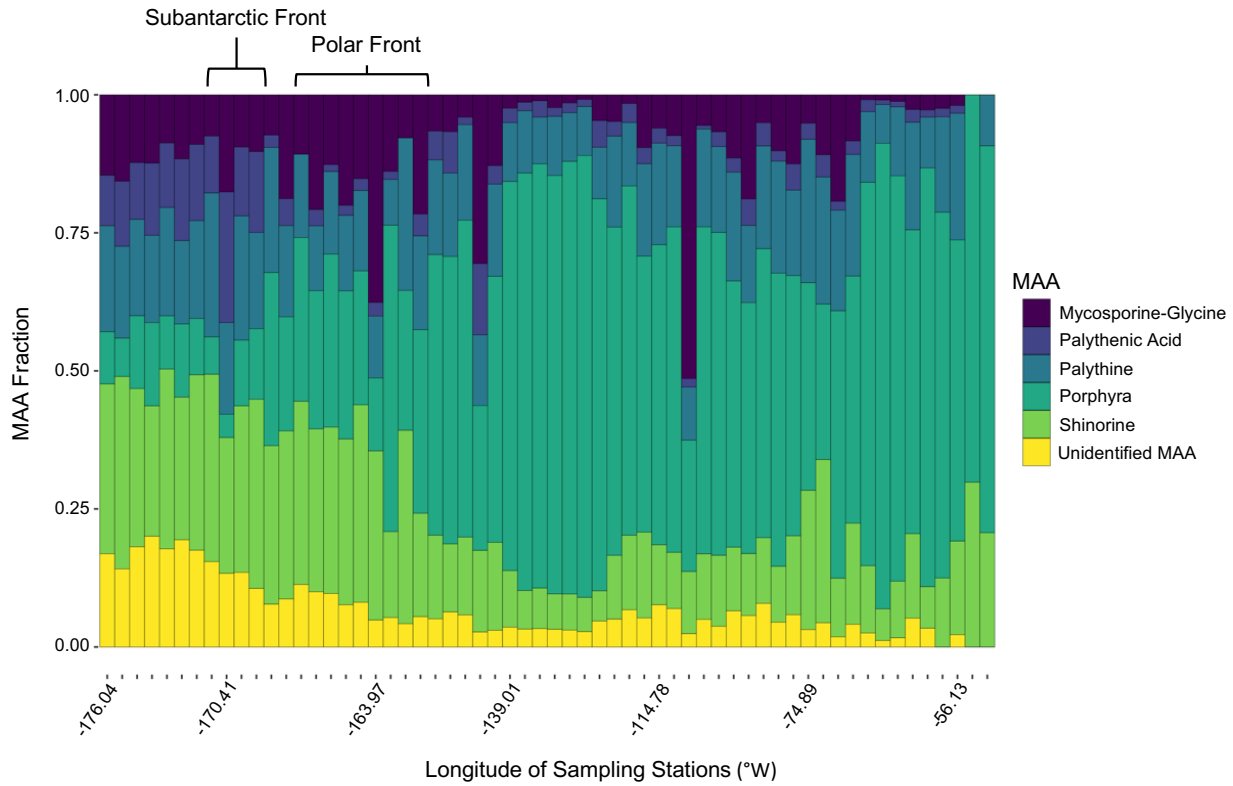

Figure 3.8. Fractional contribution of each dominant MAA to the total MAA pool during the ANA08D 2018 research expedition.

A strong positive correlation was found between the diatom fraction of phytoplankton biomass and the porphyra-334 fraction of the MAA pool ($R^2 = 0.744$, $P < 0.0001$, **Figure 3.9**). All other MAAs were inversely related to the diatom fraction, shinorine being the strongest inverse correlation ($R^2 = 0.797$, $P < 0.0001$). Haptophytes-S were most strongly correlated with the shinorine fraction of the MAA pool ($R^2 = 0.657$, $P < 0.0001$), whereas haptophytes-N were most strongly correlated with palythenic-acid fraction ($R^2 = 0.647$, $P < 0.0001$). Dinoflagellates and prasinophytes were most strongly correlated with the palythenic-acid fraction of the MAA pool as well ($R^2 = 0.4447$, $P < 0.0001$ and $R^2 = 0.3634$ $P < 0.0001$, respectively). Chlorophytes, cryptophytes, and cyanobacteria were not significantly correlated with any MAAs in this study.

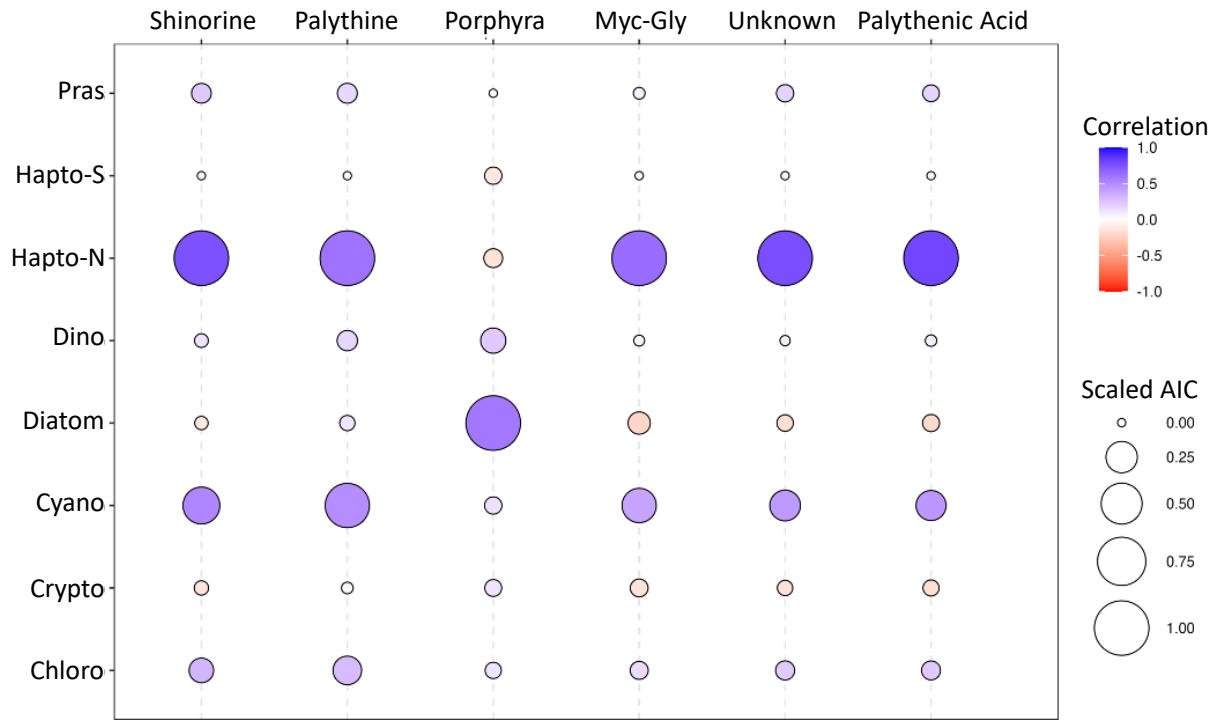

Figure 3.9. Pearson correlation coefficient and scaled Akaike information criterion (AIC) between taxonomic and MAA fractions.

Modeled UVR dosages

Monthly UVR doses experienced in the sampling region were modeled for January, February, March, and April 2018 (**Figure 3.10A**). Satellite data required for modeling was largely irretrievable across the transect in April due to cloud cover and was subsequently excluded from analysis. The strongest UVR doses in the mixed layer were estimated at the highest latitudes, at the western end of the transect. An overall monthly decrease in UVR dosage was observed from February through April due both to seasonal transition and variations in mixed layer depth The strongest, albeit weak correlation between total MAAs and UVR was with UVB (305 nm) in February ($R^2 = 0.28$). When total MAAs were normalized to chl-a, UVR dosages in both the UVA and UVB were found to be strongly correlated (**Figure 3.10B**).

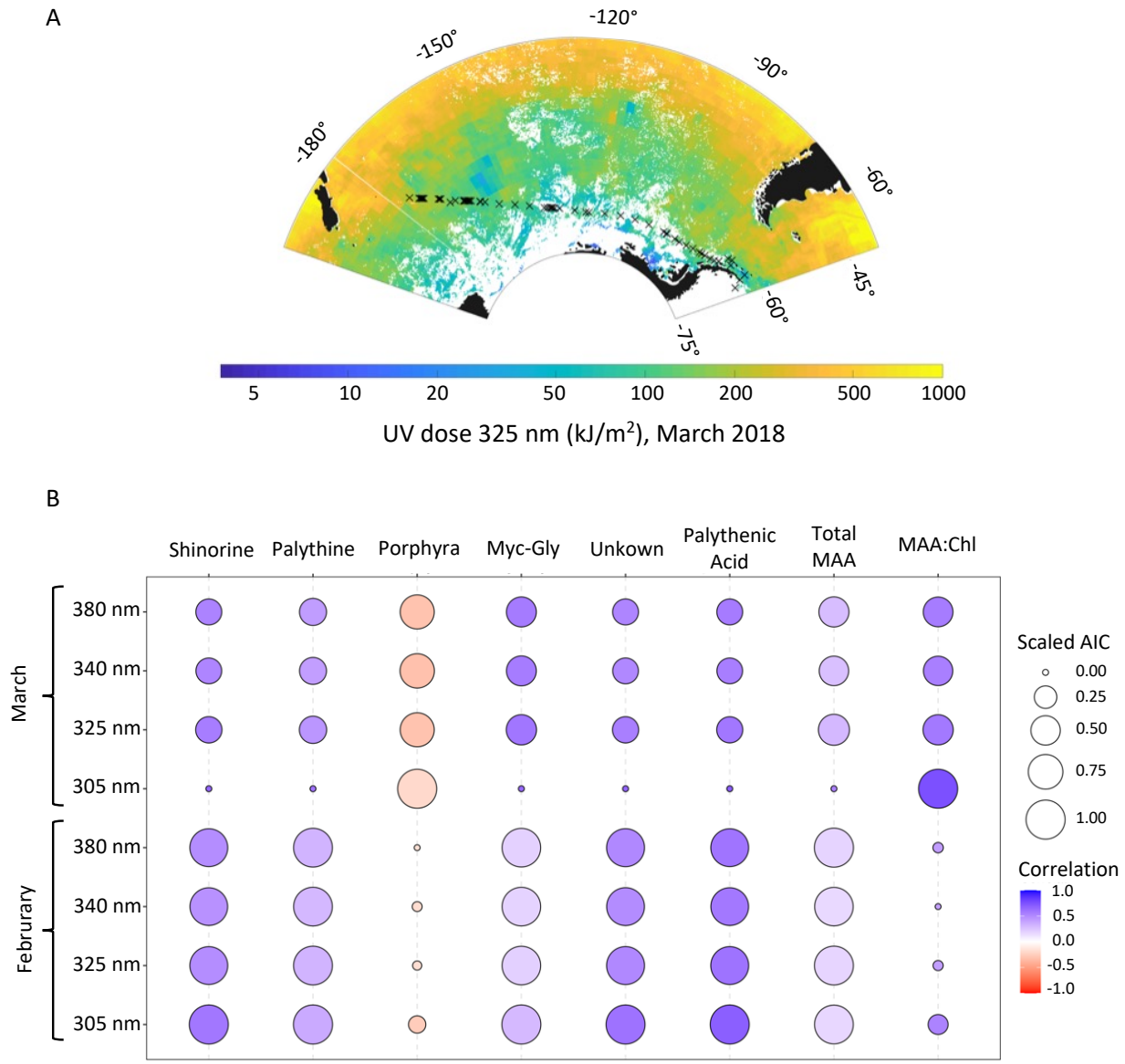

Figure 3.10. Modeled UVR dosages and correlation to MAAs. A) Modeled UVR dosage at 325 nm for March 2018 overlaid on cruise transect map. B) Pearson correlation coefficient and scaled Akaike information criterion (AIC) between UVR dosage at 305, 325, 340, and 380 nm in February and March 2018, and MAA fractions, total MAAs, and MAA:chl-a.

Discussion

This study highlights the ubiquity of mycosporine-like amino acids across the Southern Ocean in a transect from New Zealand to the Antarctic Peninsula in 2018. This is the first report of the distribution of MAAs across the major Southern Ocean fronts and provides further

evidence for the widespread global presence of MAAs suggested by Llewellyn et al. (2012). A linear correlation between the mean daily UVR dosage for the month preceding sampling and MAA:Chl-a highlight the importance of light history. It has been shown that previous light history plays an important role in development of UVR screening molecules in photosynthetic organisms (Carreto et al., 1989). Llewellyn et al. (2012) found a significant linear correlation between MAA:Chl-a and the mean UVR dose in the mixed layer for the month preceding sampling across the Atlantic Ocean, but not during the month of sampling. Unfortunately, due to limited satellite retrievals in our region during April we were unable to obtain UVR doses in the mixed layer for the majority of our sampling sites. However, the significant linear correlation between MAA:Chl-a and the mean daily UVR doses calculated for March suggests the results presented by Llewellyn et al. (2012) are consistent for the Southern Ocean as well. While along-track measurements of UVR were obtained, variability in the time of day of sampling and changes in cloud cover rendered comparisons of MAA composition to acute UVR exposure impractical. It should be noted that strong correlations were found between SST and MAA:Chl-a concentrations as well as modeled UVR dosage (**Supplementary Figure 3.1**). However, SST and UVR were strongly correlated across our transect, as is typical for the marine sea surface (Beckmann et al., 2014).

This study also highlights the relationship between phytoplankton taxa and MAAs present in the water column. A distinct transition in phytoplankton taxa was observed across the PF in our transect from haptophytes north of the PF to diatoms south of the PF. The highest levels of MAAs relative to chl-a were present north of the PF, associated with the haptophyte population. While culture isolates of haptophytes have previously been shown to express high levels of MAAs (Jeffrey et al., 1999), this region of the transect was also subjected to the highest

modeled levels of daily mean UVR in the month preceding sampling, making it difficult to separate the influence of taxonomy and UVR on MAA:chl-a. A lack of correlation with chlorophytes, cryptophytes, and cyanobacteria to any specific MAA may be due to the low biomass of these taxa present in samples, as chlorophytes, cryptophytes and cyanobacteria in other regions have been shown to possess MAAs (Llewellyn and Airs, 2010; Rastogi and Incharoensakdi, 2013).

The transition to the diatom dominated waters south of the PF coincided with a transition to porphyra-334 as the dominate MAA present in the MAA pool. Previous studies of pure cultures including *Thalassiosira sp*., *Fragilariopsis cylindrus,* and *Corethron criophilum* have identified the presence of porphyra-334 and shinorine as the primary MAAs of Antarctic diatoms (Helbling et al., 1996; Riegger and Robinson, 1997; Hernando et al., 2002). A study conducted in the Sub-Antarctic Zone of Tasmania in 2007 also documented a predominance of porphyra-334 as the dominant MAA in the PF zone, which highlights a consistency in MAA composition in the PF zone across a decade timescale (Oubelkheir et al., 2013) and along the zonal structuring of the frontal zones of the ACC. Additionally, frustules from sediment cores sampled near this transect (NBP9604 St3 MC8, 61°57′S, 170°03′W) found MAAs in diatom frustules, with the dominant MAA being Porphyra-334, corroborating the dominance of this MAA in diatom populations south of the polar front (Ingalls et al., 2010).

Diatoms have been used as a diagnostic for the location of the PF due to their dependance on dissolved silica for their siliceous frustules (Barron, 1996; Cortese and Gersonde, 2008). Given the relationship between diatoms, porphyra-334, and silica present at the polar front, porphyra-334 may serve as an alternate proxy for the location of the PF zone. Kahru et al., 2021 demonstrated the ability to differentiate neighboring algal blooms of differing taxonomic

composition via the remote detection of UVR spectral bands, likely due to the presence of MAAs. However, this differentiation was hypothesized to be based on the presence of the MAA palythene, which has a peak absorption at 360 nm in the long-wavelength UVA region. Given the similarity in absorption spectra between porphyra-334 and the MAAs associated with the haptophyte population north of the PF, distinguishing between the two will likely prove difficult. Furthermore, the challenge to use future satellites to retrieve signals below 350 nm may prove insurmountable due to the strong increase in Rayleigh scattering by the atmosphere at shorter wavelengths. However future studies in tandem with a complete suite of optical measurements are warranted and certainly could be applied on in situ gliders, moorings and profilers.

Here the profile of MAAs in phytoplankton in a transect from Eastern New Zealand to the WAP has been documented for April 2018, however future work should be conducted to document seasonal changes in MAA composition. Presumably, lower levels of irradiance during the Winter season will result in a reduction of MAA:Chl-a, and seasonal variations in phytoplankton taxa composition will result in changes in MAA quantity and quality. As climate change effects range expansion and contraction of varying phytoplankton taxa, baseline measurements will be necessary in order to separate seasonal variability in MAA quantity and composition from anomalies. Notably, blooms of phytoplankton containing MAAs with spectral signatures within the detection range of satellite sensors, such as dinoflagellates, may be detectable in the Southern Ocean by means of remote sensing with improved algorithms extended into the ultraviolet. Additionally, future studies incorporating metagenomics and metatranscriptomics in tandem with MAA analysis will allow for a higher resolution of phytoplankton groups, their correlation with specific MAAs beyond the taxa identified in this study, and an enhanced understanding of their utility as bio-indicator of UVR induced stress.

Conclusion

Amidst climate change and subsequent variations in interactions between phytoplankton and abiotic factors such as UVR, it is important to establish baseline patterns for MAA expression in the world's oceans. With the advent of new hyperspectral remote sensing platforms, a baseline understanding of the global distribution of MAAs will likely enhance capabilities to observe changes in the distribution of MAAs and MAA:Chl-a as a proxy for the photoprotective response of phytoplankton. Additionally, an enhanced understanding of the distribution and utility of MAAs to serve as a bio-indicator of UVR-induced stress in phytoplankton may help to improve models that incorporate spectral light and explicit radiative transfer to examine the role of the irradiance spectrum and pigments in establishing biogeography. The results presented here demonstrate a correlation between the preceding month's mean daily UVR dosage and MAA:Chl-a, as previously described for the Atlantic Ocean, as well as a shift to a predominance of the MAA porphyra-334 south of the PF, concurrent with a dominant diatom population.

Supplementary Figures

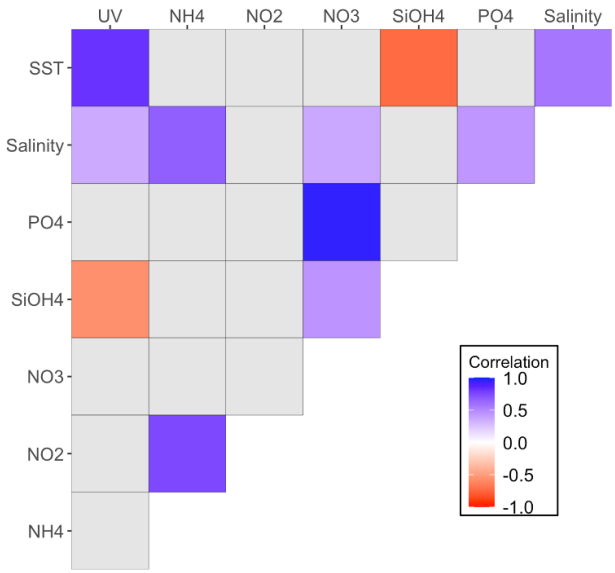

Supplementary Figure 3.1. Pearson correlation coefficients between abiotic factors.

Acknowledgments

We would like to thank the Araon crew and captain for their assistance and logistical support. We would also like to thank Michael Lesser and Kai Bishoff for isolating and providing MAA secondary standards. This research was conducted as a part of the project "Carbon cycle change and ecosystem response under the Southern Ocean warming" (PE22110) and supported by the Korea Polar Research Institute (KOPRI), Incheon. ELW was funded by the National Science Foundation through GRFP DGE-1650112 and MV was supported by the National Science Foundation Office of Polar Programs through award number 1822289.

Chapter 3, in full, is in preparation for submission as Weiss EL, Cape MR, Pan BJ, Smyth TJ, Vernet M, Mitchell BG. The Distribution of Mycosporine-like Amino Acids in Phytoplankton Across a Southern Ocean Transect. The dissertation author was the primary investigator and author of this paper.

CHAPTER 4: Bio-composite Hydrogels with Engineered Cyanobacteria Yield Stimuli-responsive Photosynthetic Materials for Bioremediation

Summary

We demonstrated the potential of integrating cyanobacteria cells within a 3D printed hydrogel matrix, resulting in a photosynthetic biocomposite material that can be bioengineered to produce functional outputs in response to an external chemical stimulus. We demonstrated the advantages of utilizing additive manufacturing techniques to control the design and shape of the fabricated materials, which proved to be important for the support and growth of obligate phototrophic microorganisms within the material. As an initial proof-of-concept, we utilized a synthetic theophylline-responsive riboswitch in *Synechococcus elongatus* PCC 7942 for regulating the expression of a yellow fluorescent protein (YFP) reporter. Our results show that upon induction of a conformational change to the riboswitch with theophylline, the encapsulated cells are able to produce the YFP protein within the matrix. Subsequently, we engineered a strain of *S. elongatus* to produce an oxidative laccase enzyme and to have the capacity for inducible cell death. We demonstrated that our fabricated responsive biomaterial is able to decolorize a textile dye pollutant, indigo carmine, thereby having the potential to serve as a powerful tool in environmental bioremediation. The biocomposite material is capable of following a sacrificial approach, where the biological component could be triggered to self-destruct once it fulfills its requirement to reduce biofouling. Additionally, we used a theophylline-responsive riboswitch to activate the cellular expression of the laccase protein within the biocomposite material. Integrating genetically engineered stimuli-responsive cyanobacteria in patterned volumetric constructs, we present programmable photosynthetic materials, capable of producing functional outputs including, but not limited to, bioremediation.

Introduction

Over the past decade the field of engineered living materials (ELMs) has evolved from a fringe endeavor to a discipline in its own right. ELMs are defined by the inclusion of a living component, such as a microorganism, in a polymeric matrix or material. A wide variety of organisms have been utilized in ELMs including bacteria, yeast, fungi and algae for different purposes. Some notable works include the fabrication of skin patches for wound healing (González et al., 2020), sweat-responsive biohybrid fabrics (Wang et al., 2017), a biodegradable aquaplastic (Duraj-Thatte et al., 2021), the incorporation of chloroplasts for self-repairing hydrogels (Kwak et al., 2018), and photosynthetic O_2 generators for enhancing mammalian cell viability (Maharjan et al., 2021). One advantage of ELMs over traditional materials is that the biological component of the ELM can be genetically engineered to provide complex responses to environmental stimuli and produce functional biological outputs. Thus, the most attractive types of organisms to include in ELMs are species for which either the wild-type strain has a functional output of interest, or a wide range of synthetic tools is available for the genetic modification of the organism.

Cyanobacteria are appealing candidates for inclusion in ELMs because the carbon source for phototrophs is innately free and provides the environmental benefit of carbon sequestration, the cells are viable in low-cost media, and there is an abundance of biosynthetic toolkits available for several cyanobacterial species. A number of ELMs have been designed using cyanobacteria as the biological component of the construct (Sawa et al., 2017; Joshi et al., 2018; Chen et al., 2020); however, to date none of these materials has capitalized on the potential for genetic modifications in cyanobacteria that can result in customizable functional outputs and

regulatory systems in the ELMs. Over the last decade the toolkits available for genetic modification in cyanobacteria have rapidly developed, and there have been a number of applications of these tools towards heterologous expression of high-value products and regulatory circuits (Ducat et al., 2011; Oliver et al., 2016; Taton et al., 2017). Notably, the development of various cyanobacteria-compatible promoters, ribosomal binding sites (RBSs), reporters, modular vectors, and markerless selection systems have contributed greatly to the evolution of cyanobacterial synthetic biology (Santos-Merino et al., 2019; Till et al., 2020). Of particular relevance to this study is the development of theophylline-responsive riboswitches in the cyanobacterium *Synechococcus elongatus* PCC 7942, which, when supplemented with the small molecule theophylline, undergo a conformational change allowing the mRNA to bind to an RBS, resulting in the translation of a protein (Ma et al., 2014).

While the past and potential applications of ELMs are vast, the utilization of ELMs in the environmental sector is an attractive prospect (Tay et al., 2017; Mohsin et al., 2021). Bioremediation is one such area where ELMs containing genetically modified organisms may prove fruitful. Previous work has demonstrated that cyanobacteria are capable of producing both native and recombinant enzymes with relevance to bioremediation (Liang et al., 2018; Han et al., 2020; Chakdar et al., 2022). In this study, we utilized genetically engineered strains of the obligate photoautotroph *S. elongatus* PCC 7942 to construct an ELM with properties suitable for the bioremediation of textile dye pollution in aqueous solutions and with the capacity for stimuli-responsive cell death to prevent biological fouling of natural systems.

Results

Material and strain selection

Identifying a biocompatible as well as printable polymer is a critical parameter when encapsulating microorganisms in any 3D-printed scaffold. Initial optimization experiments were conducted to identify a suitable matrix for the encapsulation of cyanobacterial cells that would sustain the growth and viability of the cells at ambient temperatures. Hydrogels are viable matrices for cell-culture experiments because of their capacity for water retention capacity and cell adhesion (Augst et al., 2006; Sarker et al., 2015). Among various formulations we tested of both natural and synthetic polymers capable of forming hydrogels, our best candidate was an alginate hydrogel. Alginate is a natural polysaccharide derived from seaweed that is composed of β-D-mannuronic acid and α-L- guluronic acid (Webber and Shull, 2004). The optimal condition for the alginate to be physically crosslinked using divalent cations and printable at room temperature was a mixture of 4% w/v alginate solution with a 50 mM $CaSO_4$ slurry suspension in a 2:1 ratio. Concentrations of alginate greater than 4% w/v resulted in clogging of the printing nozzles. A crucial step involved in Direct Ink Writing (DIW) is obtaining a material with suitable viscosity such that the printed structure is able to hold its shape post-printing (Li et al., 2019). This property was achieved using a 4% w/v alginate solution and a 15 min incubation of printed hydrogels in a solution of 100 mM $CaCl_2$ to further strengthen and stabilize the gel (**Figure 4.1**) prior to incubation of hydrogels under light in BG-11 medium.

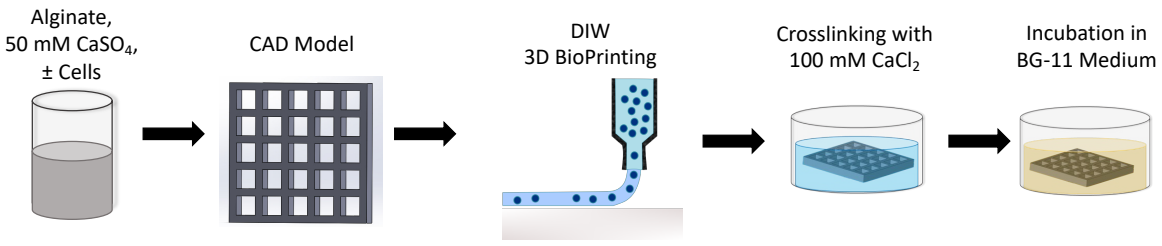

Figure 4.1. Schematic of the DIW workflow.

Mechanical properties of hydrogel

Rheological measurements were carried out to test the mechanical properties of the 3D printed hydrogel with and without embedded cells. We measured both the Storage (G′) and loss moduli (″) with increasing oscillatory strain. As expected, our gels demonstrated a shear-thinning behavior which is a requirement for DIW-based printing (**Figure 4.2A**). The alginate hydrogel and the bioink storage modulus values at lower oscillation strain are of similar magnitude. Additionally, we observed a shift in crossover frequencies between the alginate and the bioink samples (**Figure 4.2A**), with the viscosity of the bioink higher than that of the alginate hydrogel that lacks cells (**Figure 4.2B**).

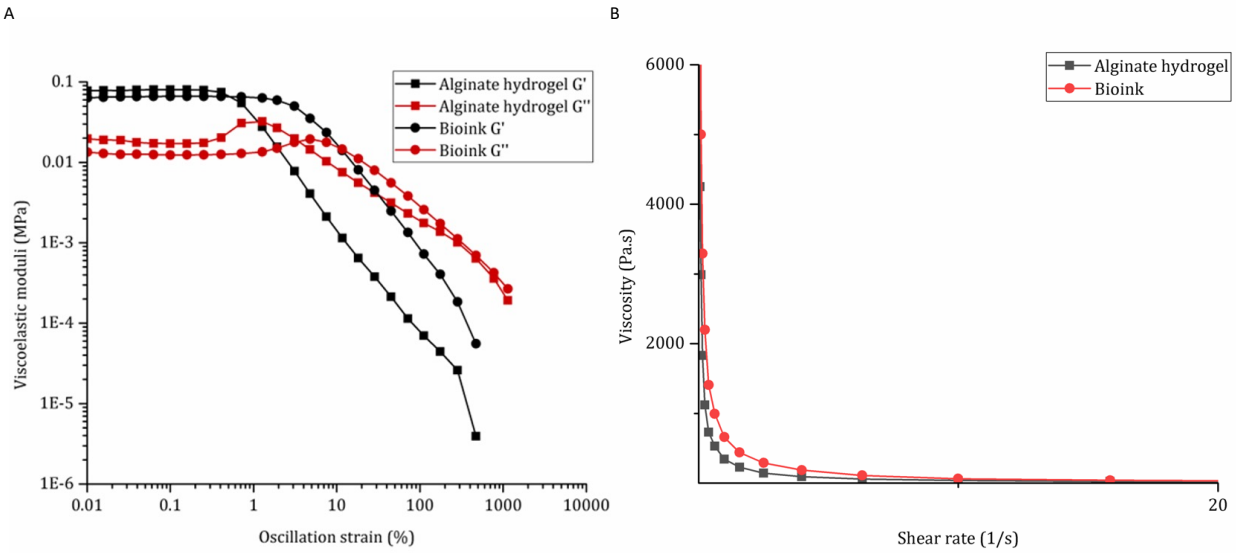

Figure 4.2. Rheological characterization of the blank hydrogel (alginate hydrogel) and hydrogel containing cells (bioink) after five days of incubation. Storage modulus is denoted by G' and loss modulus by G". A) Hydrogel viscoelastic moduli G' and G" at ω = 10 rad/s and 25 °C. B) Viscosity measurements of hydrogels at 25 °C.

Microstructure of hydrogel

Scanning electron microscopy (SEM) images of blank hydrogels illustrate the porous nature of the hydrogel scaffold (**Figure 4.3A and B**), with apparent pore sizes ranging from

under 40 µm to over 60 µm. Images of hydrogels printed with bioink illustrate a combination of individual cells and colonies of cells adhered to the cell surface (**Figure 4.3C and D**).

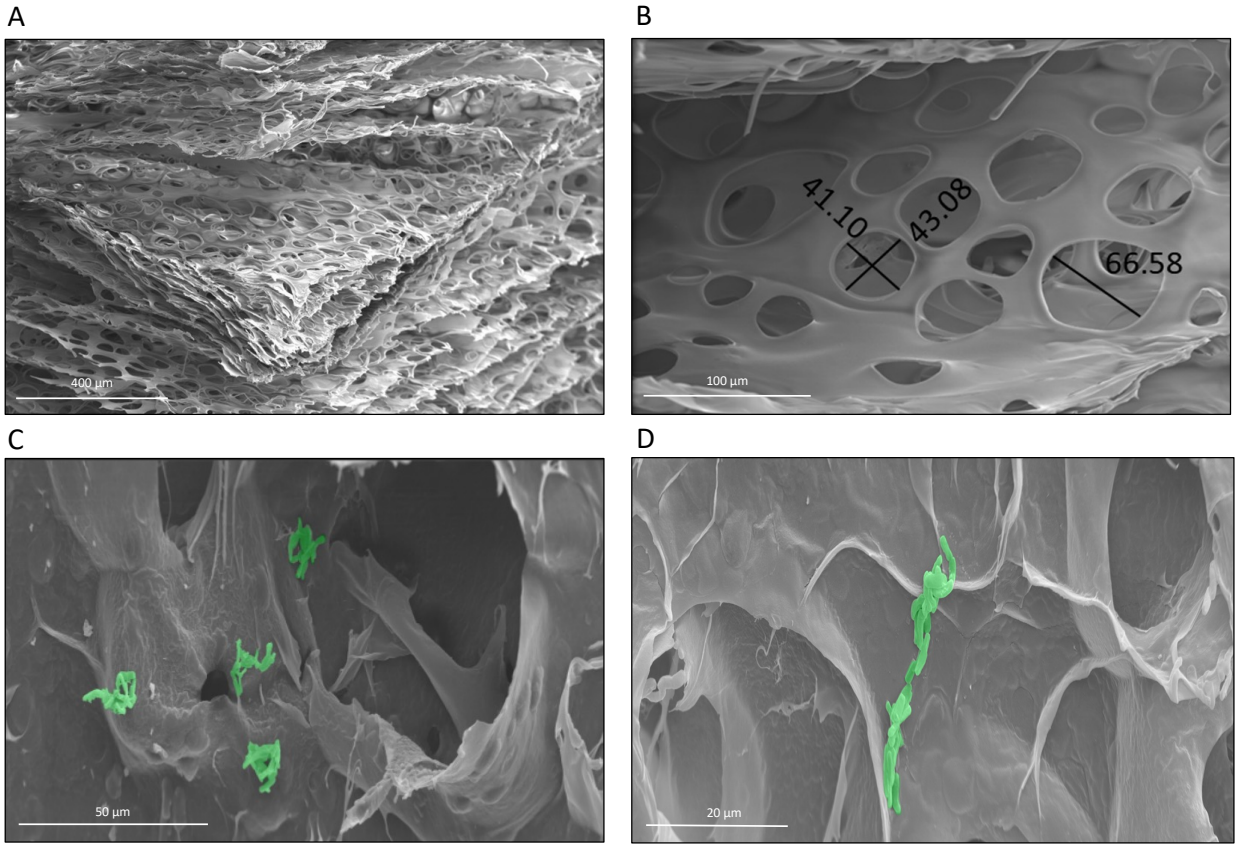

Figure 4.3. SEM images of blank hydrogels (A and B), and hydrogels printed with bioink containing wild-type *S. elongatus* PCC 7942 cells in false color (C and D).

Viability and photosynthetic activity of cyanobacteria in hydrogel

We first assessed whether wild-type *S. elongatus* PCC 7942 (WT) would maintain long-term viability within various hydrogel designs (**Figure 4.4**). Over seven days of growth, biomass within each construct became visually denser; however, designs that had low surface area to volume ratios, such as the disk (2 cm in diameter), resulted in a decrease in biomass towards the center of the hydrogel indicating a limitation of gas exchange. For this reason, subsequent experiments were conducted using hydrogels printed in a 29 x 29 mm grid configuration to

achieve a higher surface area to volume ratio and thus gas exchange, resulting in a greater density of biomass per unit volume.

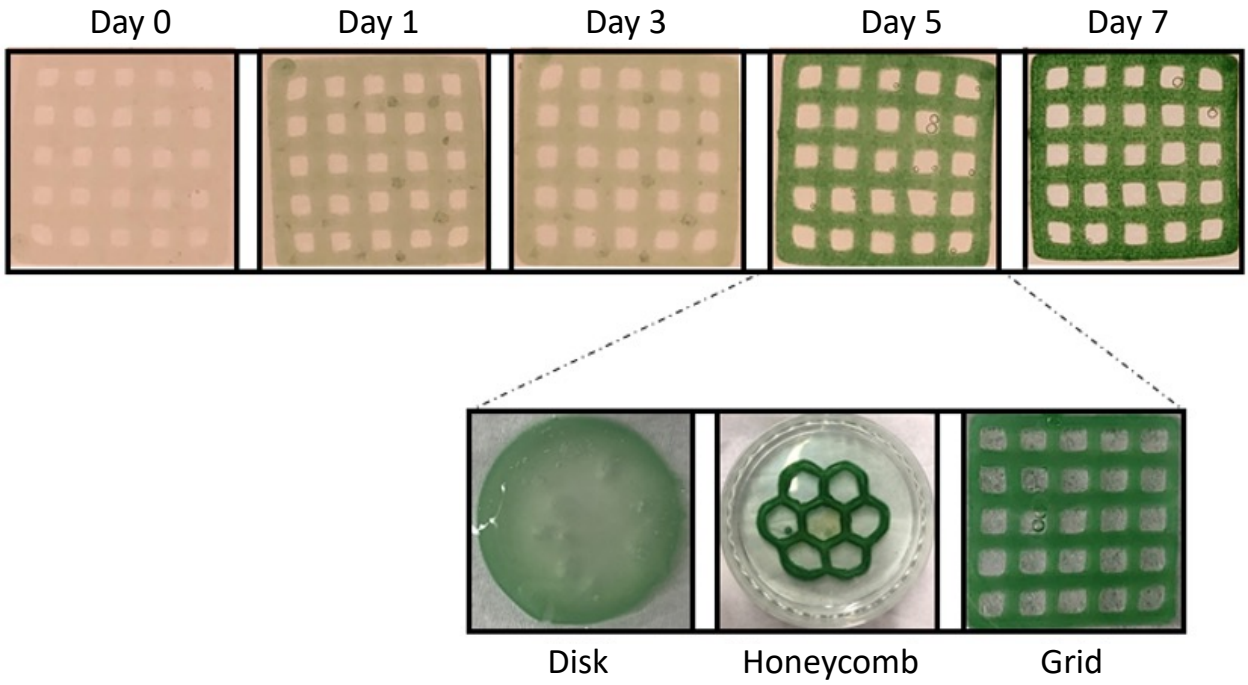

Figure 4.4. Growth of cyanobacteria within a 3D printed grid formation over 7 days. Images of five-day old hydrogels printed in a disk, honeycomb and grid geometry are included for comparison.

To visualize the proportion of viable to senescent cells within the hydrogel, constructs were imaged for chlorophyll autofluorescence and cell-death by proxy of SYTOX™ Blue (**Figure 4.5**). Red fluorescence patches, indicative of healthy colonies of cyanobacteria, were visible over seven days of growth, whereas cells stained for cell-death appeared stochastically and in low numbers.

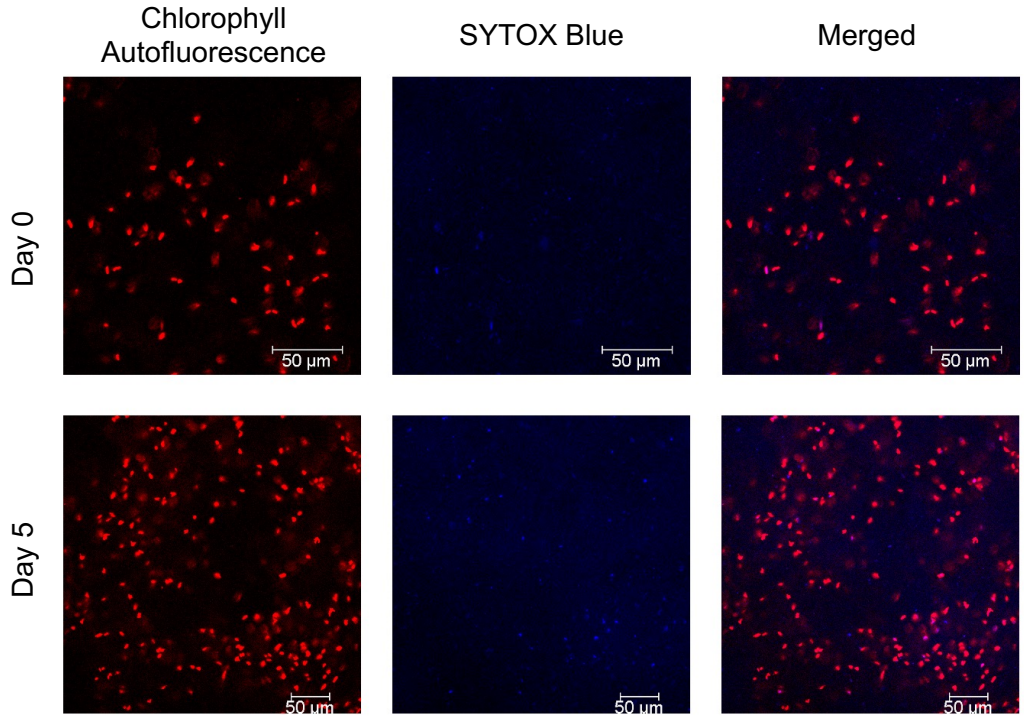

Figure 4.5. Confocal microscopy images of chlorophyll autofluorescence and SYTOX blue of a hydrogel containing wild-type *S. elongatus* cells after printing (day 0) and 5 days of growth.

Regulation of YFP expression in hydrogel

To investigate whether the viable cells grown within the hydrogel were capable of responding to an external chemical stimulus, *S. elongatus* was transformed with plasmid constructs pAM4909, pAM5027, and pAM5057 to yield strains YFP^+ (a constitutive expression YFP positive control), YFP^- (a negative control) and RiboF-YFP, respectively. While the YFP^+ construct contains a constitutive *con*II promoter driving the expression of YFP, the RiboF-YFP construct contains a theophylline-responsive riboswitch cloned upstream of the YFP reporter. After treatment with 1 mM theophylline or a 1% dimethyl sulfoxide (DMSO) vehicle control for 24 hours, YFP expression was determined qualitatively within the hydrogel using confocal fluorescence microscopy (**Figure 4.6A**). No YFP fluorescence was observed from hydrogels

containing the YFP$^-$ strain with the addition of either 1 mM theophylline or 1% DMSO. YFP fluorescence was observed from hydrogels containing the YFP$^+$ strain with the addition of either 1 mM theophylline or 1% DMSO. For hydrogels containing the RiboF-YFP strain, a similar level of fluorescence to hydrogels containing the YFP$^+$ strain was observed with the addition of 1 mM theophylline, while no YFP fluorescence was observable in hydrogels supplemented with 1% DMSO, demonstrating that the cells embedded within the hydrogel are capable of responding to external chemical stimuli and can be engineered for tight regulation of expression. To assess whether any cells that may have leaked from the hydrogel into the surrounding medium were responsive to chemical stimuli, medium from 5-day old hydrogels containing the YFP$^-$, YFP$^+$, or RiboF-YFP strains was incubated with 1 mM theophylline or 1% DMSO for 24 hours and quantified with a fluorescence plate reader. Significantly greater levels of fluorescence were detected in supernatants from the RiboF-YFP containing hydrogel in samples induced with theophylline, while no significant difference was observed between induced and uninduced samples of supernatants from all other hydrogels (**Figure 4.6B**).

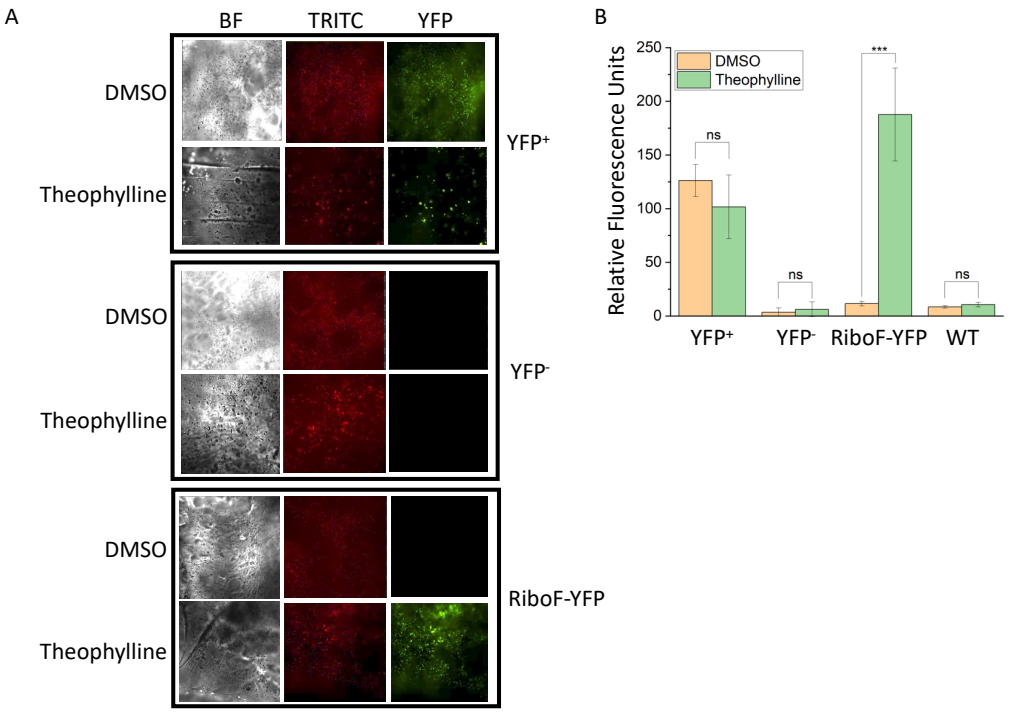

Figure 4.6. Fluorescence microscopy images of hydrogels containing YFP mutants. Hydrogels containing the YFP^{+}, YFP^{-}, and RiboF-YFP strains were supplemented with either 1% DMSO, and 1 mM theophylline and were A) images for brightfield, TRITC, or YFP fluorescence, or B) separated from the supernatant, and the supernatant of each strain was measured for YFP fluorescence.

Construction of laccase expression strains and activity of hydrogel containing strain against ABTS

In the interest of creating hydrogels embedded with cyanobacteria with properties tailored for bioremediation, a plasmid (pAM5825) was generated that encodes a laccase enzyme (*cotA*) previously demonstrated to have activity against ABTS and various dyes (Liang et al., 2018) expressed from the constitutive *con*II promoter with flanking sites for recombination into a neutral site of the *S. elongatus* chromosome. The construct was chromosomally inserted into *S. elongatus* to create strain cotA-riboF-0766 (**Figure 7A)** and printed in hydrogels in tandem with a corresponding control [WT ($Sp^{R}Sm^{R}Gm^{R}$)]. Expression of the 52 kDa CotA was confirmed on an SDS-PAGE gel (**Figure 7B**). Both the hydrogel constructs and surrounding media were

subsequently tested for laccase activity against the substrate 2,2′ -Azino-bis-(3-ethylbenzothiazoline-6-sulfonic acid) (ABTS) as described in Bourbonnais and Paice (1992) . The hydrogels were separated from their surrounding media and submerged in a buffer solution containing ABTS at a final concentration of 2 mM ABTS.

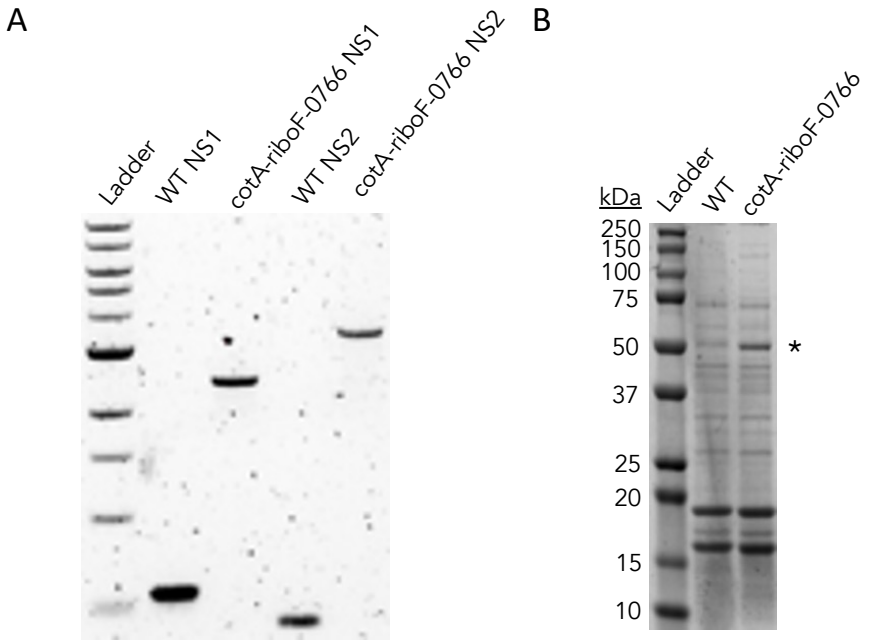

Figure 4.7. Gels characterizing the strain cotA-riboF-0766. A) genotypic characterization of the cotA-riboF-0766 strain. Lane 1, standard 1-kb ladder (NEB); lane 2, amplification of WT gDNA with primers surrounding neutral site 1; lane 3, amplification of cotA-riboF-0766 gDNA with primers surrounding neutral site 1; lane 4, lane 2, amplification of WT gDNA with primers surrounding neutral site 2; lane 5, PCR products of cotA-riboF-0766 gDNA with primers surrounding neutral site 2. B) SDS-PAGE of protein extracted from WT and cotA-riboF-0766 under standard lab conditions with band corresponding to CotA size indicated by an *.

Following 1 hour of incubation, a set of hydrogels containing WT ($Sp^RSm^RGm^R$) and cotA-riboF-0766 saturated with ABTS solution were removed, placed on sterile agar LB plates, and left to incubate for 4 days (**Figure 4.8**). Over the 4-day period, a purple coloration developed in the cotA-riboF-0766 hydrogel indicative of the oxidation of ABTS, while the hydrogel

containing the WT ($Sp^RSm^RGm^R$) strain remained the consistent green produced by cyanobacterial pigments that was observed in all constructs at time 0.

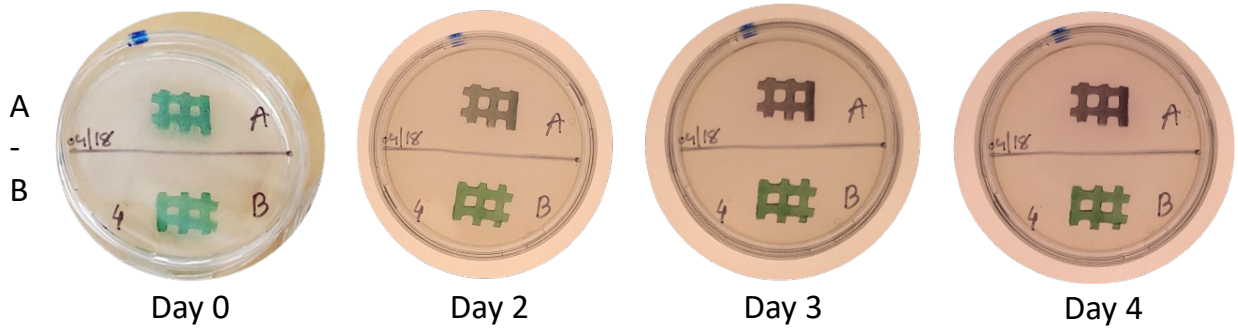

Figure 4.8. Visual assay of hydrogel ABTS oxidation activity over four days. A) Subsection of a hydrogel containing strain cotA-riboF-0766. B) Subsection of a hydrogel containing the WT strain.

To quantify the laccase activity of the hydrogel, a set of hydrogels containing WT ($Sp^RSm^RGm^R$) and cotA-riboF-0766 and a blank hydrogel were submerged in a buffer solution containing ABTS and incubated in solution for 4 days with daily sampling for quantification of the oxidation of ABTS in the reaction buffer (**Figure 4.9**). After 24 hours, 71.5 ± 13.6 nmol/ml of ABTS was oxidized by the cotA-riboF-0766 hydrogel. A small, yet significantly greater level of activity against ABTS was observed in the WT ($Sp^RSm^RGm^R$) relative to the blank hydrogel. Over the course of 4 days of incubation, the level of oxidized ABTS from the cotA-riboF-0766-containing hydrogel increased to 172.0 ± 21.3 nmol/mL and was significantly greater than either the WT ($Sp^RSm^RGm^R$)-containing or blank hydrogels (day one P value > 0.05; days two-four P value > 0.01).

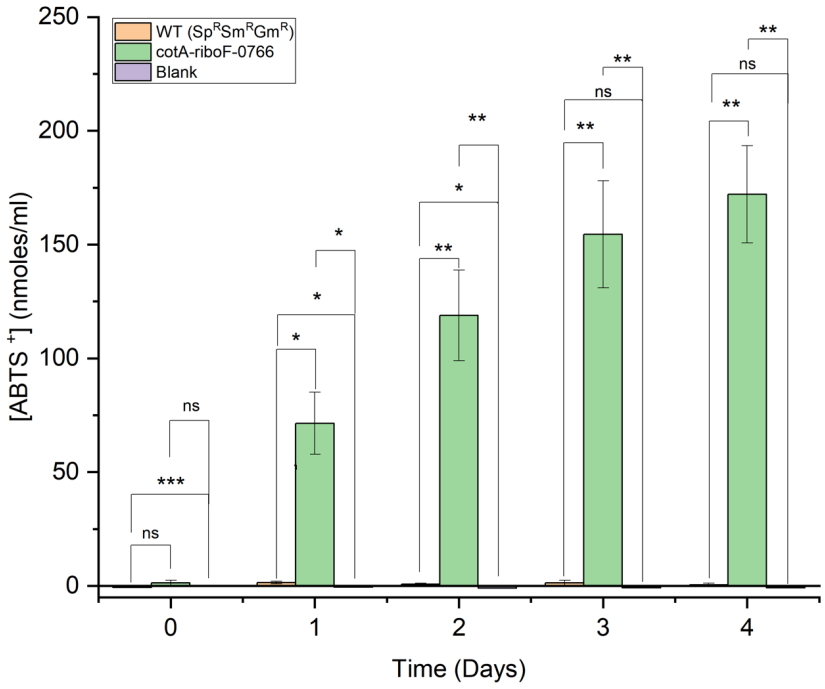

Figure 4.9. Time-course of the oxidation of ABTS in reaction buffer with the addition of hydrogels containing either the WT control strain, cotA-riboF-0766, or a blank hydrogel.

The laccase activity of the supernatant of media surrounding hydrogels was measured from samples taken five days post-printing, to assess whether the CotA enzyme escapes from the hydrogel, either by means of secretion or cell lysis within the gel (**Figure 4.10**). The activity observed from the supernatant surrounding the cotA-riboF-0766-containing hydrogels was significantly greater than either the WT ($Sp^RSm^RGm^R$)-containing or blank hydrogels. However, a significantly greater level of ABTS oxidation was observed in supernatants from WT ($Sp^RSm^RGm^R$)-containing hydrogels relative to blank hydrogels at each timepoint, indicating that the secretion or lysis products of the WT *S. elongatus* strain also confer some level of oxidative potential against the substrate ABTS, albeit a reduced level relative to the cotA-riboF-0766-containing hydrogels.

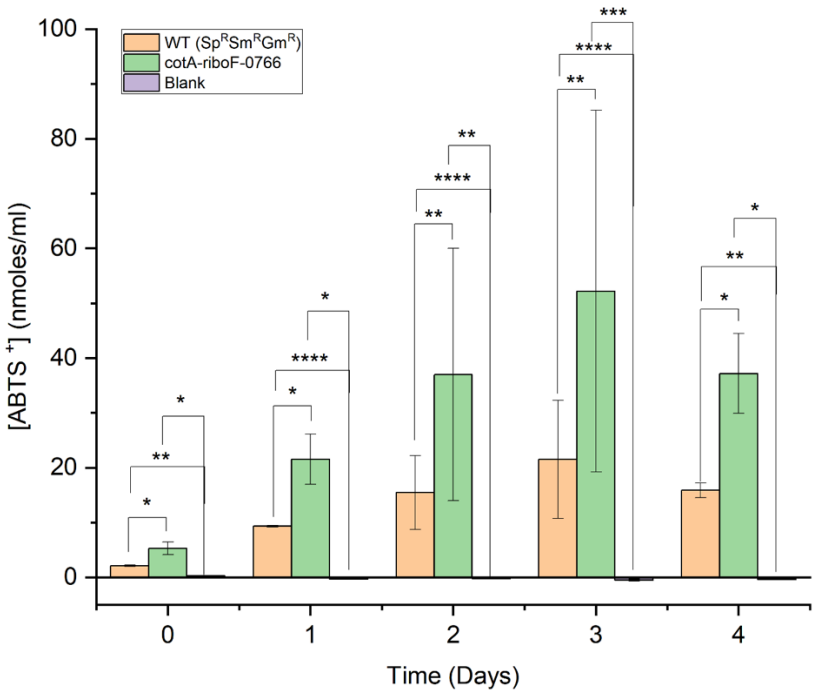

Figure 4.10. Time-course of the oxidation of ABTS in reaction buffer with the addition of supernatant surrounding either the WT control strain, cotA-riboF-0766, or a blank hydrogel.

To test the utility of the riboswitch regulatory mechanism designed for the expression of YFP in the hydrogels, plasmid construct pAM5826 was created containing a theophylline-responsive riboswitch upstream of the *cotA* gene of pAM5825, and this gene was chromosomally inserted into *S. elongatus* to produce strain RiboF-cotA. After 5 days of growth, hydrogels containing strain RiboF-cotA, WT controls [WT (Sp^RSm^R)], and blank hydrogels were transferred to fresh BG-11 medium supplemented with either 1 mM theophylline or 1% DMSO and incubated for 72 hours. The hydrogels were then transferred to a solution of reaction buffer with 2 mM ABTS, incubated for 24 hours, and the reaction buffer was measured for concentrations of oxidized ABTS (**Figure 4.11**). No oxidized ABTS was detected in either the WT (Sp^RSm^R)-containing or blank hydrogel samples. Levels of oxidized ABTS were 3.4-fold higher in samples with theophylline induction relative to uninduced samples. While these results

indicate that the riboswitch system induces the CotA enzyme within the hydrogel, the system is not as tightly controlled for the expression of CotA as was true for YFP.

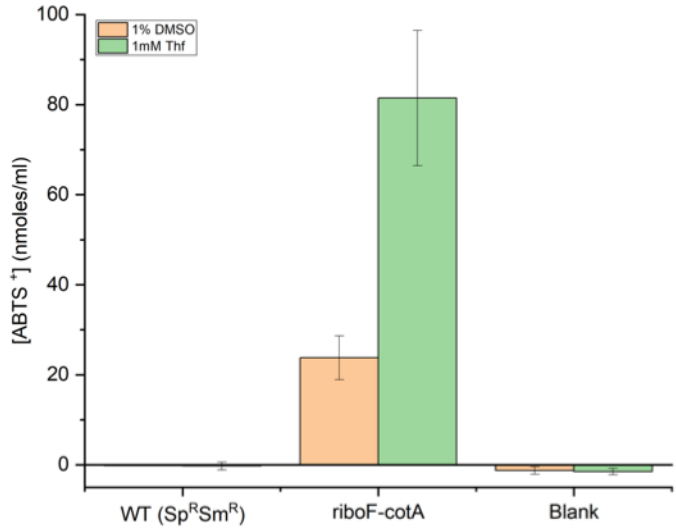

Figure 4.11. Oxidation of ABTS in reaction buffer by hydrogels containing either strains WT, RiboF-cotA or a blank hydrogel, pre-incubated with either 1% DMSO or 1mM theophylline.

Activity of hydrogel containing a laccase expression strain against indigo carmine

To assess whether hydrogels containing strains of *S. elongatus* capable of producing CotA are capable of breaking down other common pollutants, such as the dye indigo carmine, five-day old hydrogels containing either cotA-riboF-0766 or WT ($Sp^RSm^RGm^R$) and a blank hydrogel were submerged in a BG-11 solution containing indigo carmine at a starting concentration of 0.1 mg/ml. The decolorization of indigo carmine was subsequently monitored over the course of 10 days and quantified by proxy of absorption at 612 nm, the absorption maximum of indigo carmine in the visible spectrum (**Figure 4.12**). The cotA-riboF-0766-containing hydrogel samples had an average decolorization of 72.8 ± 6.8 %, while the WT ($Sp^RSm^RGm^R$) and blank hydrogel had decolorization averages of 3.8 ± 1.0 % and 18.1 ± 2.0 %, respectively. The percent decolorization in WT ($Sp^RSm^RGm^R$)-containing and blank hydrogels is due to absorption of indigo carmine by the alginate polymer matrix, as has been previously

reported for other substrates (Chan et al., 2010; Zhang and Zhao, 2020), and is observable in the blue hue of blank hydrogels removed from the solution (**Figure 4.12**).

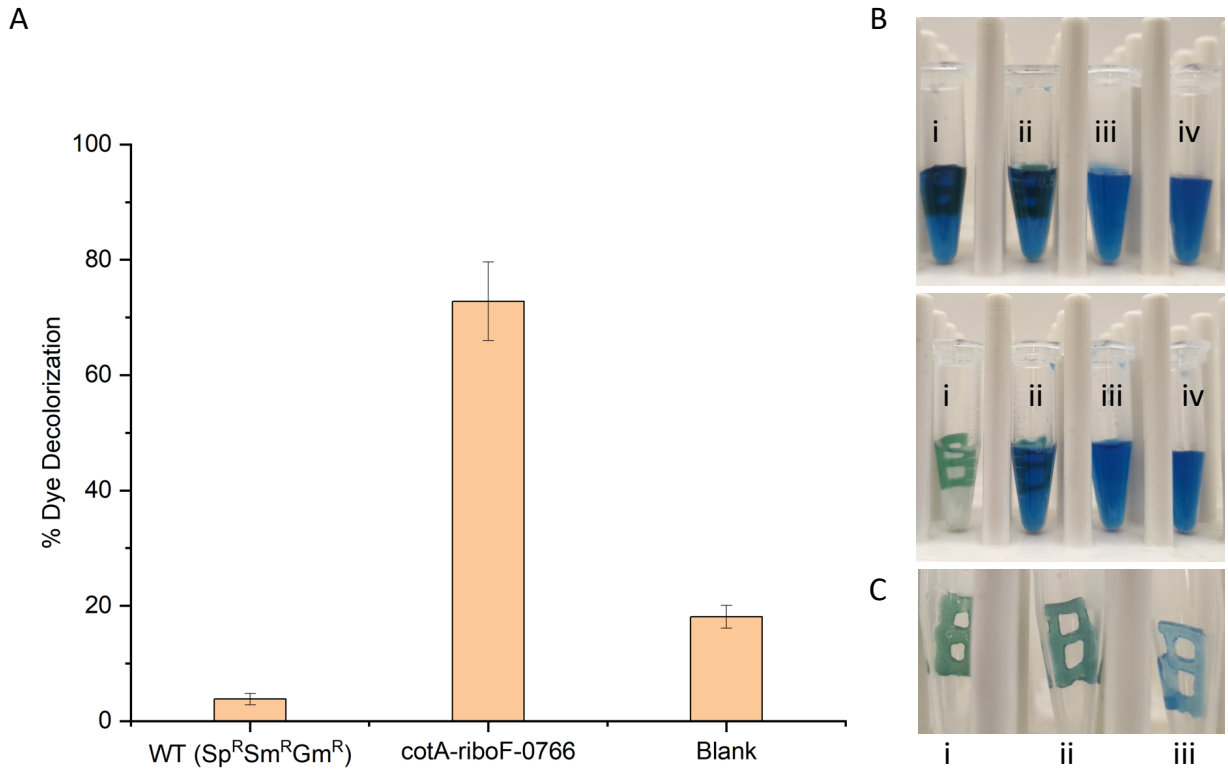

Figure 4.12. Decolorization of indigo carmine by hydrogels printed with either WT or cotA-riboF-0766 strains, or a blank hydrogel. A) Percent decolorization of indigo carmine (0.1 mg/mL) in BG-11 after incubation with hydrogels for 10 days. B) Images of hydrogels at incubation time 0 (top) and after 10 days of incubation (bottom). Roman numerals indicate the addition of i) a hydrogel printed with cotA-riboF-0766, ii) a hydrogel printed with WT, iii) a hydrogel blank, iv) BG-11 only. C) Hydrogels removed from supernatant after 10 days of incubation.

Photosynthetic activity of living hydrogels

To assess the photosynthetic activity of the living hydrogels, the O_2 microhabitat and O_2 turnover of the hydrogels was measured in light and in darkness using a O_2 microsensor mounted on a motorized micromanipulator. O_2 microsensors revealed an actively photosynthesizing and hyperoxic microenvironment on the surface of the living hydrogels (**Figure 4.13A, B and C**). O_2 concentrations were slightly higher for the cotA-riboF-0766 strain (378 µM ± 4.2 SE) compared

to the WT (mean = 346 ± 4.9 SE, Tukey post hoc p =< 0.01) at an incident irradiance of 80 μmol photons m^{-2} s^{-1}. Net photosynthesis was about 1.6-fold higher for the cotA-riboF-0766 strain (0.05 nmol O2 cm^{-2} s^{-1}) compared to the WT strain (0.031 nmol O_2 cm^{-2} s^{-1}, Tukey post hoc, $p<0.01$). No O_2 evolution was detected near the surface of the blank hydrogel. Preliminary measurements of variable chlorophyll *a* fluorimetry were performed to study the photosynthetic efficiency of the living hydrogels over a range of irradiance regimes. For both algal strains, photosynthesis was saturated between 200 – 250 μmol photons m^{-2} s^{-1} and indicative of low light adaptation (**Figure 4.13D**). Electron transport above 250 μmol photons m^{-2} was fully inhibited.

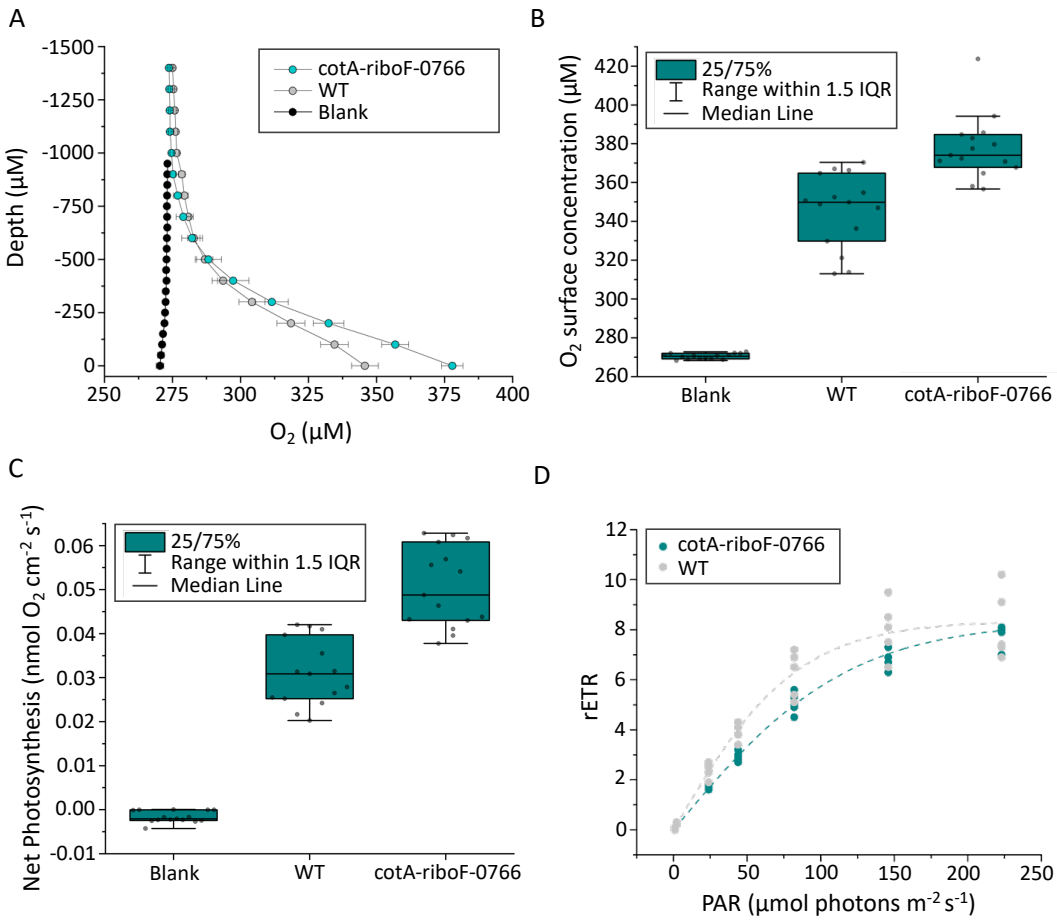

Figure 4.13. O_2 microhabitat and photosynthetic activity of living hydrogels. A) O_2 microsensor profiles were performed from the hydrogel surface (depth = 0 µm) into the overlying water column for a blank hydrogel control, a hydrogel containing the WT strain and a hydrogel containing the cotA-riboF-0766 strain. Data are means ± SEM (n=15 measurements from the 3 independent hydrogels). B) Box plot of O_2 concentrations measured at the surface of the hydrogel. C) Box plot of net photosynthesis at an incident downwelling irradiance of 80 µmol photon m^{-2} s^{-1}. D) Relative electron transport (rETR) vs. irradiance rapid light curves measured at 5 replicate spots for each printed hydrogel of the cotA-riboF-0766 and WT strains. Dotted lines indicate non-linear curve fits according to the Platt photosynthesis model (see *materials and methods*; $r^2 > 0.95$). Data above 250 µmol photons m^{-2} s^{-1} was not included as it showed full photoinhibition.

Inducible cell death of cyanobacteria in surrounding media

Because a basal level of cellular leakage from the hydrogels was observed, a system was engineered for inducible cell death as a mechanism to minimize the potential ramifications of

biofouling in natural environments by this ELM. The plasmid construct pAM5829 contains a *con*II promoter that constitutively expresses a theophylline-responsive riboswitch upstream of the native *S. elongatus* gene Synpcc7942_0766, which was chromosomally inserted during the generation of strain cotA-riboF-0766. Synpcc7942_0766, when overexpressed, results in the excision of a prophage from the *S. elongatus* genome (Adomako et al., 2022), subsequently resulting in cellular lysis (**Figure 4.14A**). Hydrogel supernatants containing cells of either cotA-riboF-0766 or WT ($Sp^RSm^RGm^R$) were supplemented with either 1 mM theophylline or 1% DMSO and growth of the cultures was monitored for four days (**Figure 4.14B**). In 48 hours, ectopic induction of Synpcc7942_0766 in cotA-riboF-0766 supplemented with 1 mM theophylline resulted in a decrease in OD_{750}, indicating senescence of the culture. Samples of cotA-riboF-0766 supplemented with 1% DMSO, and cultures of WT ($Sp^RSm^RGm^R$) supplemented with either 1 mM theophylline or 1% DMSO continued to grow at similar rates, demonstrating the utility of engineered inducible cell death in an ELM as a mechanism of reducing biological fouling.

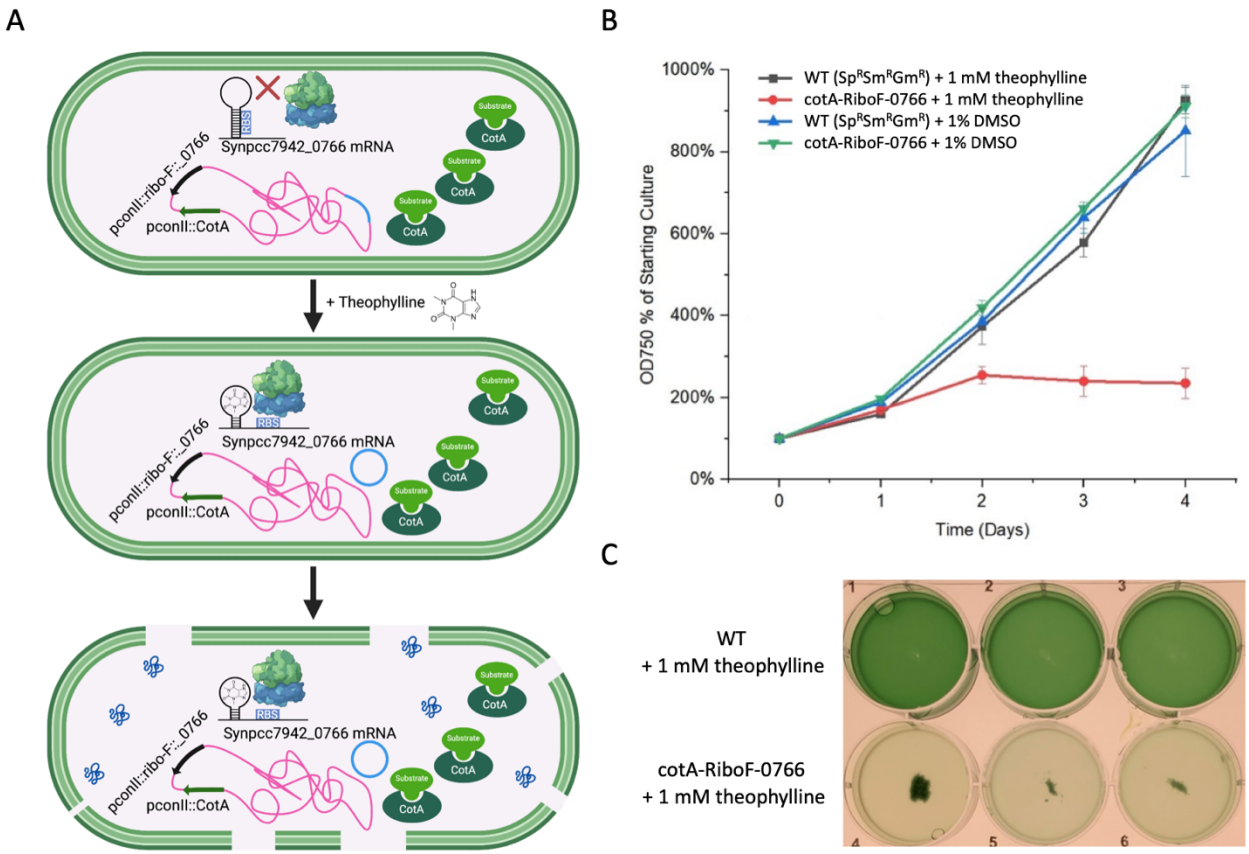

Figure 4.14. Inducible cell death of strain cotA-riboF-0766. A) Schematic of constitutive expression of CotA, and riboswitch conformation change with the addition of theophylline, leading to the overexpression of Synpcc7942_0766, prophage excision and subsequent cell death. B) Growth curves of the WT control strain and cotA-riboF-0766 with addition of either 1 mM theophylline or 1% DMSO. C) Image of liquid cultures of WT and cotA-riboF-0766 three days post supplementation with 1mM theophylline or DMSO.

Discussion

We optimized the composition of an alginate-based hydrogel for 3D printing and viability of the cyanobacterium *S. elongatus* and engineered several strains of the cyanobacterium to be stimulus-responsive and produce various functional outputs when embedded within the hydrogel. While ELMs have been constructed with cyanobacteria as a biological component (Sawa et al., 2017; Joshi et al., 2018; Han et al., 2020), the well-established genetic toolkits for synthetic biology in cyanobacteria have not previously been utilized for the development of photosynthetic

ELMs with functional outputs and tailored regulatory circuits. In this study we leveraged the use of riboswitches to regulate gene expression within the living material to produce a stimulus-responsive material with the capacity for dye-decolorization and inducible cell death to prevent biofouling.

Oxygen measurements conducted with microsensors on the living hydrogels revealed an actively photosynthesizing and O_2 rich microhabitat for both WT and cotA-riboF-0766 strains. Hydrogels containing *S. elongatus* were capable of growing from low initial cell densities under low to moderate light; however, growth halted in samples grown under irradiances greater than 300 μmol photon m^{-2} s^{-1}. Photosynthesis vs irradiance curves support saturation of photosynthesis at similar irradiance levels for these low-light adapted hydrogels. Given that solar radiation levels incident on Earth's surface can reach approximately 2000 μmol photons m^{-2} s^{-1}, freshly printed biocomposites will likely suffer in natural high-light environments. However, aquatic environments such as lakes and rivers often contain large concentrations of colored dissolved organic matter and rapidly attenuate light with depth, providing a hospitable environment for the ELMs presented here.

Given an average *S. elongatus* cell size of approximately 1 μM, and that the pore sizes observed in the biocomposite hydrogel exceed 60 μM, the diameter of constrictions within cavities of the hydrogel are not a limitation to growth of the cyanobacteria within the matrix. We assume that the apparent homogeneity of *S. elongatus* cells in the hydrogel after incubation and growth is largely a product of mixing prior to printing and subsequent colony formation, as the WT strain does not exhibit taxis. However, diffusion of cells throughout the hydrogel via mechanical agitation in an aqueous solution will occur at some level, as evidenced by low levels of cells present in the supernatant surrounding hydrogels after 5 days of incubation. The

theophylline-inducible riboswitch regulation of inducible cell death incorporated into *S. elongatus* strain cotA-riboF-0766 serves as a mechanism to remedy such leakage of cells to the surrounding environment.

Riboswitches are increasingly being used for applied bioengineering due to the simplicity of ligand-aptamer interactions (Weigand and Suess, 2009; Verhounig et al., 2010; Ma et al., 2014). The use of riboswitches to regulate protein expression within the hydrogels was successful for both YFP and CotA and should function well in future biocomposites that contain alternative cyanobacterial or algal strains. We attribute the success of regulation by riboswitches to the diffusion of the small molecule theophylline throughout the porous hydrogel. While YFP fluorescence was undetectable by fluorescence microscopy in uninduced RiboF-YFP strains, moderate levels of laccase activity were detected in uninduced RiboF-cotA samples. This is likely due to the high activity of CotA and low level of the enzyme required to oxidize ABTS. For future applications requiring tighter regulation of protein products, incorporating multiple riboswitches or pairing transcriptional regulatory systems with different riboswitches, could be used to fine-tune expression.

To assess the capability of the hydrogels to serve as a tool for bioremediation, hydrogels containing ecotA-riboF-0766 or and controls were tested for their ability to decolorize indigo carmine, an activity previously demonstrated for a cyanobacterial-expressed laccase (Liang et al., 2018). Our hydrogel was successful in decolorizing approximately 80% of indigo carmine present in BG-11 medium over the course of 10 days. The hydrogel has the added benefit of being physically removable from the system without the need for energy intensive steps required to clarify a liquid culture, such as centrifugation. The blank hydrogel also produced a significant level of apparent indigo carmine decolorization due to the absorption of indigo carmine by the

hydrogel matrix itself. Interestingly, the blank hydrogel consistently had a greater level of decolorization than hydrogels containing the control strain. It is conceivable that prints containing cells, by definition, contain less polymeric material than blank prints, and this difference in alginate material volume accounts for the reduction in apparent decolorization observed in constructs containing the control strain relative to blank hydrogels.

While the photosynthetic ELMs designed in this study have functional outputs suitable for bioremediation, there are numerous improvements that could be made to make the material more scalable and appropriate for use in the natural environment. Notably, improvements in enzymatic activity per unit volume of hydrogel will be necessary to move from the laboratory scale to large scale applications, such as bioremediation in lakes or rivers. One strategy would be modifying protein products to be tagged for secretion from the cell, ultimately removing the limitation of intracellular space for the storage of heterologously expressed products. Knowledge of mechanisms and systems for the secretion of recombinant proteins in cyanobacteria such as *S. elongatus* PCC 7942 is still in its infancy (Russo et al., 2022), and expansion of this domain of knowledge will greatly benefit the output potential of cyanobacterium-based ELMs. Secondly, careful consideration should be paid to the influence that materials containing biological components may have on the natural environment, such as biofouling and subsequent effects on ecological systems. The ELM presented here addresses this issue by incorporating a mechanism for inducible cell death in aqueous solutions with the addition of the small molecule theophylline. While theophylline is a natural product present in small quantities in tea and cocoa, it is not native to aquatic systems and should not be used for induction in the environment for risk of unintended chemo-ecological consequences. Alternative regulatory circuits with more natural inductive signals could be engineered for use in the natural environment. For example,

the use of spectrally responsive photoreceptors or temperature-sensitive signaling transduction pathways could allow for diurnal or seasonal cell death of biological fouling. An alternative approach to reduce leakiness from the hydrogel could be the addition of a clear, non-toxic polymer with pore sizes less than 1 μM to serve as a physical barrier to biological matter while still allowing for nutrient, gas, and substrate exchange.

The ELM presented here serves as a proof-of-concept for the engineering and incorporation of cyanobacteria into a polymeric matrix to produce a stimuli-responsive material with functional outputs of real-world utility. Utilizing cyanobacteria as the biological component, these ELMs fundamentally depend on only light, CO_2 as a carbon source, and minimal nutrients for survival. While applications of the biocomposites demonstrated here have been linked to bioremediation, potential functional outputs are vast and could be engineered to extend to many fields.

Materials and Methods

Cultivation of cyanobacteria

Wild type and genetically engineered Synechococcus elongatus (PCC 7942) cyanobacterial cells were cultivated in BG-11 medium (Allen, 1968) in conical flasks and grown at 30° C while shaking at 120 rpm under continuous illumination of 75 μmol photons m^{-2} s^{-1}. BG-11 was supplemented with 2 μg/ml spectinomycin, 2 μg/ml streptomycin, and/or 2 μg/ml gentamycin, depending on the strain type. Unless otherwise noted, cells were grown for 5-6 days from an initial OD_{750} of 0.05 into mid-log phase (OD_{750} = 0.5-0.6) prior to the preparation of bioinks.

Preparation of alginate ink and bioinks

Alginate hydrogels were prepared using a mixture of sodium alginate with $CaSO_4$ and $CaCl_2$ as crosslinking agents at optimized concentrations. In brief, a 4% w/v sodium alginate solution was prepared by dissolving sodium alginate powder (Sigma-Aldrich) in autoclaved deionized water. The solution was continuously stirred overnight at room temperature achieving a clear, viscous solution. Stock solutions of $CaSO_4$ and $CaCl_2$ were prepared in autoclaved deionized water at concentrations of 50 mM and 100 mM, respectively. All solutions were stored at 4 °C until use. A hydrogel ink solution was prepared for printing by mixing the alginate solution and $CaSO_4$ in a 2:1 ratio. The slurry suspension of 50 mM $CaSO_4$ was mixed thoroughly (25-30 times) with alginate solution using an in-house fabricated 3-way syringe mixer and then transferred to a 3cc syringe for 3D printing. The ink in the 3cc syringe was placed within a 50 mL falcon tube and centrifuged at 4000 rpm for 10 min to remove any air bubbles prior to printing.

Bioinks were prepared by sampling liquid cultures cells at an OD_{750} of 0.5-0.6 and centrifuging the cells at 3500 x g for 5 min. The pellet was then mixed in the plotting paste using the 3-way syringe mixer. All glassware used in the process was pre-sterilized by autoclave and all accessories required for cell mixing and 3D printing were pre-sterilized by UV sterilization. Both the ink and the bioink were prepared fresh prior to each experiment.

3D printing of alginate ink and bioinks

$CaSO_4$ was used to partially crosslink the alginate chains to make the gel suitable for Direct-Ink-Writing (DIW) printing. Various combinations of alginate solutions (0.5-5% w/v) and $CaSO_4$ (25-100 mM) concentrations were tested at different pressures (50-350 kpa) using steel

blunt end syringe needles (22, 27, and 32 gauge sizes) to optimize conditions for printability. The homogeneous mixture that gave the most stable structure at a given needle size and pressure was used for printing the bioink. In brief, the ink with or without cyanobacterial cells was loaded in a 3 cc printing syringe barrel, equipped with a 27 gauge needle. The ink was 3-D printed with a pre-designed geometry using the Inkredible+ Bioprinter (Cellink, USA). The printing parameters were as follows: pressure ~200 kPa, infill density 50%, fill pattern rectilinear, and speed 80 mm/sec. All prints were produced out in ambient conditions at room temperature. The printed geometries were designed using CAD software and converted to Gcode using the Cellink Heartware software. Ink without *S. elongatus* cells was used to construct blank hydrogels in all experiments.

Post printing, the multilayered 3D-printed structures were immersed in 100 mM $CaCl_2$ for 15 mins to allow the patterns to be fully crosslinked and then incubated in Petri dishes in BG-11 medium supplemented with antibiotics. The scaffolds were kept in an incubator at an irradiance level of 20 μmol photons m^{-2} s^{-1} and 28 °C for initial growth prior to experimentation.

Growth optimization of the 3D-printed S. elongatus scaffolds

The growth of *S. elongatus* cells was monitored and optimized in different geometries of 3D-printed patterns over time. Specifically, cells encapsulated in three different printed structures (the disk, honeycomb and grid) were incubated in BG-11 medium with constant illumination for 7 days and were visually monitored for color density over time. Images were taken at regular time intervals.

Cell viability of the 3D-printed S. elongatus structures

Cell viability within the 3D-printed constructs was assessed using confocal microscopy. Live/dead cell assays were performed by imaging chlorophyll autofluorescence and SYTOX Blue (SB; Fisher Scientific) stain fluorescence. In brief, 3D-printed grid patterns were divided into twelfths, yielding two interconnected hollow squares, under sterile conditions and incubated for 5 min in the dark, with 5 µL of a 1 mM SB stock solution in 1 mL of BG-11 medium. The effective concentration of the stain was 5 µM. After incubation the samples were washed three times with BG-11 and analyzed on a Leica Sp8 confocal microscope with Lightning Deconvolution and White Light Laser. The channel for SB detection was set at excitation 405 nm and the emission was collected at 450–510 nm. The channel for chlorophyll autofluorescence was set at excitation 488 nm and the emission was collected at 685-720 nm. Images were taken at intervals to monitor growth.

O_2 microsensor measurements

Clark-type O_2 microsensors (tip size 25–50 µm, Unisense, Aarhus, Denmark) were used to measure the O_2 microhabitat and O_2 turnover of the living hydrogels in light and in darkness. Microsensor measurements were performed as described previously (Wangpraseurt et al., 2020, 2022). Briefly, O_2 sensors were mounted on a motorized micromanipulator (MU1, Pyroscience GmbH, Germany) that was attached to an optical table. Living and blank hydrogels were placed in a custom-made acrylic system that provided slow laminar flow at a rate of approximately 1 cm/s. O_2 microsensor measurements were performed at the cross-section between the printed horizontal and vertical areas. Preliminary O_2 mapping suggested that these are the areas of highest photosynthetic activity. Microsensor profiles were generated by carefully positioning the

sensor at the surface of the hydrogel with the aid of a digital microscope (Dinolite, US). O_2 profiles were measured from the hydrogel surface through the diffusive boundary layer into the overlying water column in steps of 50-100 µm using the motorized micromanipulator. Net photosynthesis was determined at an incident downwelling irradiance of 80 µmol photons m^{-2} s^{-1} as provided by a fiber optic halogen light source (ACE, Schott GmbH). Dark respiration was calculated as the diffusive O_2 flux in darkness. The diffusive O_2 flux was calculated using Fick's first law of diffusion as described previously (Wangpraseurt et al., 2020) using a diffusion coefficient of $DO_2 = 2.2186 \times 10^{-5}$. For each experimental treatment (blank hydrogel control, WT strain and cotA-riboF-0766) a total of 15 replicate measurements were performed from three printed hydrogels.

Variable chlorophyll a fluorimetry

An I-PAM variable chlorophyll fluorescence imaging system (Mini I-PAM, Walz) was equipped with blue light-emitting diodes (460 nm) delivering a maximum saturation pulse intensity (SP = 10) of 2,700 mmol photons m^{-2} s^{-1} (Wangpraseurt et al., 2019). Relative electron transport rates were determined with dark adapted samples (30 min dark adaptation) as described previously (Ralph and Gademann, 2005). For each printed hydrogel of the WT and cotA-riboF-0766 strain, five spots were selected for photosynthetic yield analysis. It should be noted that most cyanobacteria have maximal fluorescence yield with red-orange excitation and very limited yield upon blue excitation, due to the lack of chlorophyll *b* and the enhanced contribution of photosystem I (Trampe and Kühl, 2016). Thus, the derived rETR curves have to be interpreted with caution and likely underestimate the true photosynthetic potential of the living hydrogels.

Rheological Characterization and Viscosity measurements

Viscoelastic moduli and viscosity measurements of the alginate ink, with and without the inclusion of cells, were carried out using a Discovery™ HR-30 Hybrid Rheometer (TA Instruments™). Both measurements were conducted using a 20 mm parallel plate geometry in a Peltier plate setup. For amplitude sweep measurements, angular frequency was 10 rad/sec and strain ranged from 0.01 % to 1000.0 %. For viscosity, flow sweep was measured at a continuous shear rate of 0.01 s^{-1} to 1000.0 s^{-1}. All characterizations were conducted at a temperature of 25 °C.

Field Emission Scanning Electron Microscopy

Electron Microscopy images of multiple regions over freeze-dried hydrogel samples, printed with and without cells, were taken on an FEI Apreo FESEM (Thermo Scientific). In brief, sample subsections were cut and stored at -80 °C for 24 hours. The samples were subsequently lyophilized to remove any residual water and the dried samples were prepared for imaging. The samples were adhered to SEM sample stubs using double sided carbon tape and were coated uniformly with gold particles for 60 msec. Images were taken using an ETD detector at 10-20kV.

Fluorescence microscopy

Images of hydrogel constructs were captured on a Nikon Eclipse Ni fluorescence microscope equipped with a Nikon DS Qi2 camera at 20x or 40x magnification. Brightfield, chlorophyll autofluorescence and YFP fluorescence images were captured for each sample.

YFP fluorescence measurements

The emission intensity of YFP from hydrogel samples were measured in 96-well plate with a Tecan Infinite® M200 plate reader (TECAN). The excitation and emission wavelengths were set for YFP to excitation 490/9 nm and emission 535/20 nm. Measurements were taken from hydrogels containing 3 independent clones of each strain.

SDS-PAGE of CotA

Cultures of WT ($Sp^RSm^RGm^R$) and cotA-riboF-0766 were grown in liquid culture under 75 μmol photons m^{-2} s^{-1} with continuous shaking at 30 °C to an OD_{750} of 0.5. 10 mL of cultures were pelleted by centrifugation at 4500 x g and aspirated. The pellets were then resuspended in 1 mL of cold lysis buffer (50mM Tris-HCl pH 8.0, 150mM NaCl) and supplemented with 1 mM PMSF and protease inhibitor cocktails. The samples were then homogenized in a BeadBlaster™ 24R (Benchmark Scientific) at 4 °C. The crude protein was then clarified by centrifugation at 4 °C for 20 min at 18,000 x g, after which the crude protein concentration was determined using a Pierce Coomassie Plus Protein Assay (Bradford), with bovine serum albumin used as a standard. After boiling the sample with 2x Laemmli Sample Buffer, 30 μg of sample was loaded into a Mini-PROTEAN® TGX™ Precast Gel (Bio Rad) and run at 150V. The gel was then incubated in InstantBlue Coomassie Protein Stain (Abcam) overnight prior to imaging.

ABTS activity assays

Laccase activity of either the hydrogels or the surrounding supernatant was measured using 2,2′ -Azino-bis-(3-ethylbenzothiazoline-6-sulfonic acid) (ABTS) (Thermo Fisher

Scientific). Hydrogel ABTS activity measurements were conducted by adding an approximately 83.25 mm^3 subsection of a hydrogel sample to a 1 mL reaction mixture of 100 mM sodium acetate buffer, 3.16 μM $CuSO_4$, pH 5.0, and 2 mM ABTS in a 1.5 ml conical microtube. A blank reading at 420 nm consisting of the reaction mixture without a hydrogel was subtracted from all hydrogel samples. Hydrogel supernatant ABTS activity measurements were conducted by centrifuging 1 mL of the supernatant surrounding a hydrogel for 5 minutes at 4500 x g and combining 500 μL of the supernatant with 460 μL 200 mM sodium acetate buffer, pH 5.0, and 40 μL of a 50 mM stock of ABTS for a final concentration of 100 mM sodium acetate buffer, pH 5.0, and 2 mM ABTS. A blank reading at 420 nm consisting of the BG-11 in the reaction mixture was subtracted from all supernatant samples. The oxidation of ABTS was determined by measuring absorbance of the reaction mixture at 420 nm (Childs and Bardsley, 1975) after a 1 or 24 h incubation in darkness at 28 °C, relative to the absorbance at 0 h. For assays involving the induction of RiboF-cotA, an approximately 83.25 mm^3 subsection of a hydrogel was added to 1 mL of BG-11 in a 2 mL Eppendorf tube and supplemented with either 1 mM theophylline (Sigma-Aldrich; 100 mM stock dissolved in 100% DMSO) or 1% DMSO as a control and allowed to incubate for 3 days under 50 μmol photons m^{-2} s^{-1} prior to conducting the ABTS assays described above.

Indigo carmine decolorization assays

The decolorization of indigo carmine by hydrogels was determined by suspending an 83.25 mm^3 subsection of a hydrogel in a 500 μL solution of BG-11 media with 0.1 mM indigo carmine (Sigma-Aldrich). Indigo carmine concentrations were determined spectrophotometrically by generating a standard curve for absorbance at 612 nm for 200 μL

samples in a 96-well plate with a Tecan Infinite® M200 plate reader (TECAN). The indigo carmine hydrogel mixture was incubated in darkness and the absorbance of 200 µL samples was measured at 612 nm at time 0, and after 3, 5, 7, and 10 days of incubation at 28 °C. The percent decolorization of indigo carmine was determined relative to absorbance at 612 nm at time 0 for a given sample.

Inducible cell death by phage lysis

Strains WT ($Sp^RSm^RGm^R$) and cotA-riboF-0766 were grown in liquid culture under 75 µmol photons m^{-2} s^{-1} with continuous shaking at 30 °C to an initial OD_{750} of 0.2 - 0.3, prior to being transferred to six-well plates in 8 ml aliquots. Samples were then induced with either 1 mM theophylline (100 mM stock dissolved in 100% DMSO) or 1% DMSO as a control. For four days following induction, both the OD_{750} of the cultures and ABTS activity of the supernatants were measured daily.

Construction of plasmids and mutant strains

To create plasmid pAM5823, AM4950 was digested with SwaI (NEB) to release the *ccdb* toxic gene, and the linearized plasmid was re-ligated with a Quick Ligase Kit (NEB) following manufacturer instructions. Plasmids pAM5824 and pAM5825 were created by digesting pAM4950 with SwaI (NEB) and performing a Gibson Assembly (NEB) between the linearized product and a *cotA* gBlocks Gene Fragment synthesized by Integrated DNA Technologies (IDT). The *cotA* gBlocks Gene Fragment contained 20 base pair ends of homology with the linearized pAM4950 product for Gibson Assembly and a *con*II promoter and ribosomal binding site upstream of the *cotA* gene. The *cotA* sequence was derived from a reverse-translation of the

protein sequence of cotA from *Bacillus subtilis* (accession number WP_003243170.1) and codon optimized for *S. elongatus*. A single point mutation in the *con*II promoter of pAM5824 was a spontaneous mutation in a single *E. coli* DH5a colony and was not present in pAM5825. pAM5826 was created by digesting pAM5051 with EcoRI (NEB), and performing a Gibson Assembly (NEB) between the linearized product and the PCR product of pAM5825 with primer pair cotA_5051-F/cotA_5051-R. pAM5829 was created by digesting pAM4940 with SwaI (NEB) and performing a Gibson Assembly (NEB) between the linearized product and the PCR product of *S. elongatus* gDNA and the primer pair 0766_riboF_pAM4940-F/0766_riboF_pAM4940-R. The sequence of all plasmids constructed in this study were verified by Sanger sequencing. Complete lists of all plasmids and primers used in this study are included in tables 4.1 and 4.2, respectively.

Table 4.1. Plasmids used in this study.

Plasmid Name	Description	Source
pAM4909	RSF1010 broad host-range plasmid with *aadA* cassette and constitutive expression of *myc-yfp* reporter driven by a PconII promoter.	Taton *et al.* 2014
pAM4940	Contains recombination arms for NS1 integration, an *aacC1* cassette, and a *ccdB* gene surrounded by SwaI restriction sites.	Taton *et al.* 2014
pAM4950	Contains recombination arms for NS2 integration, an *aadA* cassette, and a *ccdB* gene surrounded by SwaI restriction sites.	Taton *et al.* 2014
pAM5027	RSF1010 broad host-range plasmid with *aadA* cassette.	Ma *et al.* 2014
pAM5051	Plasmid containing recombination arms for NS2 integration and an *aadA* cassette, with a PconII promoter driving the expression of riboswitch-F followed by an EcoRI restriction site.	Ma *et al.* 2014
pAM5057	RSF1010 broad host-range plasmid with *aadA* cassette and riboswitch-F::*myc-yfp* reporter expression driven by a PconII promoter.	Ma *et al.* 2014
pAM5329	Plasmid containing recombination arms for NS1 integration and an *aadA* cassette.	Taton *et al.* 2017
pAM5610	Plasmid containing recombination arms for NS1 integration and an *aacC1* cassette.	This study
pAM5823	Plasmid containing recombination arms for NS2 integration and an *aacC1* cassette.	This study
pAM5824	Constitutive expression of *cotA*, driven by a PconII promoter with a single point mutation, with an *aadA* cassette and NS2 recombination arms.	This study
pAM5825	Constitutive expression of *cotA*, driven by a PconII promoter, with recombination arms NS2 integration and an *aadA* cassette.	This study
pAM5826	Plasmid containing a PconII promoter driving the expression of riboswitch-F::*cotA*, with recombination arms for NS2 integration and an *aadA* cassette.	This study
pAM5829	Plasmid containing a PconII promoter driving the expression of riboswitch-F::*Synpcc7942_0766* driven by a PconII promoter, with recombination arms for NS1 integration, and an *aacC1* cassette	This study

Table 4.2 Primers used in this study.

Primer Name	**Sequence**
cotA_5051-F	CTGCTAAGGAGGCAACAAGATGACGCTGGAAAAGTTCGTCGA
cotA_5051-R	CGAGGTCGAGACGGCTCATGTTATTTGTGGGGATCGGTGA
0766_riboF_pAM4940-F	GGCCAATAACCCAGGGATTTTTGACAATTAATCATCGGCTCG
0766_riboF_pAM4940-R	CTGCCGGGGAGCTCCTTCATTTCATGTCAGGGTTTCAGGCAG
NS1_Screen-F	ACATCGCTATCTCTTAGGACTTCG
NS1_Screen-R	GGCCGAAAATGACAAGATCAC
NS2_Screen-F	CTCCAGTAAAGTCTTCGCCCGTAAC
NS2_Screen-R	TTGGTGCTGTTCAGTCTGGATGC

Transformation of *S. elongatus* with plasmids pAM4909, pAM5027, and pAM5057 was achieved by biparental conjugation (Elhai et al., 1997). Transformation of *S. elongatus* with all other plasmids was achieved using standard protocols (Clerico et al., 2007). All *S. elongatus* transformations were performed using WT strain AMC06. Genotyping of *S. elongatus* was performed using colony PCR with Q5 DNA Polymerase (NEB), using primer pair NS1_Screen-F/NS1_Screen-R for transformations in neutral site 1 (NS1), and NS2_Screen-F/NS2_Screen-R for transformation in neutral site 2 (NS2). A complete list of strains used in this study is included in Table 4.3.

Table 4.3. Strains used in this study.

Name	Description	Plasmids Used	Source
WT	Wild-type *S. elongatus* (AMC06)		
YFP^+	Harbors RFS1010 plasmid for constitutive expression of *myc-yfp*	pAM4909	This study
YFP^-	Harbors RFS1010 plasmid. Negative control for YFP^+ and RiboF-YFP.	pAM5027	This study
RiboF-YFP	Harbors RSF1010 plasmid with *myc-yfp* expression regulated by riboswitch-F.	pAM5057	This study
RiboF-cotA	Contains PconII driving cotA expression regulated by riboswitch-F in NS1.	pAM5826	This study
WT (Sp^RSm^R)	Control strain for RiboF-cotA.	pAM5329	This study
cotA-riboF-0766	Contains PconII driving constitutive expression of cotA in NS2, and PconII driving expression of *SynPCC7942_0766* regulated by riboswitch-F in NS1.	pAM5825, pAM5829	This study
WT ($Sp^RSm^RGm^R$)	Control strain for cotA-riboF-0766.	pAM5610, pAM5823	This study

Statistics

Data are presented as the mean ± standard deviation. The definition of significance was set a priori to $p < 0.05$. Within figures asterisks represent: *, $P < 0.05$; **, $P < 0.01$; ***, $P < 0.001$; ****, $P < 0.0001$.

Acknowledgments

We thank David Wirth for assistance with the creation of the 3-way syringe mixer, Jack Reddan for assistance with the construction of pAM5825, Marie Adomako for the construction of pAM5610, and Bryan Bishe and Arnaud Taton for assistance with the conjugation of strains YFP^+, YFP^-, and Ribo-YFP. This work was sponsored by the UC San Diego Materials Research

Science and Engineering Center (UCSD MRSEC), supported by the National Science Foundation (Grant DMR-2011924). The authors acknowledge the use of facilities and instrumentation supported by the National Science Foundation through the University of California San Diego Materials Research Science and Engineering Center DMR-2011924, and the UCSD School of Medicine Microscopy core facility funded by NINDS Grant P30 NS047101. The use of microscopy core equipment was supported by Jennifer Santini and Marcella Erb.

Chapter 4, in part, is currently being prepared for submission for publication of the material as Datta D*, Weiss EL*, Wangpraseurt D, Hild E, Chen S, Golden JW, Golden SS, Pokorski JK. Bio-composite Hydrogels with Engineered Cyanobacteria Yield Stimuli-responsive Photosynthetic Materials for Bioremediation. The dissertation author was the co-primary researcher and author (*) of this material.

CHAPTER 5: Cyanobacterial-Spectral Interactions

5.1 Chapter Summary

Earlier chapters described complete bodies of work, leveraging RB-TnSeq to elucidate genes that are important for fitness under UV, the distribution of MAAs in the Southern Ocean, and the biotechnological application of phytoplankton towards ELMs. This chapter is divided into three subsections of works in progress, each of which are tangentially related to earlier chapters. Section 5.2 describes an RB-TnSeq experiment designed to identify genes in *S. elongatus* PCC 7942 that are important for fitness under qualities of light representative of natural spectral-niches. Section 5.3 describes an interaction RB-Seq (IRB-Seq) experiment designed to identify genes in *S. elongatus* that may be important for the transition from transcription of *psbAI* to *psbAII* and *psbAIII*, a mechanism by which cyanobacteria can reduce the damaging effects of high irradiance levels. Finally, section 5.4 describes a bioinformatics approach to identify strains of cyanobacteria that are capable of synthesizing MAAs and an attempt to heterologously express the MAAs in *E. coli*. These independent projects are included to guide future researchers who would like to advance the work presented here.

5.2 Genes Important for Fitness Under Discrete Spectral Niches Identified using RB-TnSeq

Introduction

Phytoplankton are dependent on photons of the wavelengths present in their surroundings for photosynthesis. The availability of photons of specific wavelengths in the water column is a product of the underwater irradiance spectrum, which is modified by a number of components including the absorption of light by colored dissolved organism matter (A_{CDOM}), water (A_w), algal particles (A_{ph}), and detritus (A_d), as well as scattering by water and particulates (A_s).

CDOM absorbs strongly in the violet and blue regions of the visible spectrum, while A_{ph} and A_d vary dependent on their composition. While pure water absorbs strongly in the red end of PAR, there are shoulders in the spectrum of A_w formed by harmonics of stretching vibrations (Stomp et al., 2007).

Light attenuates exponentially across a given pathlength, and thus small local minima or maxima in the absorption spectrum of a water mass can have profound effects on the spectral quality of light with depth. Stomp et al. (2007) found that the vibrational modes of water in tandem with A_{CDOM} result in distinct spectral niches with depth, and that phytoplankton have evolved to tune their pigment composition to absorb maximally at wavelengths present in these spectral niches, with minimal absorption at wavelength that are rare at depth (Stomp et al., 2007). Recently, a study by Holtrop et al. (2020) improved upon the models of Stomp et al. (2007) and demonstrated that predicted global distributions of modeled spectral niches correlate to distributions of cyanobacteria with optimized pigmentations (Holtrop et al., 2020).

For our purposes of recreating distinct spectral niches in a lab setting, Ecosense®, an LED technology company delivering advanced LED systems primarily for architectural and commercial applications, developed a light engine capable of receiving input spectra and producing the closest spectral output at a tunable photon-flux by modulating the intensity of 6 independent LED color channels. In this study, an RB-TnSeq library of *S. elongatus* PCC 7942 (Rubin et al., 2015) was grown under an emulation of five spectral niches modeled in Holtrop et al. (2020) and a "white-light" full spectral control, and was sampled after five to six generations of growth to elucidate the genes important for fitness under these unique spectral niches. The spectral niches tested are representative of those described in Holtrop et al. (2020) as containing "extremely low", "low", "low-intermediate", "high", and "extremely high" CDOM

concentrations and are referred to in this chapter as “blue niche”, “cyan niche”, “green niche”, “orange niche”, and “red niche”, respectively.

Results

Generation of Spectral Niches

Using underwater scalar irradiance spectra generated for the 3% light level in Holtrop et al. (2020) as an input to the Ecosense® light-engine, six spectra were generated (**Figure 5.2.1**). All spectra were tuned to an irradiance of 200 µmol photons·m^{-2}·s^{-1} incident on the algal cultures.

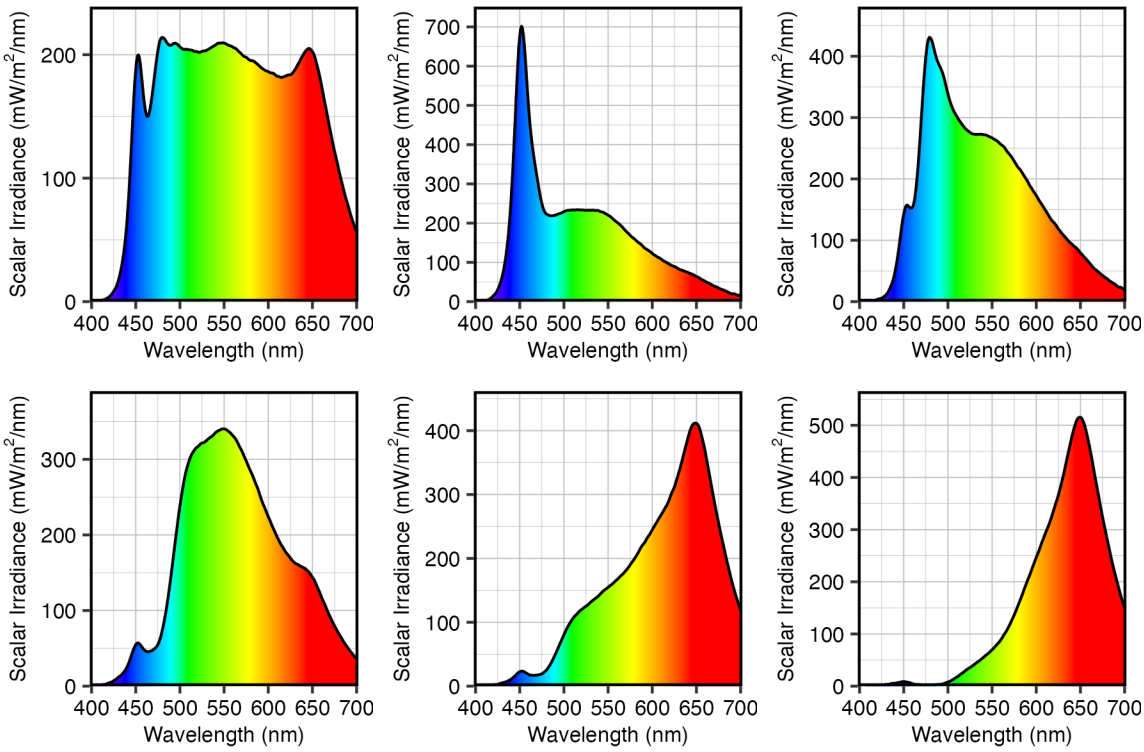

Figure 5.2.1. Representative spectra of the spectral niches generated by the Ecosense® light engine. From the upper left to bottom right panel: white light control, blue niche, cyan niche, green niche, orange niche, red niche.

RB-TnSeq Library Specific Growth Rates

The RB-TnSeq library had community-specific growth rates of less than 1.0 d^{-1} under all spectral niches (Table 5.2.1). The lowest growth rate was observed under the "green" / "low-intermediate CDOM" spectral niche (0.67 ± 0.02), while the fastest growth rates were observed under the initial white light control and "blue" / "extremely low CDOM" spectral niche (0.91 ± 0.01 and 0.92 ± 0.02, respectively. There is a discrepancy between the specific growth rates of the white-light control pre- and post-experimental spectral niches. It should be noted that these growth rates are not directly comparable to one another, as the disruption of genes that are important for specific spectral niches may be represented by larger portions of the population than other genes.

Table 5.2.1. Specific growth rates of RB-TnSeq library aliquots when grown under spectral niches.

Spectral Niche	Specific Growth Rate (d^{-1})
White Light 1 / Control 1	0.91 ± 0.01
"Blue" / "Extremely Low CDOM"	0.92 ± 0.02
"Cyan" / "Low CDOM"	0.81 ± 0.01
"Green" / "Low-intermediate CDOM"	0.67 ± 0.02
"Orange" / "High CDOM"	0.89 ± 0.02
"Red" / "Extremely High CDOM"	0.77 ± 0.01
White Light 2 / Control 2	0.79 ± 0.03

Gene Fitness Estimates for Spectral Niches

While all spectral niches yielded several genes with strong fitness values (i.e. disruption notably affected fitness) relative to the white-light control, there were several instances where the perceived fitness effect was due to poor performance of the mutant under the white light-control (**Figure 5.2.2**). Fitness in a spectral niche relative to the white-light control (ΔF) must therefore be interpreted with caution.

Figure 5.2.2. Scatter plot of fitness conferred by gene disruption relative to time 0 when grown in a spectral niche vs the white-light control. Point size indicates ΔF of gene. Solid lines delineate bounds for genes defined as conferring a strong a ΔF (less than -2 or greater than 2). All genes conferring a strong fitness under a spectral niche relative to the white light control are labelled.

All spectral niches other than "cyan" yielded a strongly negative change in fitness values (ΔF) relative to white light (ΔF < -2.0), while all spectral niches other than "green" yielded at least one gene with a strong increase in ΔF (ΔF > 2.0) (**Figure 5.2.3**).

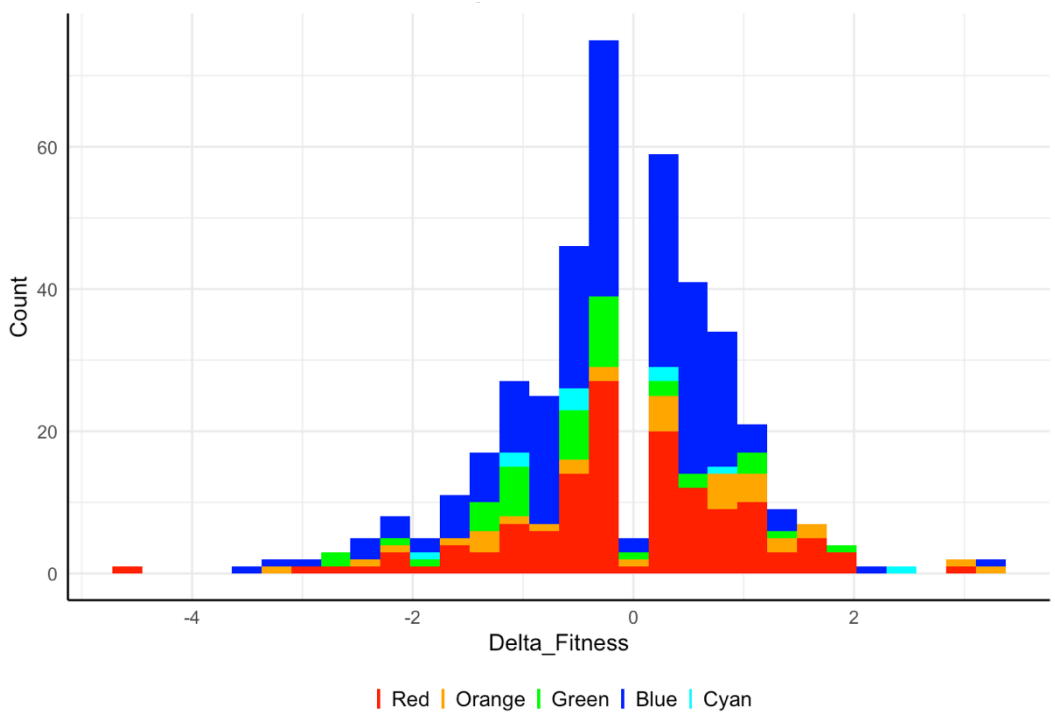

Figure 5.2.3. Histogram of ΔF values for the 5 spectral niche growth conditions.

Hierarchical clustering using Euclidean distance of ΔF values for genes in each spectral niche demonstrated a cluster of the "blue" and "cyan" spectral niches separated from an "orange", "green", and "red" spectral cluster, with the "green" spectral niche more closely related to "red" than "orange" (**Figure 5.2.4**).

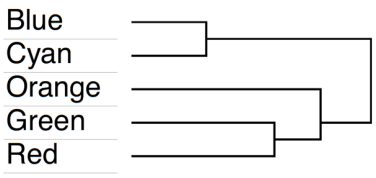

Figure 5.2.4. Hierarchical Euclidean distance clustering for spectral niches based on ΔF values for all genes with significant difference from the white light controls (P value > 0.05).

Functional Groupings of Genes

Genes with strong ΔF values were subsequently binned by a merged COG/CyoG database to identify relevant functional families (**Figure 5.2.5**). The majority of genes relevant to the "red" and "orange" spectral niches are either not in the COG/CyoG database or are classified as "function unknown" or "general function prediction only". Of the remaining genes important for fitness under the "red" niche, one gene is classified as being involved in "coenzyme transport and metabolism", one gene in "inorganic ion transport and metabolism", one gene in "replication, recombination, and repair", and one gene in "translation". Of the two remaining genes relevant to the "orange" niche, there is one involved in "coenzyme transport and metabolism", and one described as "NADH:plastoquinone oxioreductase". The only gene from the "cyan" niche to exhibit strong a strong fitness effect, *Synpcc7942_0675*, encoding a CCB1 domain-containing protein, is not in the COG/CyoG database. Only one gene from the eleven "blue" spectral niche genes that confer strong fitness affects is of an unknown function. The remaining ten genes are described as being involved in "cell wall/membrane biogenesis", "coenzyme transport and metabolism", "inorganic ion transport and metabolism", "lipid transport and metabolism", "NADH:plastoquinone oxioreductase", "transcription" and "translation".

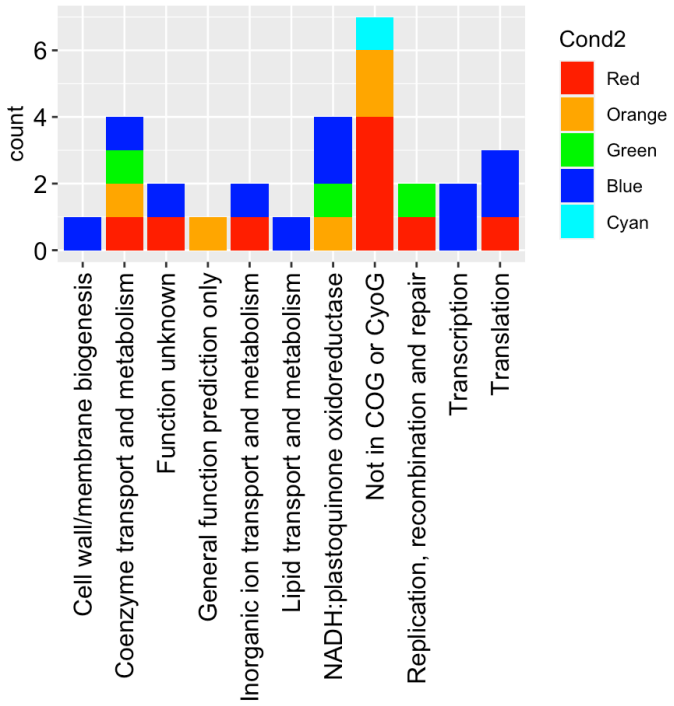

Figure 5.2.5. Histogram of COG/CyoG functional families for genes with ΔF values greater than 2.0 or less than -2.0.

Conservation of Fitness Conferred by Genes across Spectral Niches

To assess whether fitness changes conferred by gene disruptions are conserved across spectral niches, or unique to given spectral niche or subset of spectral niches, the list of all genes analyzed was curated to create a subset of only genes with a strong ΔF in at least one spectral niche (**Figure 5.2.6**). A total of twenty genes assigned to this subset. The disruption of one gene, *Synpcc7942_1184*, encoding a tetrahydropterin synthase, resulted in a strong decrease in fitness in all spectral niches aside from "cyan". Similarly, the disruption of *Synpcc7942_1570* and *Synpcc7942_1439* resulted in a moderate to strong decrease in fitness in four of the five spectral niches. The disruption of only one gene, *Synpcc7942_0675*, encoding a CCB1 domain-containing protein, resulted in a strong decrease in fitness under at least one spectral niche and a

strong increase in fitness under at least one other spectral niche. The disruption of the remaining genes results in a strong ΔF in either one or two unique spectral niches.

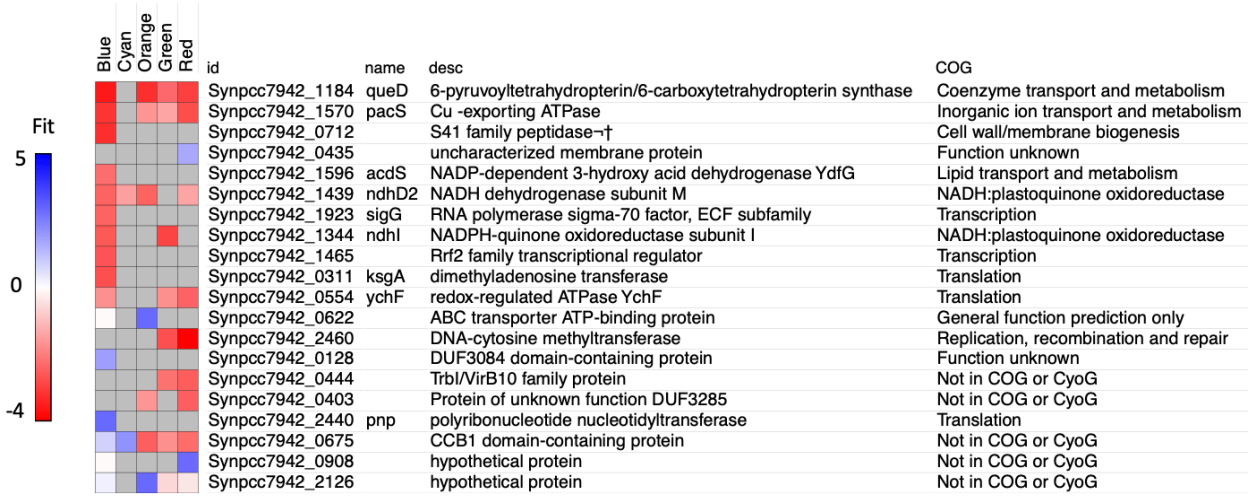

id	name	desc	COG
Synpcc7942_1184	queD	6-pyruvoyltetrahydropterin/6-carboxytetrahydropterin synthase	Coenzyme transport and metabolism
Synpcc7942_1570	pacS	Cu -exporting ATPase	Inorganic ion transport and metabolism
Synpcc7942_0712		S41 family peptidase¬†	Cell wall/membrane biogenesis
Synpcc7942_0435		uncharacterized membrane protein	Function unknown
Synpcc7942_1596	acdS	NADP-dependent 3-hydroxy acid dehydrogenase YdfG	Lipid transport and metabolism
Synpcc7942_1439	ndhD2	NADH dehydrogenase subunit M	NADH:plastoquinone oxidoreductase
Synpcc7942_1923	sigG	RNA polymerase sigma-70 factor, ECF subfamily	Transcription
Synpcc7942_1344	ndhI	NADPH-quinone oxidoreductase subunit I	NADH:plastoquinone oxidoreductase
Synpcc7942_1465		Rrf2 family transcriptional regulator	Transcription
Synpcc7942_0311	ksgA	dimethyladenosine transferase	Translation
Synpcc7942_0554	ychF	redox-regulated ATPase YchF	Translation
Synpcc7942_0622		ABC transporter ATP-binding protein	General function prediction only
Synpcc7942_2460		DNA-cytosine methyltransferase	Replication, recombination and repair
Synpcc7942_0128		DUF3084 domain-containing protein	Function unknown
Synpcc7942_0444		TrbI/VirB10 family protein	Not in COG or CyoG
Synpcc7942_0403		Protein of unknown function DUF3285	Not in COG or CyoG
Synpcc7942_2440	pnp	polyribonucleotide nucleotidyltransferase	Translation
Synpcc7942_0675		CCB1 domain-containing protein	Not in COG or CyoG
Synpcc7942_0908		hypothetical protein	Not in COG or CyoG
Synpcc7942_2126		hypothetical protein	Not in COG or CyoG

Figure 5.2.6. Heatmap of genes with a strong ΔF value (> 2.0 or < -2.0) in at least one spectral niche. Gray squares indicate fitness values that were not significantly different from the control.

Discussion

The results presented here represent the genes in *S. elongatus* PCC 7942 that confer strong changes in fitness under specific spectral signatures at a constant light intensity, relative to a white light control. Of the 2,723 genes in the *S. elongatus* 2.7 Mbp genome, 20 have a strong change in fitness when interrupted in a spectral niche relative to the white light control. It should be noted that 718 were previously determined to be essential (Rubin et al., 2015); thus, those mutants are absent from the library and were not sampled in this assay.

Spectral niches that are dominated by longer wavelength photons (i.e. the “red” / “extremely high CDOM” and “orange” / “high CDOM” niches) are more representative of spectral niches found in eutrophic lakes, while the “blue” / “extremely low CDOM” niches are representative of open ocean waters. The light level chosen for each spectral condition, 200 µmol

photons·m^{-2}·s^{-1}, is representative of roughly the 10% light level in the water column on a cloudless day. *Synechococcus elongatus* PCC 7942 was isolated from a shallow stream in the San Francisco Bay Area of California and has close relatives isolated from various other shallow streams, such as UTEX 3055 from Waller Creek, Texas (Yang et al., 2018b; Golden, 2019; Adomako et al., 2022). It is conceivable that *S. elongatus* has evolved in a spectral environment more similar to our control spectrum, that of sunlight incident on Earth's surface, thus the results of this study identify genes that are dispensable or important for a transition from a shallow stream to distinct spectral niches.

Of the genes identified in this study, only *Synpcc7942_0675*, encoding a CCB1 domain-containing protein, resulted in a strong decrease in fitness under 1 spectral niche and a strong increase in fitness under at least one other spectral niche. For this gene, the fitness of the mutant strains under the white light control was reduced (-1.69 +/- 0.20). The positive fitness of the mutant under the "cyan" condition (0.72 +/- 0.06) and negative fitness under "green", "orange", and "red" conditions suggests that either strong red light is detrimental to the mutant, or a high ratio of blue:red photons is necessary for viability. *Synpcc7942_0675* is conserved among both cyanobacteria and *Arabidopsis* (Kobayashi et al., 2004). Further studies should be conducted to investigate whether open ocean cyanobacteria ecotypes have streamlined genomes that exclude this gene, or reduced transcription of this gene relative to coastal ecotypes.

Another gene of interest is *Synpcc7942_1184*, whose interruption has a neutral fitness value in the white-light condition (0.10 +/- 0.11) and confers a strong decrease in fitness in all spectral niches aside from "cyan". *Synpcc7942_1184* encodes a 6-pyruvoyl-tetrahydropterin synthase-like protein, a key enzyme involved in tetrahydrobiopterin (BH_4) synthesis, which previously been implicated in UV-A tolerance (Matsunaga et al., 1993; Wachi et al., 1995) and

identified as a key gene for tolerating light-dark transitions (Rubin et al., 2018). As this is a 6-pyruvoyl-tetrahydropterin synthase-like protein, rather than a definitive tetrahydropterin synthase, it may have an alternative function, such as an involvement in transfer RNA biosynthesis, as predicted by the Kyoto Encyclopedia of Genes and Genomes (KEGG).

Two additional genes, *Synpcc7942_2460* and *Synpcc7942_2126* stand out as having a negligible fitness effects when disrupted under the white-light control, but a strong decrease or increase in relative fitness when disrupted under "red" or "orange" spectral niches, respectively. *Synpcc7942_2460* encodes a DNA-cytosine methyltransferase, which has been horizontally transferred to *S. elongatus* (Delaye et al., 2011), while *Synpcc7942_2126* encodes a hypothetical protein. There is little research on the impact of the spectral quality of light on DNA-methylation; however, in the brown cotton plant *Gossypium hirstum*, differing light qualities have diverse impacts on methylation patterns, with red light enhancing full methylation and hemi-methylation, while white and blue light decrease full methylation, suggesting an epigenetic mechanisms of response to light quality (Li et al., 2011). *Synpcc7942_2460* may fill a similar functional role in response to red light in *S. elongatus*.

The results of this study identify 20 genes worthy of follow-up experimentation to elucidate roles in fitness under unique spectral signatures. Further studies should involve deletion of the gene of interest and verification of phenotype when grown under the relevant spectral niche, followed by experimentation with monochromatic light to determine whether the phenotype is triggered by discrete wavelengths or a broader spectral signature. Metagenomic and metatranscriptomic studies of the distribution of the 20 genes that confer strong fitness changes would also aid in deciphering whether the results presented here are representative, in part, of a genetic basis for distributions of cyanobacterial ecotypes.

Materials and Methods

Construction of Light Engine and Generation of Spectral Niches

A custom light engine was fabricated by EcoSense ®, with four broadband phosphor converter LEDs (Korrus Inc.) of varying spectral quality spread evenly across a planar surface, driven by an EldoLED powerDrive device. Utilizing proprietary software integrated with the light engine, intensities of the varying LED bulbs were modulated to provide best fit in least squares sense output spectra based on input spectra.

Five spectral niches defined in Holtrop et al. (2020) as CDOM concentrations "extremely low", "low", "low-intermediate", "high", and "extremely high" were used as input spectra for the Ecosense® light-engine. The spectral outputs are referred to as "blue" niche, "cyan" niche, "green" niche, "orange" niche, and "red" niche, respectively, based on their appearance to the human eye. Irradiance levels incident on cultures for all spectral outputs were tuned to 200 μmol photons$\cdot m^{-2} \cdot s^{-1}$, as measured with a QSL-100 (Biospherical Instruments Inc.) quantum scale irradiance meter.

RB-TnSeq Library Specific Growth Rates

The growth rates of the RB-TnSeq library under each spectral niche condition were determined by monitoring the OD_{750} of the library at the time of initial exposure to the condition and after approximately five days of growth. The specific growth rate was calculated as $\mu = \ln(OD_{750, t2} / OD_{750, t1}) / (t_2 - t_1)$.

RB-TnSeq library sampling and sequencing

A one mL aliquot of an *S. elongatus* PCC 7942 RB-TnSeq library, previously archived at -80 °C, was quickly thawed for 2 min at 37 °C, resuspended in 2 flasks of 100 ml BG-11 with kanamycin (Km), and incubated at 30 °C for 1 day at 30 μmol photons·m^{-2}·s^{-1} without shaking (Rubin et al., 2015). The culture flasks were then transferred to 100 μmol photons·m^{-2}·s^{-1} on an orbital shaker. After one week of growth, four replicates of volume equivalent to 10 ml at OD_{750} = 0.3 were spun down at 4,500 x g and frozen at -80 °C as time 0 samples to determine the population baseline. Aliquots of the remaining culture were diluted to an OD_{750} of 0.03 and maintained in exponential phase for subsequent experimentation. 30 mL aliquots of the diluted culture were added to four polystyrene petri dishes and were placed adjacent to one another, oriented centrally underneath the Ecosense® light engine, and grown under 200 μmol photons·m^{-2}·s^{-1} of a spectral niche for five-six generations of growth. After five-six generations of growth, a volume equivalent to 10 mL at an OD_{750} of 0.3 (approximately 3 mL) of each of the four replicates was collected by centrifugation at 4,500 x g, and DNA was extracted from the pellet using a phenol-chloroform extraction (Clerico et al., 2007).

The process described above, from the time 0 sampling and dilution to growth under a spectral niche, sampling, and DNA extraction was repeated sequentially for each spectral niche. The “white light control” niche was grown and sampled twice, before and after all the other experimental spectral niche conditions.

BarSeq

The method for the quantification of TnSeq library barcodes, termed BarSeq analysis, was conducted as previously described (Wetmore, 2015). In brief, amplification of barcodes

from extracted DNA was conducted using 1 of 96 indexed forward primers for multiplexing, BarSeq_P2_ITXXX, and a common reverse primer, BarSeq_P1. PCR was performed in a final volume of 50 µl using Q5 DNA polymerase, Q5 GC Enhancer (New England Biolabs), and the following thermocycler conditions: (i) 98 °C for 4 min, (ii) 25 cycles of 30 s at 98 °C, 30 s at 55 °C, and 30 s at 72 °C, (iv) and a final extension at 72 °C for 5 min. 10 µl of each PCR product was then combined, purified with a DNA Clean and Concentrator Kit (Zymo Research), and quantified using a Nanodrop 2000 Spectrophotometer (Thermo Scientific). The pooled and purified product was then sequenced using Illumina HiSeq4000 SR75 by the IGM Genomics Center at the University of California San Diego.

RB-TnSeq data processing

BarSeq data were processed using R scripts previously described in Pierce et al. (2021). The scripts used and associated readme files are available at https://github.com/DuttonLab/RB-TnSeq-Microbial-interactions. In script 1, the reference genes chosen for normalization were ‘Synpcc7942_1445', 'Synpcc7942_0734', and 'Synpcc7942_1708', due to minimal changes in fitness as a result of disruption under all previously tested conditions. An assortment of alternate reference genes was tested to confirm the reference genes listed above conferred a minimal fitness effect when disrupted in the *psbAI* knockout. Comparisons associated with an adjusted *P* value lower than 5% were considered a significant interaction fitness (alphaF parameter = 0.002 and alphaT parameter = 0.05 in Script3_2conditions_FitnessComparison.Rmd code). To account for any drifts in the state of the inoculum that may affect experimental results over the course of the sequential experiments, script 3 was run twice, using as a control white-light spectrum samples collected prior to the spectral-niche conditions, and white-light spectrum

samples collected post spectral-niche conditions. Spectral-niche genes that had a *P* value greater than 0.05 in either comparison to the white-light controls were considered to be outside the threshold of significance.

5.3 IRB-Seq Highlights Genes Important for Survival in a *psbAI* Knockout

Introduction

Among the photosystem II (PSII) core photosynthesis proteins, the D1 subunit encoded by *psbA* endures the most damage due to the oxidative stress associated with water splitting (Mulo et al., 2009). As a result of this damage, there is a requirement for a high turnover rate of the D1 protein. Cyanobacteria contain between two and 11 copies of *psbA*, some of which encode unique isoforms of the protein (Sheridan et al., 2020). The replacement of the damaged D1 protein other isoforms that have different properties is one strategy to mitigate the damaging effects of high light and UVR stress (Vinyard et al., 2013). In *Synechococcus* PCC 7942, the *psbAI, psbAII*, and *psbAIII* members encode isoforms of the D1 protein that are differentially expressed by environmental cues. *psbAI* encodes the D1:1 isoform, and *psbAII & psbAIII* encode a D1:2 isoform. Under low light conditions, *psbAI* is actively transcribed, whereas *psbAII* and *psbAIII* are repressed, and reaction centers include D1:1 almost exclusively. In contrast, under high light, *psbaII* and *psbaIII* genes are transcribed and *psbAI* is inactivated, and thus the D1:2 isoform accumulates in PSII complexes (Schaefer and Golden, 1989). After acclimation to high light, *psbAI* is once again actively transcribed, and *psbAII* & *psbAIII* are repressed (Schaefer and Golden, 1989). The same transcriptional pattern of the D1 isoforms has been observed under 0.4 W m^{-2} of UV-B as well, while total levels of the D1 protein remained unchanged (Campbell et al., 1998). Under this UV-B condition, a double knockout of *psbAII* & *psbAIII* suffered severe

and sustained inhibition of photosystem II function, whereas a mutant strain with constitutive expression of *psbAII* and *psbAIII* was nearly resistant to UV-B, with no inhibition of photosystem II function (Campbell et al., 1998). It is therefore accepted that the exchange of D1 isoforms is largely responsible for cellular resistance to UV-B inhibition of photosystem II, in addition to resistance of oxidative stress induced by the visible spectrum (Tsinoremas et al., 1994; Vinyard et al., 2013).

Despite the importance of the regulation of the *psbA* genes, the signal transduction pathways involved have not been characterized. In this subchapter, we attempted to elucidate the genes responsible for the transition from *psbAI* to *psbAII* and *psbAIII*, using a high-throughput genetic interaction screen (IRB-Seq) involving the deletion of the *psbAI* gene, based on the premise that a *psbAI* knockout must activate *psbAII/III* expression for survival under conditions in which they normally are not expressed.

Results

To elucidate genes involved in the signal transduction pathway for transition from *psbAI* to *psbAII* and *psbAIII*, an RB-TnSeq library was transformed with a plasmid whose recombination with the chromosome causes the deletion of the *psbAI* gene. Transformants were plated on selective media, grown for six days, and resuspended and harvested for BarSeq analysis, as described in Materials and Methods. Of the 2005 non-essential genes in the *S. elongatus* PCC 7942 genome (Rubin et al., 2015), interruption of six genes strongly decreased fitness when disrupted (fitness estimate < -1.0) in combination with loss of *psbAI*, and 34 genes moderately decreased fitness (fitness estimate > -1.0 & < -0.05) (**Table 5.3.1**). Two of the mutants designated as conferring strong decreases in fitness, Synpcc7942_0425 and

Synpcc7942_0424, and one gene conferring a moderate decrease in fitness, Synpcc7942_0423, are the genes flanking *psbAI* and *psbAI* itself and their barcodes are lost during the transformation process. These 3 genes are not included in subsequent analysis and discussion. No genes strongly increased fitness when disrupted (fitness estimate > 1.0), and loss of six genes moderately increased fitness (fitness estimate > 0.05 & < 1.0) (**Table 5.3.2**).

Table 5.3.1 Genes resulting in a decrease in fitness when disrupted in a *psbAI* knockout, FDR threshold cutoff < 0.02. Genes disrupted during transformation for *psbAI* knockout are indicated with an *.

Locus ID	Name	Description	Estimate	STD Error	P-value	FDR
Synpcc7942_0425*	_0425	hypothetical protein	-1.54	0.40	0.00	0.00
Synpcc7942_1952	_1952	hypothetical protein	-1.34	0.41	0.00	0.01
Synpcc7942_1616	_1616	hypothetical protein	-1.21	0.38	0.00	0.02
Synpcc7942_1880	_1880	hypothetical protein	-1.07	0.28	0.00	0.00
Synpcc7942_2297	tal	transaldolase/EF-hand domain-containing protein	-1.01	0.10	0.00	0.00
Synpcc7942_0424*	psbAI	photosystem q(b) protein	-1.01	0.16	0.00	0.00
Synpcc7942_0423*	_0423	hypothetical protein	-0.93	0.28	0.00	0.01
Synpcc7942_2334	zwf	glucose-6-phosphate 1-dehydrogenase	-0.83	0.06	0.00	0.00
Synpcc7942_2273	_2273	hypothetical protein	-0.77	0.07	0.00	0.00
Synpcc7942_1033	_1033	hypothetical protein	-0.76	0.19	0.00	0.00
Synpcc7942_0810	_0810	hypothetical protein	-0.74	0.15	0.00	0.00
Synpcc7942_2479	_2479	pilin-like protein	-0.71	0.19	0.00	0.00
Synpcc7942_2464	_2464	N-acetylmannosamine-6-phosphate 2-epimerase	-0.65	0.10	0.00	0.00
Synpcc7942_1437	_1437	hypothetical protein	-0.64	0.19	0.00	0.01
Synpcc7942_1218	kaiA	circadian clock protein KaiA	-0.64	0.10	0.00	0.00
Synpcc7942_1234	_1234	hypothetical protein	-0.63	0.17	0.00	0.01
Synpcc7942_0529	pgl	6-phosphogluconolactonase	-0.61	0.12	0.00	0.00
Synpcc7942_1561	_1561	hypothetical protein	-0.60	0.20	0.00	0.02
Synpcc7942_1338	_1338	hypothetical protein	-0.59	0.14	0.00	0.00
Synpcc7942_1467	_1467	Heat shock protein DnaJ-like	-0.58	0.17	0.00	0.01
Synpcc7942_1281	_1281	hypothetical protein	-0.58	0.12	0.00	0.00
Synpcc7942_1247	_1247	hypothetical protein	-0.57	0.18	0.00	0.02
Synpcc7942_0244	glgP	Glycogen/starch/alpha-glucan phosphorylase	-0.57	0.06	0.00	0.00
Synpcc7942_1147	_1147	hypothetical protein	-0.56	0.12	0.00	0.00
Synpcc7942_B2660	B2660	hypothetical protein	-0.54	0.08	0.00	0.00

Table 5.3.2 Genes resulting in an increase in fitness when disrupted in a *psbAI* knockout, FDR threshold cutoff < 0.02.

Locus ID	Name	Description	Estimate	STD Error	P-value	FDR
Synpcc7942_2323	grxC	glutaredoxin	0.90	0.27	0.00	0.01
Synpcc7942_1174	psbJ	photosystem II reaction center protein PsbJ	0.73	0.20	0.00	0.01
Synpcc7942_1809	flv1	flavoprotein	0.62	0.06	0.00	0.00
Synpcc7942_0709	_0709	hypothetical protein	0.53	0.17	0.00	0.02
Synpcc7942_1185	_1185	hypothetical protein	0.53	0.17	0.00	0.02
Synpcc7942_0162	_0162	hypothetical protein	0.52	0.12	0.00	0.00
Synpcc7942_1088	petE	plastocyanin	0.49	0.16	0.00	0.02
Synpcc7942_1989	_1989	cation diffusion facilitator family transporter	0.44	0.14	0.00	0.02
Synpcc7942_1810	flv3	flavoprotein	0.44	0.07	0.00	0.00
Synpcc7942_0556	srrB	two component transcriptional regulator	0.44	0.13	0.00	0.01

The genes conferring strong decreases in fitness when disrupted encode three hypothetical proteins (*Synpcc7942_1952*, *Synpcc7942_1616*, and *Synpcc7942_1880*) and a transaldolase (*tal, Synpcc7942_2297*). The 34 genes conferring moderate decreases in fitness when disrupted encode of 12 hypothetical proteins, as well as a glucose-6-phosphate 1-dehydrogenase (*Synpcc7942_2334, zwf)*, a pilin-like protein (*Synpcc7942_2479*), a N-acetylmannosamine-6-phosphate 2-epimerase (*Synpcc7942_2464*), circadian clock protein KaiA (*Synpcc7942_1218, kaiA*), a 6-phosphogluconolactonase (*Synpcc7942_0529, pgl*), a DnaJ-like heat shock protein (*Synpcc7942_1467*), and a glycogen/starch/alpha-glucan phosphorylase (*Synpcc7942_0244, glgP*).

The genes conferring a moderate increase in fitness when disrupted encode glutaredoxin (*Synpcc7942_2323, grxC*), photosystem II reaction center protein J (*Synpcc7942_1174, psbJ*), a flavoprotein (*Synpcc7942_1809, flv1*), and 3 hypothetical proteins (*Synpcc7942_0709, Synpcc7942_1185,* and *Synpcc7942_0162*).

Discussion

The results presented here identify genes that affect fitness in *psbAI* knockout mutants of *S. elongatus.* We expected that, within the set of genes identified, at least one would be clearly involved in a signal transduction pathway. While the results do not explicitly eliminate this possibility, there is no clear evidence of any genes involved in signal transduction.

There are several hypotheses as to why the outcome of this screen did not elucidate the expected results. Firstly, the RB-TnSeq library is by definition composed of the non-essential gene-set. If genes critical for the regulation of the transition from *psbAI* to *psbaII/III* happen to be essential for survival under normal lab conditions, they would be overlooked by this screen. This issue could be overcome by constructing a CRISPR-dCas9 knockdown library of *S. elongatus*, which would include essential genes, paired with a transformation for a *psbAI* knockout. Secondly, there is the possibility that there is no canonical genetic signaling mechanism for the transition. Perhaps there is an alternative method of regulation, such as the binding of damaged D1 proteins to DNA, resulting in the D1 protein regulating its own synthesis (Stelljes and Koenig, 2007). Thirdly, it is possible that the gene of interest is under the guise of encoding a hypothetical protein. Subsequent experiments with individual knockouts of the genes of interest will be needed to understand the mechanism by which these hypothetical genes affect fitness of *psbAI* knockouts.

Synpcc7942_1952 encodes a hypothetical 133 amino acid polypeptide and shows moderate co-fitness with several genes shown to be important for fitness under UVR stress in chapter 2, such as *uvrC* and *gshB*, indicating that this gene may be part of an overall response to oxidative stress. *Synpcc7942_1616* encodes a 128 amino acid polypeptide and is cotranscribed with *Synpcc7942_1613- Synpcc7942_1615* (hypothetical protein, *rpmH*, and *rnpA*).

Interestingly, *Synpcc7942_1616* was also identified as important for fitness under UVR stress, which was suggested in chapter 2 to have an important role in association to photosystem complexes, as the protein product has been detected in PSI and PSII pulldown experiments (Zhang et al., 2021). Lastly, *Synpcc7942_1880* is transcribed alone, encodes a 68 amino acid polypeptid, and has no strong co-fitness with other genes. In addition to the genes that encode for hypothetical proteins and result in strong decreases in fitness when disrupted, several genes involved in carbon metabolism were identified as conferring strong to moderate fitness defects. These genes include *tal, zwf, glgX, glgP, and opcA*. With the exception of *glgP*, these 5 genes are all involved in the oxidative pentose phosphate pathway (OPPP). These members of the OPPP are critical for survival through darkness, with gene expression peaking at dawn (Diamond et al., 2015; Welkie et al., 2018).

Of the six genes that confer a strong increase in fitness when disrupted, three encode hypothetical proteins. The other three genes encode a glutaredoxin, flavoprotein 1 (Flv1), and PsbJ. Glutaredoxins are involved in the maintenance of cellular redox potential and iron-sulfur homeostasis. Flavoprotein 1 (a component of the heterodimer Flv1/Flv3) functions as a NAD(P)H:oxygen oxidoreductase, donating electrons directly to O_2 without the production of reactive oxygen species. Flavoproteins are important for cyanobacteria under fluctuating light, as mutants exhibit malfunction of photosystem I and suffer oxidative damage induced by the formation of ROS generated during abrupt short-term increases in light (Allahverdiyeva et al., 2013). Essentially, the Flv1/Flv3 heterodimer assists in maintaining the redox balance of the electron transfer chain in cyanobacteria (Shaku et al., 2016). *Flv1* was previously implicated as the gene with the greatest decrease in fitness in a *cdaA* IRB-Seq experiment (Rubin et al., 2018). Lastly, *psbJ* has been shown to regulate the number of photosystem II centers in thylakoid

membranes in *Synechocystis* sp. PCC 6803 (Lind et al., 1993). Interestingly, *psbJ* mutants exhibited a moderate decrease in fitness in the UVR screen described in Chapter 2 as well. Cultures of the *psbJ* mutants grown for experimentation in Chapter 2 had a blue phenotype, suggesting a change in the ratio of chlorophyll to phycobiliproteins.

Materials and Methods

Construction of plasmids and mutants

Plasmid pPSBAI-KO for the deletion of the *psbAI* gene from *S. elongatus* was created by first digesting pAM4817 with EcoRV (NEB) and pAM4843 with ZraI (NEB). PCRs for 700 nucleotide left and right recombination arms surrounding *psbAI* were created by amplifying wild-type gDNA with primer pairs 5'CGCTATCGCTACGTGACTGGGTCATGGCTGGTCCAGTCGTGGTTTCCAGT3' & 5'GAACGAGCGCAAGGTTTCGGTCTCCACGACATCGATCTTGAGGTTGTAAAGGG3' and 5'GCATTAACATGGTCATAGCTGTTTCCTTGCTTGCCGGAATTACAGCAGTCT3' & 5'GATGCCGCATAGTTAAGCCAGCCCCGACACGCATGAACTTAGAAGCCCTGATTC3' for the left and right arms, respectively, using standard protocols. The pPSBAI-KO plasmid was then generated via seamless assembly using a GeneArt® Seamless Cloning and Assembly Kit (Thermo Fisher Scientific) with the four components. The plasmid pAM5610, containing a gentamycin resistance cassette flanked by arms for recombination into a *S. elongatus* neutral site, was used for the control strain. Transformation of *S. elongatus* was achieved using standard protocols (Clerico et al., 2007). Genotyping of *S. elongatus* was performed using colony PCR with Taq DNA Polymerase (NEB).

Estimation of transformation efficiency

To estimate the transformation efficiencies of pPSBAI-KO and pAM5610 prior to creating the *psbAI* IRB-Seq library, large aliquots of the plasmid pPSBAI-KO and pAM5610 were prepared using a DNA/RNA MiniPrep Kit Plus (Zymo Research), following the manufacturer's protocol. A stock of the RB-TnSeq library left to grow on a laboratory bench following the experiments in Chapter 2 was grown to an OD_{750} of 0.4 under 70 μmol photons·m^{-2}·s^{-1} of constant light and orbital shaking. The cells were then transformed using standard protocols (Clerico et al., 2007), beginning with 19.5 mL of culture which was split into six 200 μL aliquots following the cleaning and concentration steps. Three aliquots were each supplemented with 500 ng of pPSBAI-KO, and three with 500 ng of pAM5610. After 4 hours of incubation, the aliquots were serial diluted and plated in 6 μL spots on BG-11 plates with the addition of either kanamycin (Km) or kanamycin/gentamycin (KmGm). The transformation efficiency was calculated as the ratio between colonies appearing on the Km and KmGm plates. A transformation efficiency of 0.0015 was calculated for pAM5610 and 0.0042 for pPSBAI-KO.

PsbAI IRB-Seq library creation and sampling

To create the IRB-Seq library, an aliquot of a previously created RB-TnSeq library was rapidly thawed as previously described (Rubin et al., 2015). After growing to an OD_{750} of approximately 0.4, four 10 mL samples were taken, spun, and frozen as T0 samples. The library was then transformed with either pPSBAI-KO or pAM5610, using culture volumes and plasmid concentrations established during the transformation efficiency tests to achieve approximately $5*10^5$ mutants in order to maintain the diversity of the $1.52*10^5$-member library. Following a 4-hour incubation, the control library and *psbaI* library were plated on Km/Gm plates and left to

grow under 140 μmol photons·m^{-2}·s^{-1}.

After 6 days of growth, colonies were harvested from their plates using 2 ml of BG-11 with KmGm added, and a cell spreader to aid in resuspension. Samples were washed twice by centrifugation and resuspended in media. From each of the six tubes, two replicates were taken and frozen at -80°C for BarSeq analysis. Extra resuspension was used to inoculate flasks of 100ml BG-11 + KmGm, which were subsequently concentrated and cryopreserved for posterity. Future studies using the *psbAI*-IRB-Seq library should thaw and resuspend frozen aliquots following the protocols described in Rubin et al. (2015). Samples taken as T0s should be compared with the BarSeq data available from this study, to assess diversity loss due to the freeze/thaw process.

BarSeq and Fitness calculations

The method for BarSeq analysis was conducted as previously described (Wetmore et al., 2015). In brief, amplification of barcodes from extracted DNA was conducted using one of 96 indexed forward primers for multiplexing, BarSeq_P2_ITXXX, and a common reverse primer, BarSeq_P1. PCR was performed in a final volumes of 50 μL using Q5 DNA polymerase, Q5 GC Enhancer (New England Biolabs), and the following thermocycler conditions: (i) 98 °C for 4 min, (ii) 25 cycles of 30 s at 98 °C, 30 s at 55 °C, and 30 s at 72 °C, (iv) and a final extension at 72 °C for 5 min. 10 μl of each PCR product was then combined, purified with a DNA Clean & Concentrator Kit (Zymo Research), and quantified using a Nanodrop 2000 Spectrophotometer (Thermo Scientific). The pooled and purified product was then sequenced using Illumina HiSeq4000 SR75 by the IGM Genomics Center at the University of California San Diego.

Fitness values were calculated using a previously described R script, using a FDR cutoff threshold of 0.02 (Rubin et al., 2018).

5.4 Heterologous Expression of MAA Biosynthetic Gene Clusters in *E. coli*

Introduction

While MAAs are seemingly ubiquitous in the world's oceans, and common in both terrestrial and freshwater alpine environments, we still have limited knowledge of the genetic basis behind the diversity of the 40+ MAAs currently identified in nature. As described in chapter 3, there are correlations between specific MAAs and taxa of phytoplankton, as well as changes in the ratio of MAAs:Chl*a* in phytoplankton in response to changes in UVR levels. MAAs may serve as a bioindicators of UVR-stress and help to improve satellite ocean color algorithms. An enhanced understanding of the genetic underpinnings of this diversity may prove highly informative in the current era of big data, as metagenomic and transcriptomic datasets could be mined for such pathways to elucidate global distributions of MAAs and the regulation of MAAs in the context of a changing climate.

Our understanding of the genetic basis of MAA synthesis has been gaining momentum over the past decade. Fundamentally, in cyanobacteria MAAs are synthesized via a 3+ component gene cluster (Balskus and Walsh, 2010). In *Anabaena variabilis* ATCC 29413 the pentose phosphate pathway intermediate sedoheptulose 7-phosphate (SH 7-P) is modified by a dehydroquinate synthase homolog (DHQS) 2-epi-5-epi-valionate synthase (EVS) and an adjacent O-methyltransferase (O-MT) to form a single product, 4-deoxygadusol. 4-deoxygadusol and glycine are then converted by an ATP-grasp family member to form mycosporine-glycine, the basal mycosporine that absorbs maximally at ~310 nm, which is thought to be the core

molecule from which other MAAs are derived. A non-ribosomal peptide synthase (NRPS)-like enzyme, containing adenylation, thiolation, and thioesterase domains, converts mycosporine glycine and serine to shinorine, a common MAA that absorbs maximally at approximately 334 nm. In addition to the discovery of the genetic basis of MAA biosynthesis in cyanobacteria, research by Dr. Yang at the University of Florida has been successful in the heterologous production of mycosporine-glycine using the MAA biosynthetic gene cluster from *Fischerella* sp. PCC 9339 in *Synechocystis* sp. PCC 6803 (Yang et al., 2018a).

In addition to the fundamental necessity of understanding the biology and ecology of these molecules, MAAs show great biotechnological promise as next-generation sunscreen compounds. Recent studies have demonstrated that some of the chemical compounds present in commercial sunscreens, such as benzophenone-3, can have toxic effects on corals (Danovaro et al., 2008). It is estimated that between 6,000 and 14,000 tons of sunscreen lotion, many containing up to 10% benzophenone-3, are released into coral reef environments annually (Downs et al., 2006). In 2018, Hawaii was the first US state to ban the sale of sunscreens containing oxybenzone and octinoxate, galvanizing a new focus on sunscreen alternatives. While a few companies, such as Mibelle Biochemistry in Switzerland, have adopted MAAs as UV-screening additives to their cosmetic products, the algal strain used for MAA production, *Porphyra umbilicalis*, is relatively slow growing, and the MAAs produced only cover a limited bandwidth of the UV spectrum. Thus, the heterologous expression of a diversity of MAAs will be a useful organic sunscreen alternative for many current commercial sunscreens.

In this study we used bioinformatics to predict which isolates of cyanobacteria, available in the Gerwick laboratory at Scripps Institution of Oceanography, are capable of expressing MAAs, profile the MAAs produced after induction by UVR, and attempted to express the MAAs

in *E. coli* to expand on the diversity of MAAs available for high yield expression for downstream biotechnological applications.

Results

Prediction of MAA-containing cyanobacteria strains and growth phenotypes

The cyanobacterial library of genetic data in the Gerwick Lab at SIO (in collaboration with the Knight Lab, at UCSD) consists of 210 metagenomic assemblies and 75 assembled genomes. We identified several MAA-like genes; however, they were numerous and sometimes not clustered in BGCs. In order to narrow the list of candidates, the gene cluster networking tool BiG-SCAPE was used to group the BGCs into families. A family containing 119 candidate MAA BGCs was identified; however, only a few of those strains have been successfully established and maintained in laboratory cultures. Three strains maintained in laboratory cultures were selected for further screening for the presence of MAAs (**Table 5.4.1**).

Table 5.4.1. Strains from the Gerwick laboratory at the Scripps Institution of Oceanography predicted to synthesize MAAs.

Field ID	Genome ID	Mash ID	Collection Site	Species Name
PAL24MAY134CUL	1D4	Moorea	Palmyra Atoll	Moorea sp.
3LOscillatoriaCUL	4C8	Moorea	Curacao	Oscillatoria nigrovidis
JHBCUL	4C7	Moorea	Jamaica	Moorea producens

The three cultures were exposed to UVR and visible light on a 16-h light:8-h dark cycle for 22 days. There were no visible signs of growth during this period; however, within 48 hours of UVR exposure, *Oscillatoria nigrovidis* folded into a compact ball, potentially as a stress response, and likely conferring self-shading to the community (**Figure 5.4.1**).

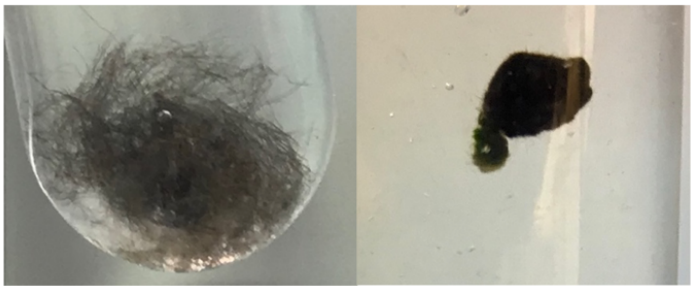

Figure 5.4.1. Compaction of *Oscillatoria nigrovidis* after UV exposure.

MAA profile of UVR induced cultures

All three of the cyanobacterial strains cultivated under UVR for 22 days produced MAAs. *Oscillatoria nigrovidis* (3LOscillatoriaCUL) produced 2 MAAs, eluting at 5.561 min (a_{max} 332 nm), and 10.495 min (a_{max} 330 nm), with *m/z* = 333.14 and 289.21, respectively (**Figure 5.4.2**). Based on retention time, absorption spectra, and *m/z*, these compounds have been defined as shinorine and asterina-330. While the BGC for the biosynthesis of shinorine has been elucidated and proven to be widely conserved in cyanobacteria, the pathway for asterina-330 production has not.

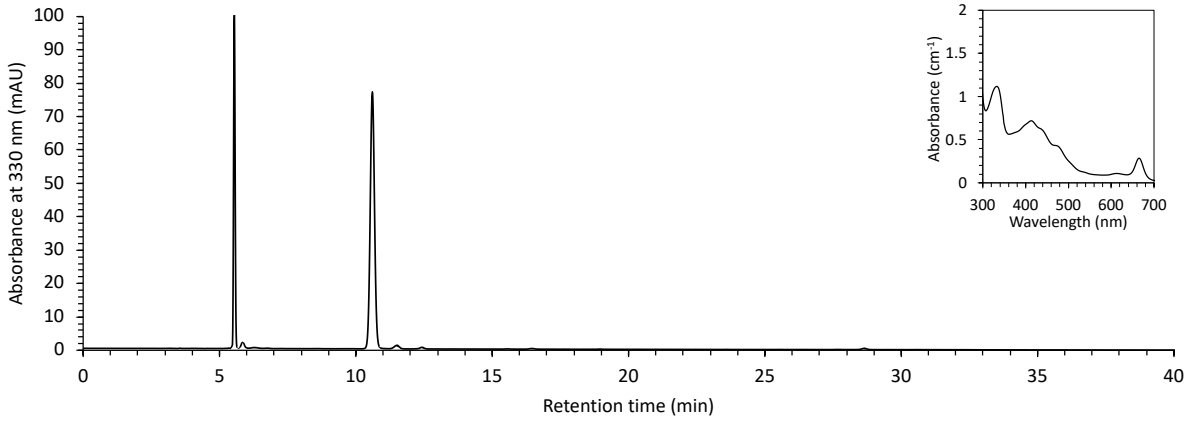

Figure 5.4.2. HPLC chromatogram of MAAs present in *Oscillatoria nigrovidis* after prolonged exposure to UVR. The absorbance spectrum of the methanol extract is inset in the upper right panel.

Moorea producens (JHBCUL) produced two MAAs as well, eluting at 5.082 min (a_{max} 332 nm), and 11.708 min (a_{max} 308 nm), with *m/z* = 333.14 and 246.13, respectively (**Figure 5.4.3**). Based on retention time, absorption spectra, and *m/z*, these compounds have been tentatively defined as shinorine and mycosporine-glycine. The BGC for production of both shinorine and mycosporine-glycine have been elucidated, heterologously expressed, and proven to be widely conserved in cyanobacteria. Based on the absorption spectrum (**Figure 5.4.3**), the ratio of MAAs:Chl*a* appear to be extremely high, making this strain a compelling candidate for future studies on MAA regulation.

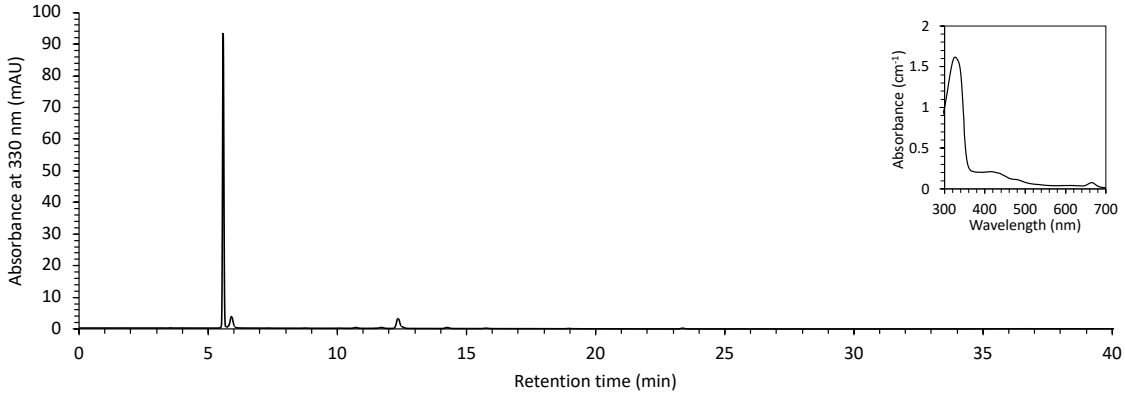

Figure 5.4.3. HPLC chromatogram of MAAs present in *Moorea producens* after prolonged exposure to UVR. The absorbance spectrum of the methanol extract is inset in the upper right panel.

Moorea sp. (PAL24MAY134CUL) extract contained the greatest diversity of MAAs with 5 putative MAA compounds, eluting at 14.17 min (a_{max} 330 nm), 18.97 min (a_{max} 310 nm), 20.60 min (a_{max} 320 nm), 28.62 min (a_{max} 358 nm), and 36.35 min (a_{max} 312 nm) (**Figure 5.4.4**). Interestingly, the canonical MAA precursor compound mycosporine-glycine and the common secondary MAA shinorine were not present in the extract, although the genes present in the putative MAA BGC contain homology to the enzymes required for synthesis.

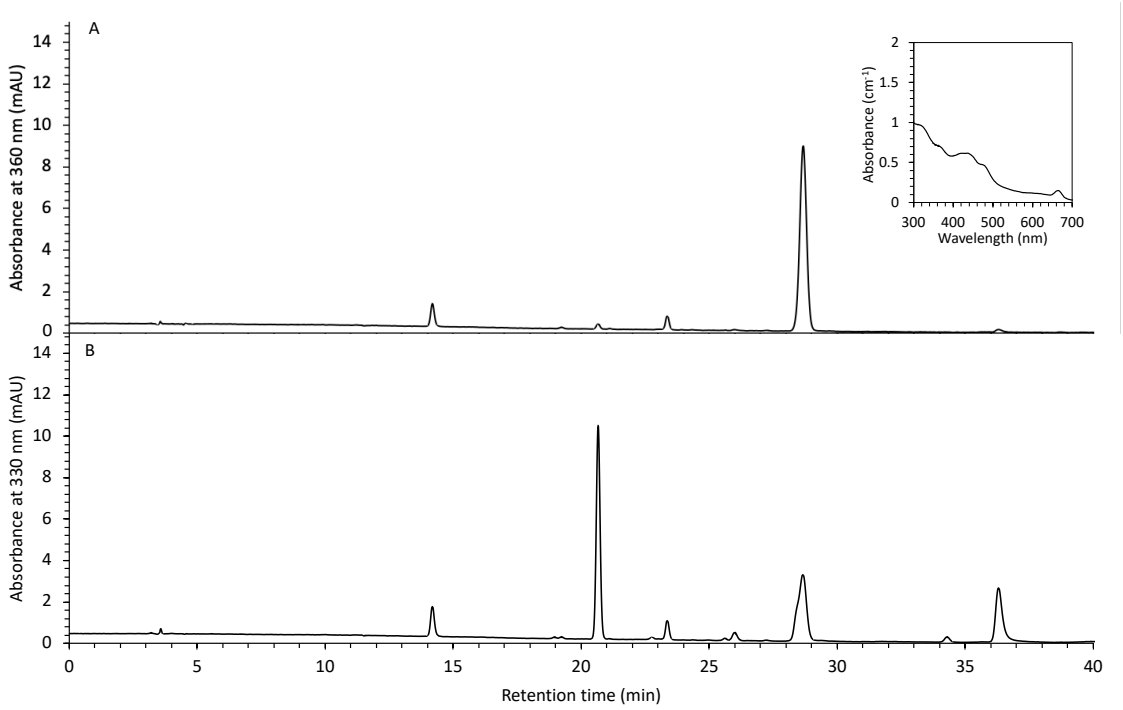

Figure 5.4.4. HPLC chromatogram of MAAs present in *Moorea sp*. after prolonged exposure to UVR. A) Absorbance at 360 nm. B) Absorbance at 330 nm. The absorbance spectrum of the methanol extract is inset in the upper right panel.

Heterologous expression of MAAs in E. coli

The putative MAA producing BGCs from the three profiled strains were cloned into *E. coli* BL21(DE3) for inducible overexpression. The *Moorea producens* JHB BGC yielded two MAAs in *E. coli*, identified as shinorine and mycosporine-glycine, a profile identical to the wildtype JHB strain. Neither the *Moorea sp*. nor the *Oscillatoria nigrovidis* BGCs produced MAAs in *E. coli*.

Discussion

The results presented here illustrate the MAA profiles of three cyanobacterial strains successfully predicted to produced MAAs using previously identified genes involved in the synthesis of the MAAs mycosporine-glycine and shinorine. Of these three strains, only *Moorea sp*. PAL (PAL24MAY134CUL) produced potentially novel MAAs.

Heterologous expression of MAAs using the *Moorea producens* (JHB) gene cluster in *E. coli* was successful; however, the MAAs produced, mycosporine-glycine and shinorine, have previously been expressed heterologously (Yang et al., 2018a). Heterologous expression of MAAs from the BGCs of *Oscillatoria nigrovidis* and *Moorea* sp. PAL were unsuccessful. This failure is is likely due to either a false prediction of the MAA BGC, a lack of necessary co-factors for synthesis in *E. coli*, or poor levels of transcription due to the reliance of a single promoter upstream of a large gene cluster.

The BGC of *Moorea* sp. PAL was identified by AntiSMASH through homology to the shinorine BGC of *Anabaena variabilis* ATCC 29413, which synthesizes both mycosporine-glycine and shinorine. However, neither of these compounds was present in the methanol extract. These molecules may be absent because the molecules are precursors for the other five MAAs detected and are converted to undetectable levels by other enzymes encoded in the BGC or elsewhere in the genome. Alternatively, the genes identified may produce entirely different MAAs, with the potential for enzymes encoded downstream in the BGC to further modify these precursor MAAs. Unfortunately, heterologous expression of the putative MAA BGC in *E. coli* did not successfully produce MAAs. Future studies should attempt to express the putative MAA BGC in other cyanobacteria capable of synthesizing simple MAAs to overcome co-factor limitations, such as *Anabaena* sp. PCC 7120, or fragment the BGC and engineer strong

promoters upstream of each gene to enhance transcription of each genetic component. Both strategies have proven successful for the production of recombinant cyanobacterial proteins (Taton et al., 2020, 2022). Due to the diversity of MAAs present in the methanolic extract of *Moorea sp*. PAL, the potential novelty of these MAAs, and the biotechnological utility of sunscreen compounds absorbing across a wide spectral bandwidth (absorption maxima ranging from 310 to 358 nm), further studies are warranted with this strain.

Materials and Methods

Prediction of MAA-Containing Cyanobacteria Strains

To identify putative MAA biosynthetic gene clusters in the Gerwick cyanobacteria collection available at the Scripps Institution of Oceanography, antiSMASH was used to annotate all biosynthetic genes clusters from available strains, from which a BLAST database was created. The genes Ava_3858, Ava_3857, and Ava_3856, from the *A. variabilis* ATCC 29413 core MAA pathway, were queried against this database. From the resultant hits, only strains successfully maintained in laboratory cultures were selected for further screening of the presence of MAAs.

Induction of Putative MAAs

All strains were sub-cultured in SWBG11 media in autoclaved quartz tubes and grown at 27.3 °C with no CO_2 added or stirring, in front of a Q-Lab UV-A 340 lamp (270 lux) and a 'whole-spectrum' lamp (1700 lux) on a 16:8 light/dark cycle. The samples incubated under these conditions for 22 days, filtered for the collection of residual biomass, and frozen in liquid

nitrogen.

Analysis of MAAs

MAAs were extracted and analyzed according to the HPLC method of Carreto et al. (2005). In brief, each frozen sample was extracted sequentially (x3) in 2ml of 80% methanol and sonicated on ice (30 s total, 10 s on, 5 s off). Extracts were centrifuged and pooled to remove filter debris, and the supernatant was evaporated using a Labconco Centrivap Concentrator at 30°C. Samples were resuspended in 0.5 mL of HPLC grade H_2O and filtered through Pall Nanosep 100k Omega centrifugal filters prior to analysis. Samples were analyzed using the reverse C18 columns and the gradient elution described in Carreto et al. (2005). MAA identities were confirmed for dominant MAAs using retention times, UV-visible spectra, and LC-MS analysis at 50x dilution and SPE column filtration. MAAs were quantified by HPLC using response factors (ng/HPLC peak area) from secondary standards, when available.

Heterologous Expression of Gene Clusters

To create a plasmid for the heterologous expression of the MAAs, two primers (pet28-linear-streptag-F and pet28-linear-streptag-R; **Table 5.4.2**) were used with PCR to linearize a commercially available pET-28b(+) vector (Millipore Sigma) and incorporate sequence to encode a Strep-tag on the N-terminus of the protein product. The primer pair JHB-F & JHB-R was used to amplify the putative *Moorea producens* (JHB) MAA BGC with appropriate overhangs for subsequent Gibson Assembly with the linearized pET-28b(+) vector (NEB). The primer pair PAL-F & PAL-R was used to amplify the putative *Moorea sp.* PAL MAA BGC with appropriate overhangs for subsequent Gibson Assembly with the linearized pET-28b(+) vector (NEB). The primer pair OSC-F & OSC-R was used to amplify the putative *Moorea sp.* PAL

MAA BGC with appropriate overhangs for subsequent Gibson Assembly with the linearized pET-28b(+) vector (NEB).

Table 5.4.2 Primers used in this study.

Primer Name	Sequence
pet28-linear-streptag-F	AGCTCCGTCGACAAGCTTG
pet28-linear-streptag-R	CTGCGGGTGGCTCCATTCCATGGTATATCTCCTTCTTAAAGTTAAAC
JHB-F	CATGGAATGGAGCCACCCGCAGTTCGAAAAGTCGGCCGTTCAAGCTAAACCTAATCC
JHB-R	GCAAGCTTGTCGACGGAGCTCAGTATAAATGCAAAAGTAGCTGTCA
PAL-F	TAAGAAGGAGATATACCATGACTTTGGTAGACCGCAGTTTCTTC
PAL-R	TGTTAGCAGCCGGATCTCAGTATCGGAAATTAGCTGTGCTTATTGG
OSC-F	TAAGAAGGAGATATACCATGAGCAACGCAATATTTCCTTCTAC
OSC-R	TGTTAGCAGCCGGATCTCAGTACTCCCTACTCCCTACTCCCTTT

The resulting plasmids were used to transform *E. coli* DH5α cells for plasmid generation and sequence confirmation. The plasmid was subsequently moved into *E. coli* BL21 (DE3). Plasmid-bearing *E. coli* BL21 (DE3) strains were grown to OD_{600} of 0.5 with 50 mg/mL kanamycin before overnight induction of protein expression at room temperature by the addition of 200 μM isopropyl β-D-1-thiogalactopyranoside and subsequent collection for MAA analysis.

Acknowledgments

Chapter 5 consists of unpublished material. The dissertation author was the primary author of this material. The following individuals are also authors on this work: Section 5.2- Susan Golden (UCSD), Ben Harrison (Ecosense); Section 5.3- Susan Golden (UCSD); Section 5.4- Tiago Ferreira-leão (UCSD), Evgenia Glukhov (UCSD), Lena Gerwick (UCSD).

CHAPTER 6: Conclusions

The chapters presented in this dissertation examine both the genetic and environmental basis of interactions between phytoplankton and light. While each studies focuses on one of these components at a time, as a sum, this thesis threads a narrative through each, culminating in the biotechnological application of an engineered photosynthetic living material.

Using a combination of the high-throughput genetic screening technique RB-TnSeq, transcriptomics, biochemical assays, and discrete growth experiments, in chapter 2 we have identified a gene important for UVR tolerance that was previously overlooked, a leucyl aminopeptidase (LAP), with cysteinyl-glycinase properties. The LAP is conserved across many ecologically relevant species and may be a key component of the glutathione catabolism pathway, with a pH-dependence that modulates activity of the enzyme based on the photosynthetic activity of the cell. The LAP identified by this screen has likely been overlooked due to low transcript levels in response to acute UVR exposure, highlighting the importance of utilizing new methods to investigate age-old concepts. Future genomic studies on the genetic basis of UV-tolerance in phytoplankton will benefit from the use of methodologies such as CRISPRi knockdown libraries, to elucidate the importance of essential genes that are necessary for survival under standard laboratory conditions and that are overlooked by RB-TnSeq.

In contrast, chapter 3 relies on more traditional methods of oceanic sampling and taxa analysis by proxy of pigmentation. The data presented in chapter 3 incrementally close the gap in knowledge of the global distribution of MAAs, and identify correlations between phytoplankton taxa and MAA quality, as well as UVR light history and the ratio of MAAs to Chl*a*. Future studies of the distribution of MAAs should include more modern methods of sampling and

analysis, including metagenomics and metatranscriptomics to gain higher taxonomic resolution of the bacteria and protists corresponding with MAAs at discrete sampling sites.

The ELMs developed in chapter 4 bridge the gap between biologists and materials scientists, utilizing synthetic biology toolkits to create stimuli-responsive photosynthetic materials with functional outputs. The specific ELM designed as a proof-of-concept for bioremediation in the studies presented here only begins to scratch the surface of the potential for materials embedded with photosynthetic organisms. Future iterations could include cyanobacterial strains tailored for enhanced carbon capture and printed within a 3D structure for optimal surface area to volume ratios, and novel secretion systems could be utilized to enhance the activity of enzymes of interest in the surrounding environment. Various polymers with properties of interest, such as temperature-dependent conformational changes, could be used as a scaffold for cells and RB-TnSeq experiments could be conducted to elucidate genes that are important for growth within such polymer matrices to create more robust ELMs of greater dimensionality.

In summary, this thesis explores the mechanisms that have evolved in phytoplankton to enable them to tolerate distinct spectral signatures of light and takes our understanding of these mechanisms to explore how humankind can utilize phytoplankton for modern biotechnological applications.

REFERENCES

Adomako, M., Ernst, D., Simkovsky, R., Chao, Y.-Y., Wang, J., Fang, M., et al. (2022). Comparative Genomics of *Synechococcus elongatus* Explains the Phenotypic Diversity of the Strains. *MBio*. doi: 10.1128/mbio.00862-22.

Akter, T., and Nakamoto, H. (2021). pH-regulated chaperone function of cyanobacterial Hsp90 and Hsp70: implications for light/dark regulation. *J. Biochem.* 170, 463–471.

Allahverdiyeva, Y., Mustila, H., Ermakova, M., Bersanini, L., Richaud, P., Ajlani, G., et al. (2013). Flavodiiron proteins Flv1 and Flv3 enable cyanobacterial growth and photosynthesis under fluctuating light. *Proc. Natl. Acad. Sci. U. S. A.* 110, 4111–4116. doi: 10.1073/pnas.1221194110.

Allen, J. F., and Martin, W. (2007). Evolutionary biology: Out of thin air. *Nature* 445, 610–612. doi: 10.1038/445610a.

Allen, M. M. (1968). Simple Conditions for Growth of Unicellular Blue-Green Algae on Plates. *J. Phycol.* 4, 1–4. doi: 10.1111/j.1529-8817.1968.tb04667.x.

Altschul, S. F., Madden, T. L., Schäffer, A. A., Zhang, J., Zhang, Z., Miller, W., et al. (1997). Gapped BLAST and PSI-BLAST: A new generation of protein database search programs. *Nucleic Acids Res.* 25, 3389–3402. doi: 10.1093/nar/25.17.3389.

Augst, A. D., Kong, H. J., and Mooney, D. J. (2006). Alginate hydrogels as biomaterials. *Macromol. Biosci.* 6, 623–633. doi: 10.1002/mabi.200600069.

Balskus, E. P., and Walsh, C. T. (2010). The genetic and molecular basis for sunscreen biosynthesis in cyanobacteria. *Science* 329, 1653–6. doi: 10.1126/science.1193637.

Barnes, P. W., Williamson, C. E., Lucas, R. M., Robinson, S. A., Madronich, S., Paul, N. D., et al. (2019). Ozone depletion, ultraviolet radiation, climate change and prospects for a sustainable future. *Nat. Sustain.* 2, 569–579.

Barron, J. A. (1996). Diatom constraints on the position of the Antarctic Polar Front in the middle part of the Pliocene. *Mar. Micropaleontol.* 27, 195–213.

Beckmann, M., Václavík, T., Manceur, A. M., Šprtová, L., von Wehrden, H., Welk, E., et al. (2014). glUV: A global UV-B radiation data set for macroecological studies. *Methods Ecol. Evol.* 5, 372–383. doi: 10.1111/2041-210X.12168.

Bečková, M., Gardian, Z., Yu, J., Konik, P., Nixon, P. J., and Komenda, J. (2017). Association of Psb28 and Psb27 proteins with PSII-PSI supercomplexes upon exposure of *Synechocystis* sp. PCC 6803 to high light. *Mol. Plant* 10, 62–72.

Benjamini, Y., and Hochberg, Y. (1995). Controlling the false discovery rate: a practical and powerful approach to multiple testing. *J. R. Stat. Soc. Ser. B* 57, 289–300.

Biller, S. J., Berube, P. M., Lindell, D., and Chisholm, S. W. (2015). *Prochlorococcus*: the structure and function of collective diversity. *Nat. Rev. Microbiol.* 13, 13–27.

Boelen, P., Obernostere, I., Vink, A. A., and Buma, A. G. J. (1999). Attenuation of biologically effective UV radiation in tropical Atlantic waters measured with a biochemical DNA dosimeter. *Photochem. Photobiol.* 69, 34–40.

Bourbonnais, R., and Paice, M. G. (1992). Demethylation and delignification of kraft pulp by Trametes versicolor laccase in the presence of 2,2′-azinobis-(3-ethylbenzthiazoline-6-sulphonate). *Appl. Microbiol. Biotechnol.* 36, 823–827. doi: 10.1007/BF00172202.

Buick, R. (2008). When did oxygenic photosynthesis evolve? *Philos. Trans. R. Soc. B Biol. Sci.* 363, 2731–2743. doi: 10.1098/rstb.2008.0041.

Cameron, J. C., and Pakrasi, H. B. (2010). Essential role of glutathione in acclimation to environmental and redox perturbations in the cyanobacterium *Synechocystis* sp. PCC 6803. *Plant Physiol.* 154, 1672–1685. doi: 10.1104/pp.110.162990.

Campbell, D., Eriksson, M. J., Öquist, G., Gustafsson, P., and Clarke, A. K. (1998). The cyanobacterium *Synechococcus* resists UV-B by exchanging photosystem II reaction-center D1 proteins. *Proc. Natl. Acad. Sci. U. S. A.* 95, 364–369. doi: 10.1073/pnas.95.1.364.

Cappiello, M., Lazzarotti, A., Buono, F., Scaloni, A., D'ambrosio, C., Amodeo, P., et al. (2004). New role for leucyl aminopeptidase in glutathione turnover. *Biochem. J.* 378, 35–44.

Carreto, J. I., and Carignan, M. O. (2011). Mycosporine-Like Amino Acids: Relevant Secondary Metabolites. Chemical and Ecological Aspects. *Mar. Drugs* 9, 387–446. doi: 10.3390/md9030387.

Carreto, J. I., Carignan, M. O., and Montoya, N. G. (2005). A high-resolution reverse-phase liquid chromatography method for the analysis of mycosporine-like amino acids (MAAs) in marine organisms. *Mar. Biol.* 146, 237–252. doi: 10.1007/s00227-004-1447-y.

Carreto, J. I., Carignan, M. O., Montoya, N. G., Cozzolino, E., and Akselman, R. (2018). Mycosporine-like amino acids and xanthophyll-cycle pigments favour a massive spring bloom development of the dinoflagellate *Prorocentrum minimum* in Grande Bay (Argentina), an ozone hole affected area. *J. Mar. Syst.* 178, 15–28.

Carreto, J. I., De Marco, S. G., and Lutz, V. A. (1989). UV-absorbing pigments in the dinoflagellates *Alexandrium excavatum* and *Prorocentrum micans*. Effects of light intensity. *Red tides Biol. Environ. Sci. Toxicol.*, 37–40.

Caruso, G., and Zaccone, R. (2000). Estimates of leucine aminopeptidase activity in different marine and brackish environments. *J. Appl. Microbiol.* 89, 951–959.

Cassier-Chauvat, C., Veaudor, T., and Chauvat, F. (2016). Comparative genomics of DNA recombination and repair in cyanobacteria: biotechnological implications. *Front. Microbiol.* 7, 1809.

Chakdar, H., Thapa, S., Srivastava, A., and Shukla, P. (2022). Genomic and proteomic insights into the heavy metal bioremediation by cyanobacteria. *J. Hazard. Mater.* 424, 127609. doi: 10.1016/j.jhazmat.2021.127609.

Chan, E. S., Yim, Z. H., Phan, S. H., Mansa, R. F., and Ravindra, P. (2010). Encapsulation of herbal aqueous extract through absorption with ca-alginate hydrogel beads. *Food Bioprod. Process.* 88, 195–201. doi: 10.1016/j.fbp.2009.09.005.

Chen, H., Cheng, Y., Tian, J., Yang, P., Zhang, X., Chen, Y., et al. (2020). Dissolved oxygen from microalgae-gel patch promotes chronic wound healing in diabetes. *Sci. Adv.* 6. doi: 10.1126/sciadv.aba4311.

Chen, Y., Holtman, C. K., Taton, A., and Golden, S. S. (2012). "Functional analysis of the *Synechococcus elongatus* PCC 7942 genome," in *Functional Genomics and Evolution of Photosynthetic Systems* (Springer), 119–137.

Childs, R. E., and Bardsley, W. G. (1975). The steady state kinetics of peroxidase with 2,2' azino di (3 ethylbenzthiazoline 6 sulphonic acid) as chromogen. *Biochem. J.* 145, 93–103. doi: 10.1042/bj1450093.

Chipperfield, M. P., Bekki, S., Dhomse, S., Harris, N. R. P., Hassler, B., Hossaini, R., et al. (2017). Detecting recovery of the stratospheric ozone layer. *Nature* 549, 211–218. doi: 10.1038/nature23681.

Chu, L., Lai, Y., Xu, X., Eddy, S., Yang, S., Song, L., et al. (2008). A 52-kDa leucyl aminopeptidase from *Treponema denticola* is a cysteinylglycinase that mediates the second step of glutathione metabolism. *J. Biol. Chem.* 283, 19351–19358.

Clerico, E. M., Ditty, J. L., and Golden, S. S. (2007). "Specialized techniques for site-directed mutagenesis in cyanobacteria," in *Circadian rhythms* (Springer), 155–171.

Constable, A. J., Melbourne-Thomas, J., Corney, S. P., Arrigo, K. R., Barbraud, C., Barnes, D. K. A., et al. (2014). Climate change and Southern Ocean ecosystems I: how changes in physical habitats directly affect marine biota. *Glob. Chang. Biol.* 20, 3004–3025.

Copley, S. D., and Dhillon, J. K. (2002). Lateral gene transfer and parallel evolution in the history of glutathione biosynthesis genes. *Genome Biol.* 3, 1–16.

Cortese, G., and Gersonde, R. (2008). Plio/Pleistocene changes in the main biogenic silica carrier in the Southern Ocean, Atlantic Sector. *Mar. Geol.* 252, 100–110.

Cullen, J. J., Neale, P. J., and Lesser, M. P. (1992). Biological Weighting Function for the Inhibition of Phytoplankton Photosynthesis by Ultraviolet Radiation. *Science.* 258, 646–650.

Danovaro, R., Bongiorni, L., Corinaldesi, C., Giovannelli, D., Damiani, E., Astolfi, P., et al. (2008). Sunscreens cause coral bleaching by promoting viral infections. *Environ. Health Perspect.* 116, 441–7. doi: 10.1289/ehp.10966.

David Des Marais (2000). When-Did-Photosynthesis-Emerge-on-Earth. *Science.* 289, 1703–1705.

Day, T. A., and Neale, P. J. (2002). Effects of UV-B radiation on terrestrial and aquatic primary producers. *Annu. Rev. Ecol. Syst.* 33, 371–396.

de Boyer Montégut, C., Madec, G., Fischer, A. S., Lazar, A., and Iudicone, D. (2004). Mixed layer depth over the global ocean: An examination of profile data and a profile-based climatology. *J. Geophys. Res. Ocean.* 109.

De Mora, S., Demers, S., and Vernet, M. (2000). The effects of UV radiation in the marine environment.

Delaye, L., González-Domenech, C. M., Garcillán-Barcia, M. P., Peretó, J., de la Cruz, F., and Moya, A. (2011). Blueprint for a minimal photoautotrophic cell: Conserved and variable genes in *Synechococcus elongatus* PCC 7942. *BMC Genomics* 12, 25. doi: 10.1186/1471-2164-12-25.

Diamond, S., Jun, D., Rubin, B. E., and Golden, S. S. (2015). The circadian oscillator in *Synechococcus elongatus* controls metabolite partitioning during diurnal growth. *Proc. Natl. Acad. Sci. U. S. A.* 112, E1916–E1925. doi: 10.1073/pnas.1504576112.

Dobáková, M., Sobotka, R., Tichy, M., and Komenda, J. (2009). Psb28 protein is involved in the biogenesis of the photosystem II inner antenna CP47 (PsbB) in the cyanobacterium *Synechocystis* sp. PCC 6803. *Plant Physiol.* 149, 1076–1086.

Downs, C. A., Fauth, J. E., Wetzel, D., Hallock, P., Halas, J. F., Halas, J. C., et al. (2006). Investigating coral reef degradation at Alina's Reef in the Florida Keys: Cellular physiology of white grunt (*Haemulon plumieri*) as a biological indicator. *Environ. Forensics* 7, 15–32. doi: 10.1080/15275920500351775.

Ducat, D. C., Way, J. C., and Silver, P. A. (2011). Engineering cyanobacteria to generate high-value products. *Trends Biotechnol.* 29, 95–103. doi: 10.1016/j.tibtech.2010.12.003.

Dunlap, W. C., and Shick, J. M. (1998). Ultraviolet radiation-absorbing mycosporine-like amino acids in coral reef organisms: A biochemical and environmental perspective. *J. Phycol.* 34, 418–430. doi: 10.1046/j.1529-8817.1998.340418.x.

Duraj-Thatte, A. M., Manjula-Basavanna, A., Courchesne, N. M. D., Cannici, G. I., Sánchez-Ferrer, A., Frank, B. P., et al. (2021). Water-processable, biodegradable and coatable aquaplastic from engineered biofilms. *Nat. Chem. Biol.* 17, 732–738. doi: 10.1038/s41589-021-00773-y.

Dutkiewicz, S., Hickman, A. E., Jahn, O., Gregg, W. W., Mouw, C. B., and Follows, M. J. (2015). Capturing optically important constituents and properties in a marine biogeochemical and ecosystem model. *Biogeosciences* 12, 4447–4481. doi: 10.5194/bg-12-4447-2015.

Elhai, J., Vepritskiy, A., Muro-Pastor, A. M., Flores, E., and Wolk, C. P. (1997). Reduction of conjugal transfer efficiency by three restriction activities of *Anabaena* sp. strain PCC 7120. *J. Bacteriol.* 179, 1998–2005.

Engler, C., Kandzia, R., and Marillonnet, S. (2008). A one pot, one step, precision cloning method with high throughput capability. *PLoS One* 3, e3647.

Erickson, D. J., Sulzberger, B., Zepp, R. G., and Austin, A. T. (2015). Effects of stratospheric ozone depletion, solar UV radiation, and climate change on biogeochemical cycling: Interactions and feedbacks. *Photochem. Photobiol. Sci.* 14, 127–148. doi: 10.1039/c4pp90036g.

Fahey, D., Newman, P. A., Pyle, J. A., Safari, B., Chipperfield, M. P., Karoly, D., et al. (2018). Scientific Assessment of Ozone Depletion: 2018, Global Ozone Research and Monitoring Project-Report No. 58.

Fahey, R. C. (2001). Novel thiols of prokaryotes. *Annu. Rev. Microbiol.* 55, 333–356.

Falkowski, P. G. (1994). The role of phytoplankton photosynthesis in global biogeochemical cycles. *Photosynth. Res.* 39, 235–258. doi: 10.1007/BF00014586.

Fang, X., Park, S., Saito, T., Tunnicliffe, R., Ganesan, A. L., Rigby, M., et al. (2019). Rapid increase in ozone-depleting chloroform emissions from China. *Nat. Geosci.* 12, 89–93.

Field, C. B., Behrenfeld, M. J., Randerson, J. T., and Falkowski, P. (1998). Primary production of the biosphere: Integrating terrestrial and oceanic components. *Science.* 281, 237–240. doi: 10.1126/science.281.5374.237.

Fowler, J. H., Narváez-Vásquez, J., Aromdee, D. N., Pautot, V., Holzer, F. M., and Walling, L. L. (2009). Leucine aminopeptidase regulates defense and wound signaling in tomato downstream of jasmonic acid. *Plant Cell* 21, 1239–1251.

Gaitonde, M. K. (1967). A spectrophotometric method for the direct determination of cysteine in the presence of other naturally occurring amino acids. *Biochem. J.* 104, 627.

Gieskes, W. W. C., and Kraay, G. W. (1990). Transmission of ultraviolet light in the Weddell Sea: report of the first measurements made in the Antarctic. *Biomass Newsl.* 12, 12–14.

Golden, S. S. (2019). The international journeys and aliases of *Synechococcus elongatus*. *New Zeal. J. Bot.* 57, 70–75. doi: 10.1080/0028825X.2018.1551805.

González, L. M., Mukhitov, N., and Voigt, C. A. (2020). Resilient living materials built by printing bacterial spores. *Nat. Chem. Biol.* 16, 126–133. doi: 10.1038/s41589-019-0412-5.

Häder, D.-P., Helbling, E. W., Williamson, C. E., and Worrest, R. C. (2011). Effects of UV radiation on aquatic ecosystems and interactions with climate change. *Photochem. Photobiol. Sci.* 10, 242. doi: 10.1039/c0pp90036b.

Häder, D.-P., Williamson, C. E., Wängberg, S.-Å., Rautio, M., Rose, K. C., Gao, K., et al. (2015). Effects of UV radiation on aquatic ecosystems and interactions with other environmental factors. *Photochem. Photobiol. Sci.* 14, 108–126.

Häder, D. P., and Sinha, R. P. (2005). Solar ultraviolet radiation-induced DNA damage in aquatic organisms: potential environmental impact. *Mutat. Res. Mol. Mech. Mutagen.* 571, 221–233. doi: 10.1016/j.mrfmmm.2004.11.017.

Hager, M., Hermann, M., Biehler, K., Krieger-Liszkay, A., and Bock, R. (2002). Lack of the small plastid-encoded PsbJ polypeptide results in a defective water-splitting apparatus of photosystem II, reduced photosystem I levels, and hypersensitivity to light. *J. Biol. Chem.* 277, 14031–14039.

Han, S., Han, W., Chen, J., Sun, Y., Dai, M., and Zhao, G. (2020). Bioremediation of malachite green by cyanobacterium *Synechococcus elongatus* PCC 7942 engineered with a triphenylmethane reductase gene. *Appl. Microbiol. Biotechnol.* 104, 3193–3204. doi: 10.1007/s00253-020-10438-w.

Harris, N. R. P., Montzka, S. A., Newman, P. A., and others (2019). Report on the International Symposium on the Unexpected Increase in emissions of ozone-depleting CFC-11. *SPARC Newsl.* 53, 9–18.

Helbling, E. W., Chalker, B. E., Dunlap, W. C., Holm-Hansen, O., and Villafañe, V. E. (1996). Photoacclimation of Antarctic marine diatoms to solar ultraviolet radiation. *J. Exp. Mar. Bio. Ecol.* 204, 85–101.

Hernando, M., Carreto, J. I., Carignan, M. O., Ferreyra, G. A., and Gross, C. (2002). "Effects of solar radiation on growth and mycosporine-like amino acids content in *Thalassiosira* sp, an Antarctic diatom," in *Ecological Studies in the Antarctic Sea Ice Zone* (Springer), 237–245.

Hessen, D. O. (1993). DNA-damage and pigmentation in alpine and arctic zooplankton as bioindicators of UV-radiation. *SIL Proceedings, 1922-2010* 25, 482–486. doi: 10.1080/03680770.1992.11900171.

Holtrop, T., Huisman, J., Stomp, M., Biersteker, L., Aerts, J., Grébert, T., et al. (2020). Vibrational modes of water predict spectral niches for photosynthesis in lakes and oceans. *Nat. Ecol. Evol.* doi: 10.1038/s41559-020-01330-x.

Hood, E.M., Sabine, C.L. and Sloyan, B. M. (2010). The GO-SHIP Repeat Hydrography Manual: a collection of expert reports and guidelines, Version 1. doi: https://doi.org/10.25607/OBP-1341.

Hood, E., Fellman, J. B., and Spencer, R. G. M. (2020). Glacier Loss Impacts Riverine Organic Carbon Transport to the Ocean. *Geophys. Res. Lett.* 47, 0–3. doi: 10.1029/2020GL089804.

Ingalls, A. E., Whitehead, K., and Bridoux, M. C. (2010). Tinted windows: The presence of the UV absorbing compounds called mycosporine-like amino acids embedded in the frustules of marine diatoms. *Geochim. Cosmochim. Acta* 74, 104–115.

Ivleva, N. B., Bramlett, M. R., Lindahl, P. A., and Golden, S. S. (2005). LdpA: a component of the circadian clock senses redox state of the cell. *EMBO J.* 24, 1202–1210.

Jeffrey, S. W., MacTavish, H. S., Dunlap, W. C., Vesk, M., and Groenewoud, K. (1999). Occurrence of UVA-and UVB-absorbing compounds in 152 species (206 strains) of marine microalgae. *Mar. Ecol. Prog. Ser.* 189, 35–51.

Jin, P., Duarte, C. M., and Agusti, S. (2017). Contrasting responses of marine and freshwater photosynthetic organisms to UVB radiation: a meta-analysis. *Front. Mar. Sci.* 4, 45.

Jösch, C., Klotz, L.-O., and Sies, H. (2003). Identification of cytosolic leucyl aminopeptidase (EC 3.4. 11.1) as the major cysteinylglycine-hydrolysing activity in rat liver.

Joshi, S., Cook, E., and Mannoor, M. S. (2018). Bacterial Nanobionics via 3D Printing. *Nano Lett.* 18, 7448–7456. doi: 10.1021/acs.nanolett.8b02642.

Kahru, M., Anderson, C., Barton, A. D., Carter, M. L., Catlett, D., Send, U., et al. (2021). Satellite detection of dinoflagellate blooms off California by UV reflectance ratios. *Elem. Sci. Anthr.* 9. doi: 10.1525/elementa.2020.00157.

Kahru, M., and Mitchell, B. G. (1998). Spectral reflectance and absorption of a massive red tide off southern California. *J. Geophys. Res. Ocean.* 103, 21601–21609.

Kawasaki, K., and Iwasaki, H. (2020). Involvement of glycogen metabolism in circadian control of UV resistance in cyanobacteria. *PLoS Genet.* 16, e1009230.

Kobayashi, M., Ishizuka, T., Katayama, M., Kanehisa, M., Bhattacharyya-Pakrasi, M., Pakrasi, H. B., et al. (2004). Response to oxidative stress involves a novel peroxiredoxin gene in the unicellular cyanobacterium *Synechocystis* sp. PCC 6803. *Plant Cell Physiol.* 45, 290–299. doi: 10.1093/pcp/pch034.

Kumar, S., Kaur, A., Chattopadhyay, B., and Bachhawat, A. K. (2015). Defining the cytosolic pathway of glutathione degradation in *Arabidopsis thaliana*: role of the ChaC/GCG family of γ-glutamyl cyclotransferases as glutathione-degrading enzymes and AtLAP1 as the Cys-Gly peptidase. *Biochem. J.* 468, 73–85.

Kwak, S. Y., Giraldo, J. P., Lew, T. T. S., Wong, M. H., Liu, P., Yang, Y. J., et al. (2018). Polymethacrylamide and Carbon Composites that Grow, Strengthen, and Self-Repair using Ambient Carbon Dioxide Fixation. *Adv. Mater.* 30, 1–10. doi: 10.1002/adma.201804037.

Latasa, M. (2007). Improving estimations of phytoplankton class abundances using CHEMTAX. *Mar. Ecol. Prog. Ser.* 329, 13–21.

Lawrence, M., Huber, W., Pages, H., Aboyoun, P., Carlson, M., Gentleman, R., et al. (2013). Software for computing and annotating genomic ranges. *PLoS Comput. Biol.* 9, e1003118.

Leite, G. B., Abdelaziz, A. E. M., and Hallenbeck, P. C. (2013). Algal biofuels: Challenges and opportunities. *Bioresour. Technol.* 145, 134–141. doi: 10.1016/j.biortech.2013.02.007.

Lesser, M. P. (1996). Acclimation of phytoplankton to UV-B radiation: oxidative stress and photoinhibition of photosynthesis are not prevented by UV-absorbing compounds in the dinoflagellate *Prorocentrum micans*. *Mar. Ecol. Prog. Ser.* 132, 287–297.

Li, L., Lin, Q., Tang, M., Duncan, A. J. E., and Ke, C. (2019). Advanced Polymer Designs for Direct-Ink-Write 3D Printing. *Chem. - A Eur. J.* 25, 10768–10781. doi: 10.1002/chem.201900975.

Li, T., Fan, H., Li, Z., Wei, J., Cai, Y., and Lin, Y. (2011). Effect of different light quality on DNA methylation variation for brown cotton (*Gossypium hirstum*). *African J. Biotechnol.* 10, 6220–6226. doi: 10.5897/AJB10.1569.

Liang, Y., Hou, J., Liu, Y., Luo, Y., Tang, J., Cheng, J. J., et al. (2018). Textile Dye Decolorizing *Synechococcus* PCC7942 Engineered With CotA Laccase. *Front. Bioeng. Biotechnol.* 6, 1–10. doi: 10.3389/fbioe.2018.00095.

Lind, L. K., Shukla, V. K., Nyhus, K. J., and Pakrasi, H. B. (1993). Genetic and immunological analyses of the cyanobacterium *Synechocystis* sp. PCC 6803 show that the protein encoded by the psbJ gene regulates the number of photosystem II centers in thylakoid membranes. *J. Biol. Chem.* 268, 1575–1579. doi: 10.1016/s0021-9258(18)53891-6.

Liu, H., Huang, R. Y.-C., Chen, J., Gross, M. L., and Pakrasi, H. B. (2011). Psb27, a transiently associated protein, binds to the chlorophyll binding protein CP43 in photosystem II assembly intermediates. *Proc. Natl. Acad. Sci.* 108, 18536–18541.

Llewellyn, C. A., and Airs, R. L. (2010). Distribution and abundance of MAAs in 33 species of microalgae across 13 classes. *Mar. Drugs* 8, 1273–1291.

Llewellyn, C. A., Greig, C., Silkina, A., Kultschar, B., Hitchings, M. D., and Farnham, G. (2020). Mycosporine-like amino acid and aromatic amino acid transcriptome response to UV and far-red light in the cyanobacterium *Chlorogloeopsis fritschii* PCC 6912. *Sci. Rep.* 10, 1–13.

Llewellyn, C. A., and Harbour, D. S. (2003). A temporal study of mycosporine-like amino acids in surface water phytoplankton from the English Channel and correlation with solar irradiation. *J. Mar. Biol. Assoc. United Kingdom* 83, 1–9.

Llewellyn, C. A., White, D. A., Martinez-Vincente, V., Tarran, G., and Smyth, T. J. (2012). Distribution of mycosporine-like amino acids along a surface water meridional transect of the Atlantic. *Microb. Ecol.* 64, 320–333.

Love, M. I., Anders, S., Kim, V., and Huber, W. (2015). RNA-Seq workflow: gene-level exploratory analysis and differential expression. *F1000Research* 4, 1070. doi: 10.12688/f1000research.7035.1.

Ma, A. T., Schmidt, C. M., and Golden, J. W. (2014). Regulation of gene expression in diverse cyanobacterial species by using theophylline-responsive riboswitches. *Appl. Environ. Microbiol.* 80, 6704–6713. doi: 10.1128/AEM.01697-14.

Mackey, M. D., Mackey, D. J., Higgins, H. W., and Wright, S. W. (1996). CHEMTAX-a program for estimating class abundances from chemical markers: application to HPLC measurements of phytoplankton. *Mar. Ecol. Prog. Ser.* 144, 265–283.

Maharjan, S., Alva, J., Cámara, C., Rubio, A. G., Hernández, D., Delavaux, C., et al. (2021). Symbiotic Photosynthetic Oxygenation within 3D-Bioprinted Vascularized Tissues. *Matter* 4, 217–240. doi: 10.1016/j.matt.2020.10.022.

Mangan, N. M., Flamholz, A., Hood, R. D., Milo, R., and Savage, D. F. (2016). pH determines the energetic efficiency of the cyanobacterial CO_2 concentrating mechanism. *Proc. Natl. Acad. Sci.* 113, E5354--E5362.

Masip, L., Veeravalli, K., and Georgiou, G. (2006). The many faces of glutathione in bacteria. *Antioxid. Redox Signal.* 8, 753–762.

Matsunaga, T., Burgess, J. G., Yamada, N., Komatsu, K., Yoshida, S., and Wachi, Y. (1993). An ultraviolet (UV-A) absorbing biopterin glucoside from the marine planktonic cyanobacterium *Oscillatoria* sp. *Appl. Microbiol. Biotechnol.* 39, 250–253. doi: 10.1007/BF00228614.

Mloszewska, A. M., Cole, D. B., Planavsky, N. J., Kappler, A., Whitford, D. S., Owttrim, G. W., et al. (2018). UV radiation limited the expansion of cyanobacteria in early marine photic environments. *Nat. Commun.* 9, 1–8.

Mohsin, M. Z., Omer, R., Huang, J., Mohsin, A., Guo, M., Qian, J., et al. (2021). Advances in engineered *Bacillus subtilis* biofilms and spores, and their applications in bioremediation, biocatalysis, and biomaterials. *Synth. Syst. Biotechnol.* 6, 180–191. doi: 10.1016/j.synbio.2021.07.002.

Moisan, T. A., and Mitchell, B. G. (2001). UV absorption by mycosporine-like amino acids in *Phaeocystis antarctica Karsten* induced by photosynthetically available radiation. *Mar. Biol.* 138, 217–227.

Morty, R. E., and Morehead, J. (2002). Cloning and characterization of a leucyl aminopeptidase from three pathogenic Leishmania species. *J. Biol. Chem.* 277, 26057–26065.

Mulo, P., Sicora, C., and Aro, E. M. (2009). Cyanobacterial psbA gene family: Optimization of oxygenic photosynthesis. *Cell. Mol. Life Sci.* 66, 3697–3710. doi: 10.1007/s00018-009-0103-6.

Neale, P. J., Davis, R. F., and Cullen, J. J. (1998). Interactive ozone depletion and vertical mixing on photosynthesis of antarctic phytoplankton. *Nature* 392, 585–589. doi: 10.1038/33374.

Neale, P. J., and Thomas, B. C. (2017). Inhibition by ultraviolet and photosynthetically available radiation lowers model estimates of depth-integrated picophytoplankton photosynthesis: global predictions for *Prochlorococcus* and *Synechococcus*. *Glob. Chang. Biol.* 23, 293–306. doi: 10.1111/gcb.13356.

Nowaczyk, M. M., Krause, K., Mieseler, M., Sczibilanski, A., Ikeuchi, M., and Rögner, M. (2012). Deletion of psbJ leads to accumulation of Psb27--Psb28 photosystem II complexes in *Thermosynechococcus elongatus*. *Biochim. Biophys. Acta (BBA)-Bioenergetics* 1817, 1339–1345.

Oliver, N. J., Rabinovitch-Deere, C. A., Carroll, A. L., Nozzi, N. E., Case, A. E., and Atsumi, S. (2016). Cyanobacterial metabolic engineering for biofuel and chemical production. *Curr. Opin. Chem. Biol.* 35, 43–50. doi: 10.1016/j.cbpa.2016.08.023.

Orfanoudaki, M., Hartmann, A., Karsten, U., and Ganzera, M. (2019). Chemical profiling of mycosporine-like amino acids in twenty-three red algal species. *J. Phycol.* 55, 393–403. doi: 10.1111/jpy.12827.

Orsi, A. H., Whitworth, T., and Nowlin, W. D. (1995). On the meridional extent and fronts of the Antarctic Circumpolar Current. *Deep. Res. Part I* 42, 641–673. doi: 10.1016/0967-0637(95)00021-W.

Oubelkheir, K., Clementson, L. A., Moore, G. F., and Tilstone, G. H. (2013). Production of mycosporine-like amino acids by phytoplankton under ultraviolet radiation exposure in the Sub-Antarctic Zone south of Tasmania. *Mar. Ecol. Prog. Ser.* 494, 41–63.

Pagliano, C., Saracco, G., and Barber, J. (2013). Structural, functional and auxiliary proteins of photosystem II. *Photosynth. Res.* 116, 167–188.

Paolicchi, A., Dominici, S., Pieri, L., Maellaro, E., and Pompella, A. (2002). Glutathione catabolism as a signaling mechanism. *Biochem. Pharmacol.* 64, 1027–1035.

Pierce, E. C., Morin, M., Little, J. C., Liu, R. B., Tannous, J., Keller, N. P., et al. (2021). Bacterial–fungal interactions revealed by genome-wide analysis of bacterial mutant fitness. *Nat. Microbiol.* 6, 87–102. doi: 10.1038/s41564-020-00800-z.

Portwich, A., and Garcia-Pichel, F. (1999). Ultraviolet and osmotic stresses induce and regulate the synthesis of mycosporines in the cyanobacterium *Chlorogloeopsis* PCC 6912. *Arch. Microbiol.* 172, 187–192.

Rai, R., Singh, S., Rai, K. K., Raj, A., Sriwastaw, S., and Rai, L. C. (2021). Regulation of antioxidant defense and glyoxalase systems in cyanobacteria. *Plant Physiol. Biochem.* 168, 353–372.

Ralph, P. J., and Gademann, R. (2005). Rapid light curves: A powerful tool to assess photosynthetic activity. *Aquat. Bot.* 82, 222–237. doi: 10.1016/j.aquabot.2005.02.006.

Rastogi, R. P., and Incharoensakdi, A. (2013). UV radiation-induced accumulation of photoprotective compounds in the green alga *Tetraspora* sp. CU2551. *Plant Physiol. Biochem.* 70. doi: 10.1016/j.plaphy.2013.04.021.

Rastogi, R. P., and Incharoensakdi, A. (2014). UV radiation-induced biosynthesis, stability and antioxidant activity of mycosporine-like amino acids (MAAs) in a unicellular

cyanobacterium *Gloeocapsa* sp. CU2556. *J. Photochem. Photobiol. B Biol.* 130, 287–292.

Rastogi, R. P., Singh, S. P., Häder, D.-P., and Sinha, R. P. (2010). Detection of reactive oxygen species (ROS) by the oxidant-sensing probe 2′, 7′-dichlorodihydrofluorescein diacetate in the cyanobacterium *Anabaena variabilis* PCC 7937. *Biochem. Biophys. Res. Commun.* 397, 603–607.

Regel, R. E., Ivleva, N. B., Zer, H., Meurer, J., Shestakov, S. V, Herrmann, R. G., et al. (2001). Deregulation of electron flow within photosystem II in the absence of the PsbJ protein. *J. Biol. Chem.* 276, 41473–41478.

Riegger, L., and Robinson, D. (1997). Photoinduction of UV-absorbing compounds in Antarctic diatoms and *Phaeocystis antarctica*. *Mar. Ecol. Prog. Ser.* 160, 13–25.

Rodrigo-Navarro, A., Sankaran, S., Dalby, M. J., del Campo, A., and Salmeron-Sanchez, M. (2021). Engineered living biomaterials. *Nat. Rev. Mater.* 6, 1175–1190. doi: 10.1038/s41578-021-00350-8.

Roose, J. L., and Pakrasi, H. B. (2008). The Psb27 protein facilitates manganese cluster assembly in photosystem II. *J. Biol. Chem.* 283, 4044–4050.

Rubin, B. E., Huynh, T. A. N., Welkie, D. G., Diamond, S., Simkovsky, R., Pierce, E. C., et al. (2018). High-throughput interaction screens illuminate the role of c-di-AMP in cyanobacterial nighttime survival. *PLoS Genet.* 14, 1–21. doi: 10.1371/journal.pgen.1007301.

Rubin, B. E., Wetmore, K. M., Price, M. N., Diamond, S., Shultzaberger, R. K., Lowe, L. C., et al. (2015). The essential gene set of a photosynthetic organism. *Proc. Natl. Acad. Sci.* 112, E6634--E6643.

Russo, D. A., Zedler, J. A. Z., Conradi, F. D., Schuergers, N., Jensen, P. E., Mullineaux, C. W., et al. (2022). Development of a highly sensitive luciferase-based reporter system to study two-step protein secretion in cyanobacteria. *J. Bacteriol.* 204, e00504--21.

Sakata, S., Mizusawa, N., Kubota-Kawai, H., Sakurai, I., and Wada, H. (2013). Psb28 is involved in recovery of photosystem II at high temperature in *Synechocystis* sp. PCC 6803. *Biochim. Biophys. Acta (BBA)-Bioenergetics* 1827, 50–59.

Santos-Merino, M., Singh, A. K., and Ducat, D. C. (2019). New applications of synthetic biology tools for cyanobacterial metabolic engineering. *Front. Bioeng. Biotechnol.* 7, 1–24. doi: 10.3389/fbioe.2019.00033.

Sarker, B., Rompf, J., Silva, R., Lang, N., Detsch, R., Kaschta, J., et al. (2015). Alginate-based hydrogels with improved adhesive properties for cell encapsulation. *Int. J. Biol. Macromol.* 78, 72–78. doi: 10.1016/j.ijbiomac.2015.03.061.

Sawa, M., Fantuzzi, A., Bombelli, P., Howe, C. J., Hellgardt, K., and Nixon, P. J. (2017). Electricity generation from digitally printed cyanobacteria. *Nat. Commun.* 8, 1–9. doi:

10.1038/s41467-017-01084-4.

Schaefer, M. R., and Golden, S. S. (1989). Differential expression of members of a cyanobacterial psbA gene family in response to light. *J. Bacteriol.* 171, 3973–3981. doi: 10.1128/jb.171.7.3973-3981.1989.

Schmid, D., Schuerch, C., and Zuelli, F. (2004). Harmless, natural cosmetic skin treatment compositions, for protecting against UV-A induced lipid oxidation and premature aging, containing mycosporine-like amino acids. *Pat. number EPI 1473028-AL*.

Scranton, M. A., Fowler, J. H., Girke, T., and Walling, L. L. (2013). Microarray analysis of tomato's early and late wound response reveals new regulatory targets for leucine aminopeptidase A. *PLoS One* 8, e77889.

Shaku, K., Shimakawa, G., Hashiguchi, M., and Miyake, C. (2016). Reduction-induced suppression of electron flow (RISE) in the photosynthetic electron transport system of *Synechococcus elongatus* PCC 7942. *Plant Cell Physiol.* 57, 1443–1453. doi: 10.1093/pcp/pcv198.

Sharma, K. K., and Ortwerth, B. J. (1986). Aminopeptidase III activity in normal and cataractous lenses. *Curr. Eye Res.* 5, 373–380.

Sheridan, K. J., Duncan, E. J., Eaton-Rye, J. J., and Summerfield, T. C. (2020). The diversity and distribution of D1 proteins in cyanobacteria. *Photosynth. Res.* 145, 111–128. doi: 10.1007/s11120-020-00762-7.

Shick, J. M., and Dunlap, W. C. (2002). Mycosporine-like amino acids and related gadusols: biosynthesis, accumulation, and UV-protective functions in aquatic organisms. *Annu. Rev. Physiol.* 64, 223–262.

Simkovsky, R., Parnasa, R., Wang, J., Nagar, E., Zecharia, E., Suban, S., et al. (2022). Transcriptomic and phenomic investigations reveal elements in biofilm repression and formation in the cyanobacterium *Synechococcus elongatus* PCC 7942. *bioRxiv*.

Singh, A. K., Bhattacharyya-Pakrasi, M., Elvitigala, T., Ghosh, B., Aurora, R., and Pakrasi, H. B. (2009). A systems-level analysis of the effects of light quality on the metabolism of a cyanobacterium. *Plant Physiol.* 151, 1596–1608.

Singh, S. P., Häder, D.-P., and Sinha, R. P. (2010). Cyanobacteria and ultraviolet radiation (UVR) stress: Mitigation strategies. *Ageing Res. Rev.* 9, 79–90. doi: 10.1016/j.arr.2009.05.004.

Sinha, R. P., Singh, S. P., and Häder, D.-P. (2007). Database on mycosporines and mycosporine-like amino acids (MAAs) in fungi, cyanobacteria, macroalgae, phytoplankton and animals. *J. Photochem. Photobiol. B Biol.* 89, 29–35. doi: 10.1016/j.jphotobiol.2007.07.006.

Smyth, T. J. (2011). Penetration of UV irradiance into the global ocean. *J. Geophys. Res.* 116, C11020. doi: 10.1029/2011JC007183.

Stelljes, C., and Koenig, F. (2007). Specific binding of D1 protein degradation products to the psbAI promoter in *Synechococcus* sp. strain PCC 7942. *J. Bacteriol.* 189, 1722–1726. doi: 10.1128/JB.01428-06.

Stomp, M., Huisman, J., Stal, L. J., and Matthijs, H. C. P. (2007). Colorful niches of phototrophic microorganisms shaped by vibrations of the water molecule. *ISME J.* 1, 271–282. doi: 10.1038/ismej.2007.59.

Suzuki, H., Kamatani, S., Kim, E. S., and Kumagai, H. (2001). Aminopeptidases A, B, and N and dipeptidase D are the four cysteinylglycinases of *Escherichia coli* K-12. *J. Bacteriol.* 183, 1489–1490. doi: 10.1128/JB.183.4.1489-1490.2001.

Taton, A., Ecker, A., Diaz, B., Moss, N. A., Anderson, B., Reher, R., et al. (2020). Heterologous expression of cryptomaldamide in a cyanobacterial host. *ACS Synth. Biol.* 9, 3364–3376.

Taton, A., Ma, A. T., Ota, M., Golden, S. S., and Golden, J. W. (2017). NOT Gate Genetic Circuits to Control Gene Expression in Cyanobacteria. *ACS Synth. Biol.* 6, 2175–2182. doi: 10.1021/acssynbio.7b00203.

Taton, A., Rohrer, S., Diaz, B., Reher, R., Mauricio, A., Rodriguez, C., et al. (2022). Heterologous Expression in *Anabaena* of the Columbamide Pathway from the Cyanobacterium *Moorena bouillonii* and Production of New Analogs. doi: 10.1021/acschembio.2c00347.

Taton, A., Unglaub, F., Wright, N. E., Zeng, W. Y., Paz-Yepes, J., Brahamsha, B., et al. (2014). Broad-host-range vector system for synthetic biology and biotechnology in cyanobacteria. *Nucleic Acids Res.* 42, e136--e136.

Tay, P. K. R., Nguyen, P. Q., and Joshi, N. S. (2017). A Synthetic Circuit for Mercury Bioremediation Using Self-Assembling Functional Amyloids. *ACS Synth. Biol.* 6, 1841–1850. doi: 10.1021/acssynbio.7b00137.

Till, P., Toepel, J., Bühler, B., Mach, R. L., and Mach-Aigner, A. R. (2020). Regulatory systems for gene expression control in cyanobacteria. *Appl. Microbiol. Biotechnol.* 104, 1977–1991. doi: 10.1007/s00253-019-10344-w.

Trampe, E., and Kühl, M. (2016). Chlorophyll f distribution and dynamics in cyanobacterial beachrock biofilms. *J. Phycol.* 52, 990–996. doi: 10.1111/jpy.12450.

Truglio, J. J., Croteau, D. L., Van Houten, B., and Kisker, C. (2006). Prokaryotic nucleotide excision repair: the UvrABC system. *Chem. Rev.* 106, 233–252.

Tsinoremas, N. F., Schaefer, M. R., and Golden, S. S. (1994). Blue and red light reversibly control psbA expression in the cyanobacterium *Synechococcus* sp. strain PCC 7942. *J. Biol. Chem.* 269, 16143–16147. doi: 10.1016/s0021-9258(17)33984-4.

Verhounig, A., Karcher, D., and Bock, R. (2010). Inducible gene expression from the plastid genome by a synthetic riboswitch. *Proc. Natl. Acad. Sci. U. S. A.* 107, 6204–6209. doi:

10.1073/pnas.0914423107.

Vijay, D., Akhtar, M. K., and Hess, W. R. (2019). Genetic and metabolic advances in the engineering of cyanobacteria. *Curr. Opin. Biotechnol.* 59, 150–156. doi: 10.1016/j.copbio.2019.05.012.

Vinyard, D. J., Gimpel, J., Ananyev, G. M., Cornejo, M. A., Golden, S. S., Mayfield, S. P., et al. (2013). Natural variants of photosystem II subunit D1 tune photochemical fitness to solar intensity. *J. Biol. Chem.* 288, 5451–5462. doi: 10.1074/jbc.M112.394668.

Wachi, Y., Grant Burgess, J., Iwamoto, K., Yamada, N., Nakamura, N., and Matsunaga, T. (1995). Effect of ultraviolet-A (UV-A) light on growth, photosynthetic activity and production of biopterin glucoside by the marine UV-A resistant cyanobacterium *Oscillatoria* sp. *BBA - Gen. Subj.* 1244, 165–168. doi: 10.1016/0304-4165(94)00219-N.

Wada, N., Sakamoto, T., and Matsugo, S. (2015). Mycosporine-Like Amino Acids and Their Derivatives as Natural Antioxidants. *Antioxidants (Basel, Switzerland)* 4, 603–46. doi: 10.3390/antiox4030603.

Wang, W., Yao, L., Cheng, C. Y., Zhang, T., Atsumi, H., Wang, L., et al. (2017). Harnessing the hygroscopic and biofluorescent behaviors of genetically tractable microbial cells to design biohybrid wearables. *Sci. Adv.* 3, 1–9. doi: 10.1126/sciadv.1601984.

Wangpraseurt, D., Lichtenberg, M., Jacques, S. L., Larkum, A. W. D., and Kühl, M. (2019). Optical properties of corals distort variable chlorophyll fluorescence measurements. *Plant Physiol.* 179, 1608–1619. doi: 10.1104/pp.18.01275.

Wangpraseurt, D., Sun, Y., You, S., Chua, S. T., Noel, S. K., Willard, H. F., et al. (2022). Bioprinted Living Coral Microenvironments Mimicking Coral-Algal Symbiosis. *Adv. Funct. Mater.* 2202273, 1–11. doi: 10.1002/adfm.202202273.

Wangpraseurt, D., You, S., Azam, F., Jacucci, G., Gaidarenko, O., Hildebrand, M., et al. (2020). Bionic 3D printed corals. *Nat. Commun.* 11. doi: 10.1038/s41467-020-15486-4.

Webber, R. E., and Shull, K. R. (2004). Strain dependence of the viscoelastic properties of alginate hydrogels. *Macromolecules* 37, 6153–6160. doi: 10.1021/ma049274n.

Weigand, J. E., and Suess, B. (2009). Aptamers and riboswitches: Perspectives in biotechnology. *Appl. Microbiol. Biotechnol.* 85, 229–236. doi: 10.1007/s00253-009-2194-2.

Welkie, D. G., Rubin, B. E., Chang, Y.-G., Diamond, S., Rifkin, S. A., LiWang, A., et al. (2018). Genome-wide fitness assessment during diurnal growth reveals an expanded role of the cyanobacterial circadian clock protein KaiA. *Proc. Natl. Acad. Sci.* 115, E7174--E7183.

Wetmore, K. M., Price, M. N., Waters, R. J., Lamson, J. S., He, J., Hoover, C. A., et al. (2015). Rapid quantification of mutant fitness in diverse bacteria by sequencing randomly bar-coded transposons. *MBio* 6, e00306--15.

Whitehead, K., and Vernet, M. (2000). Influence of mycosporine-like amino acids (MAAs) on UV absorption by particulate and dissolved organic matter in La Jolla Bay. *Limnol. Oceanogr.* 45, 1788–1796.

World Meteorological Organization (WMO) (2018). Executive Summary: Scientific Assessment of Ozone Depletion: 2018. *Glob. Ozone Res. Monit. Proj.* Report No.

Wright, S. W., Thomas, D. P., Marchant, H. J., Higgins, H. W., Mackey, M. D., and Mackey, D. J. (1996). Analysis of phytoplankton of the Australian sector of the Southern Ocean: Comparisons of microscopy and size frequency data with interpretations of pigment HPLC data using the "CHEMTAX" matrix factorisation program. *Mar. Ecol. Prog. Ser.* 144, 285–298. doi: 10.3354/meps144285.

Yang, G., Cozad, M. A., Holland, D. A., Zhang, Y., Luesch, H., and Ding, Y. (2018a). Photosynthetic Production of Sunscreen Shinorine Using an Engineered Cyanobacterium. *ACS Synth. Biol.* 7, 664–671. doi: 10.1021/acssynbio.7b00397.

Yang, Y., Lam, V., Adomako, M., Simkovsky, R., Jakob, A., Rockwell, N. C., et al. (2018b). Phototaxis in a wild isolate of the cyanobacterium *Synechococcus elongatus*. *Proc. Natl. Acad. Sci. U. S. A.* 115, E12378–E12387. doi: 10.1073/pnas.1812871115.

Zapata, M., Rodríguez, F., and Garrido, J. L. (2000). Separation of chlorophylls and carotenoids from marine phytoplankton: A new HPLC method using a reversed phase C8 column and pyridine-containing mobile phases. *Mar. Ecol. Prog. Ser.* 195, 29–45. doi: 10.3354/meps195029.

Zhang, M., and Zhao, X. (2020). Alginate hydrogel dressings for advanced wound management. *Int. J. Biol. Macromol.* 162, 1414–1428. doi: 10.1016/j.ijbiomac.2020.07.311.

Zhang, Z., Zhao, L.-S., and Liu, L.-N. (2021). Characterizing the supercomplex association of photosynthetic complexes in cyanobacteria. *R. Soc. Open Sci.* 8, 202142.

Zhao, M., and Running, S. W. (2010). Drought-Induced Reduction in Global. *Science.* 329, 940–943. doi: 10.1126/science.1192666.